Specially Shaped Optical Fiber Probes: Understanding and Their Applications in Integrated Photonics, Sensing, and Microfluidics

A Dissertation

Submitted to the Faculty

of the

WORCESTER POLYTECHNIC INSTITUTE

in partial fulfillment of the requirements for the

Degree of Doctor of Philosophy

in

Mechanical Engineering

by

Yundong Ren

June 2019

Advisory Committee:

Assistant Professor Yuxiang Liu, Advisor (Mechanical Engineering Department, WPI),

Professor Jamal Yagoobi (Head of Mechanical Engineering Department, WPI),

Professor Douglas T. Petkie (Head of Physics Department, WPI),

Associate Professor Songbai Ji (Biomedical Engineering Department, Mechanical Engineering Department, WPI)

Professor Pawan Singh Takhar (Food Engineering, UIUC),

Associate Professor Pratap Rao (Graduate Committee Representative, Mechanical Engineering Department, WPI)

Abstract

Thanks to their capability of transmitting light with low loss, optical fibers have found a wide range of applications in illumination, imaging, and telecommunication. However, since the light guided in a regular optical fiber is well confined in the core and effectively isolated from the environment, the fiber does not allow the interactions between the light and matters around it, which are critical for many sensing and actuation applications. Specially shaped optical fibers endow the guided light in optical fibers with the capability of interacting with the environment by modifying part of the fiber into a special shape, while still preserving the regular fiber's benefit of low-loss light delivering. However, the existing specially shaped fibers have the following limitations: 1) limited light coupling efficiency between the regular optical fiber and the specially shaped optical fiber, 2) lack special shape designs that can facilitate the light-matter interactions, 3) inadequate material selections for different applications, 4) the existing fabrication setups for the specially shaped fibers have poor accessibility, repeatability, and controllability.

The overall goal of this dissertation is to further the fundamental understanding of specially shaped fibers and to develop novel specially shaped fibers for different applications. In addition, the final part of this dissertation work proposed a microfluidic platform that can potentially improve the light-matter interactions of the specially shaped fibers in fluidic environments. The contributions of this dissertation work are summarized as follows: **1) An enhanced fiber tapering system for highly repeatable adiabatic tapered fiber fabrications.** An enhanced fiber tapering system based on a novel heat source and an innovative monitoring method has been developed. The novel heat source is a low-cost ceramic housed electric furnace (CHEF). The innovative monitoring method is based on the frequency-domain optical transmission signal from the fiber that is being tapered. The enhanced fiber tapering system can allow highly repeatable fabrication of adiabatic tapered fibers. **2) A lossy mode resonance (LMR) sensor enabled by SnO_2 coating on a novel specially shaped fiber design has been developed.** The developed LMR sensor has a D-shape fiber tip with SnO_2 coating. It has the capability of relative humidity and moisture sensing. The fiber-tip form factor can allow the sensor to be used like a probe and be inserted into/removed from a tight space. **3) Specially shaped tapered fibers with novel designs have been developed for integrated photonic and microfluidic applications.** Two novel specially tapered fibers, the tapered fiber loop and the tapered fiber helix have been developed. The tapered fiber loop

developed in this work has two superiority that differentiated itself from previous works: a) the mechanical stability of the tapered fiber loop in this work is significantly better. b) the tapered fiber loops in this work can achieve a diameter as small as 15 μm while still have a high intrinsic optical quality factor of 32,500. The tapered fiber helix developed in this work has a 3D structure that allows it to efficiently deliver light to locations out of the plane defined by its two regular fiber arms. Applications of the tapered fiber helices in both integrated photonic device characterizations and microparticle manipulations have been demonstrated. 4**) Developed an acrylic-tape hybrid microfluidic platform that can allow function reconfiguration and optical fiber integration.** A low-cost, versatile microfluidic platform based on reconfigurable acrylic-tape hybrid microfluidic devices has been developed. To the best of the author's knowledge, this is the first time that the fabrication method of sealing the acrylic channel with a reconfigurable functional tape has been demonstrated. The tape-sealing method is compatible with specially shaped fiber integrations.

Acknowledgements

I would like to take this short page to express my sincere gratefulness to a large group of people who have all made great contribution to my Ph.D. study.

First and foremost, I would like to express my deepest appreciation to my advisor Professor Yuxiang Liu, for his mentorship, support, and inspiration. Throughout my Ph.D., he has passionately taught me a great amount of exciting science and valuable skills. However, his influence on me goes far beyond professional development. Through his own words and deeds, I have learned a lot of valuable lessons about how to deal with choices and challenges in life. I cherish this past experience as his student, and I believe this experience will continue to lead me in my future adventures in life.

I would like to thank my dissertation committee members, Professor Jamal Yagoobi, Professor Pratap Rao, Professor Yuxiang Liu, Professor Douglas Petkie, and Professor Pawan Singh Takhar for taking your valuable time to review my dissertation. Particularly, I want to thank Professor Rao for his generous help and valuable suggestions to my research. In the development of the lossy-mode-resonance sensor, his insights on material selection have played an important role in the success of the project. He has generously lent me many chemicals and chemistry related equipment for my research work. His student Tao Yan and Binod Giri have helped me with the SEM imaging.

I would also like to thank Mr. Peter Hefti for his invaluable help in the machine shop. Without his help, many of my designs will be just a 2D schematic drawing. His optimistic loud laughter can always put smile on people's face.

I am deeply grateful to the all my lab mates and friends for their supports, they are (in no particular order), Chaoyang Ti, Yao Shen, Rui Zhang, Subhrodeep Ray, Mucheng Li, Mengqiao Yang, Haimi Tang, and Lite Zhou, without your company, my Ph.D. life will be much more arduous and less fun.

Outside WPI, I would also like to thank Professor Misha Sumetsky and Dr. Yong Yang from Aston University in the UK. Thank you for hosting my stay in the UK for the summer research. Your passion in research has invigorated me to pursue a career in science.

Finally, with all my heart, I want to thank my wife, Zeyan Huang, and my parents, Mr. Xuegong Ren and Mrs. Mitao Liao. Your unconditional support and encouragement are the sources of my strength. I'm deeply indebted to your sacrifice for me, this dissertation is dedicated to you.

Table of Contents

CHAPTER 1 INTRODUCTION AND BACKGROUND 1

1.1 PROBLEM OF INTEREST 1

1.2 REGULAR OPTICAL FIBERS 2

1.2.1 Basic information of regular glass optical fibers 2

1.2.2 Optical modes of regular step-index optical fibers 4

1.3 STATE OF THE ART OF SPECIALLY SHAPED FIBERS 6

1.3.1 Straight tapered optical fibers 6

1.3.1.1 Basic information of the straight tapered optical fibers 6

1.3.1.2 Existing fiber tapering methods 8

1.3.1.3 Applications of the straight tapered fibers 16

1.3.2 Dimpled tapered fibers 22

1.3.2.1 Fabrication of dimpled tapered fiber 22

1.3.2.2 Application of the dimpled tapered fiber 23

1.3.2.3 Limitations of the dimpled tapered fiber 24

1.3.3 Tapered fiber ring resonators 25

1.3.3.1 Fabrication of the tapered fiber ring resonators 25

1.3.3.2 Sensing applications of the tapered fiber ring resonators 30

1.3.4 D-shape optical fibers 31

1.3.4.1 Fabrication of D-shape fibers 31

1.3.4.2 Applications of the D-shape fibers 32

1.4 MOTIVATION OF THIS DOCTORAL RESEARCH 36

1.5 OBJECTIVES AND SCOPE OF THE DISSERTATION 38

CHAPTER 2 TAPERED OPTICAL FIBER LOOPS AND HELICES FOR INTEGRATED PHOTONIC DEVICE CHARACTERIZATIONS AND MICROPARTICLE MANIPULATIONS 41

2.1 A BRIEF REVIEW OF THE EXISTING SPECIAL-SHAPE TAPERED FIBERS 41

2.1.1 Existing special-shape tapered fibers and their applications 41

2.1.2 Fabrication methods of the existing special-shape tapered fibers 42

2.2 DEVELOPMENT OF FABRICATION SETUPS FOR THE TAPERED FIBER LOOPS AND HELICES 43

2.2.1 Fiber tapering system based on an alcohol lamp 43

2.2.2 Fabrication methods for the tapered fiber loops and helices 45

2.3 OPTICAL CHARACTERIZATIONS OF THE TAPERED FIBER LOOPS AND HELICES 47

2.3.1 Optical spectroscopies of the tapered fiber loops and helices 47

2.3.2 Mechanical stability of the annealed tapered fiber loops..... 49

2.4 EXPERIMENTAL DEMONSTRATION OF INTEGRATED PHOTONIC DEVICE CHARACTERIZATION USING THE TAPERED FIBER HELICES 50

2.4.1 Brief description of the integrated photonic device used in the experiment..... 50

2.4.2 Comparison of straight tapered fibers and tapered fiber helices for in-plane integrated photonic device characterization..... 51

2.4.3 Experimental characterization results 52

2.5 EXPERIMENTAL DEMONSTRATION OF MICROPARTICLE MANIPULATIONS USING THE TAPERED FIBER HELICES..... 53

2.6 SUMMARY..... 55

CHAPTER 3 HIGHLY ACCESSIBLE AND LOW-LOSS FIBER TAPERING SETUP BASED ON A CERAMIC HOUSED ELECTRIC FURNACE (CHEF)..... 56

3.1 REVIEW OF CURRENT HEAT SOURCES USED IN THE HEAT-AND-PULL FIBER TAPERING SETUP 57

3.2 DEVELOPMENT OF THE CHEF-BASED FIBER TAPERING SETUP 59
3.2.1 Fiber tapering setup based on the CHEF heat source 59
3.2.2 Fabrication of the CHEF 60
3.2.3 Recommendations for the CHEF fabrication process 61
3.3 EXPERIMENTAL STUDY AND CHARACTERIZATION OF THE CHEF 62
3.3.1 Parametric study and general design guidelines of the CHEF 62
3.3.2 Temperature characterization of the CHEF 66
3.4 FUNDAMENTAL UNDERSTANDING OF THE FIBER TAPERING PROCESS 68
3.4.1 Shape of the straight tapered fiber 68
3.4.2 Optical modes evolution in a tapered fiber 70
3.5 EXPERIMENTAL AND THEORETICAL STUDY OF THE OPTICAL TRANSMISSION OF THE TAPERING PROCESS 72
3.5.1 Experimentally measured time-domain and frequency-domain optical transmission signals 72
3.5.2 Theoretical analysis of the optical transmission signal 74
3.6 DEVELOPMENT OF A RELIABLE FIBER TAPERING MONITORING METHOD 76
3.7 EXPERIMENTAL DEMONSTRATION OF A CLOSE TO PERFECT-ADIABATIC STRAIGHT TAPERED FIBER 78
3.8 SUMMARY 80
CHAPTER 4 D-SHAPE FIBER-TIP RELATIVE HUMIDITY SENSOR BASED ON LOSSY MODE RESONANCE 82
4.1 REVIEW OF THE RECENT DEVELOPMENT OF LMR OPTICAL FIBER SENSORS 83
4.2 SENSOR DESIGN AND FABRICATION 83
4.3 WORKING PRINCIPLE OF THE D-SHAPE LMR RELATIVE HUMIDITY AND MOISTURE SENSOR 86

4.3.1 Numerical simulation of the LMR phenomenon 87
4.3.2 Fundamental understanding of the influence of the relative humidity on the LMR signal 90
4.4 CHARACTERIZATIONS OF THE LMR SENSOR FOR RELATIVE HUMIDITY (RH) SENSING ... 91
4.4.1 Optical system for the sensor characterization 91
4.4.2 Experimental characterization of the LMR signal 92
4.4.3 Development of the characterization system 93
4.4.3.1 Customized RH chamber 93
4.4.4 Experimental characterization of the LMR sensor's dynamic response to relative humidity 94
4.5 EXPERIMENTAL CHARACTERIZATION OF THE SENSOR'S CAPABILITY OF MEASURING MOISTURE CONTENT IN FOOD SAMPLES 97
4.6 SUMMARY 99
CHAPTER 5 RECONFIGURABLE ACRYLIC-TAPE-HYBRID MICROFLUIDICS 100
5.1 REVIEW OF EXISTING MICROFLUIDIC PLATFORMS 100
5.2 FABRICATION METHODS AND MATERIALS 102
5.3 EXPERIMENTAL CHARACTERIZATION OF THE FLOW IN THE VECTOR ABLATED ACRYLIC CHANNELS 104
5.4 RECONFIGURABLE ACRYLIC-TAPE HYBRID MICROFLUIDIC DEVICES WITH MULTIPLEX FUNCTIONS 107
5.5 ACRYLIC-TAPE MICROFLUIDIC DEVICES WITH ON-CHIP PUMPS 112
5.5.1 On-chip paper pump 112
5.5.2 On-chip pipette tube pump 113
5.6 SYRINGE PUMP DRIVEN MONODISPERSE DROPLET GENERATION 114

5.7 PRELIMINARY EXPERIMENTAL RESULTS OF INTEGRATION WITH LMR D-SHAPE OPTICAL FIBER SENSORS (AND FUTURE PLANS) 116
5.8 SUMMARY 118
CHAPTER 6 SUMMARY AND FUTURE WORK 120
6.1 SUMMARY AND CONTRIBUTIONS OF THE DISSERTATION WORK 120
6.2 FUTURE WORK 123
6.3 SOCIAL IMPACT OF THIS DISSERTATION WORK 125
6.3.1 Tapered fibers. 125
6.3.2 D-shape fibers 126
6.3.3 Acrylic-tape hybrid microfluidic platform. 127
REFERENCES: 128

Chapter 1 INTRODUCTION AND BACKGROUND

1.1 PROBLEM OF INTEREST

Since the pioneering work of light-guiding glass fibers by Sir Charles K. Kao in 1960s, optical fibers have flourished in the telecommunication industry, its anticipated market size is going to reach USD ~ 4 billion by 2025 [1]. Optical fibers are preferred in the telecommunication industries because it can deliver optical signals with low loss and minimum noise is introduced during the transmission. This is because in a regular telecom fiber, the guided light is well confined in the core and effectively isolated from the environment. In addition to telecommunication, other applications have also enjoyed various advantages of the optical fibers. For example, in fiber optic illumination and endoscope applications, the flexible optical fiber can transmit light with low loss and deliver light to locations otherwise difficult for light to reach (e.g. within the human body).

However, in many applications such as sensing and actuation [2–4], efficient light delivery is not enough to fulfill the task, and it is imperative to enable the interactions between the guided light and the matters around the fiber. Despite its importance, a regular optical fiber does not allow the light to interact with the environment. Although light-matter interactions have been commonly enabled by light propagating in free space, such interactions are subject to the limitations of free-space optics, such as spatial resolution confined by the diffraction limit, light scattering and absorption of the media, and susceptibility to the environmental fluctuations. By comparison, optical fibers enable convenient and reliable light delivery with high spatial resolution (not confined by diffraction limits), regardless of light scattering or absorption by the environment, resulting in well-controlled light-matter interactions.

A general solution to the fiber-delivered light-matter interactions is the specially shaped optical fiber. Such fibers can have modified exotic geometry, engineered material properties, and carefully designed light manipulation capabilities that address the particular needs of various applications. The ideal specially shaped fiber should be easily accessible, can be fabricated in a repeatable and controllable manner, allows strong light-matter interactions at the desired location at the fibers, and facilitates low-loss, robust light delivery and readout. Both fiber-end and in-line types are interesting/important. The fiber-end specially shaped fibers can allow easy and quick

insertion/removal of the fiber at point of interest. The in-line specially shaped fibers can allow a continuous low-loss light propagation along the fiber and is ideal for micro/nano-device optical characterizations.

The state of art of both types will be reviewed in Sections 1.2 and 1.3, and their challenges will be detailed in Section 1.4. This dissertation work aims to develop highly accessible novel specially shaped optical fibers of both in-line and fiber-end types with enhanced capabilities for different applications.

1.2 REGULAR OPTICAL FIBERS

1.2.1 Basic information of regular glass optical fibers

Most of current commercially available fibers are made of glass. These fibers can be categorized into three groups by their internal structures.

Step-index fibers: The most widely used step-index fibers have two layers, the core and the cladding, and each layer has a constant and uniform refractive index. The refractive index of the core of the step-index fiber is larger than that of the cladding, which allows it to guide light through total internal reflections.

Graded-index fibers: A graded-index fiber also has the core-cladding two-layer structure similar to the step-index fiber. But while its cladding has a uniform and constant refractive index, the refractive index profile of its core is a function of the radial distance from the cylindrical fiber's longitudinal axis. Because this gradually changing core refractive index, light in a graded-index fiber is being continuously focused and guided.

Microstructured fibers: In a microstructured fiber, the structure within the cylindrical glass rod is modified by air holes. Light in a microstructured fiber can be guided not only by the refractive index differences of the fiber but also through the constructive interference of scattered light. For example, one type of microstructured fiber called the photonic crystal fiber guides light based on the photonic bandgap effect.

Optical fibers can also be classified into two categories based on the number of supported optical modes, namely the single-mode fibers and multi-mode fibers. The optical modes which are the electromagnetic field distributions of the propagating light at the fiber's cross section are found

by solving the Maxwell's equation under the boundary condition imposed by the optical fibers (more details will be discussed in later sections). The single-mode optical fibers support only one optical mode (the fundamental mode), while the multi-mode optical fibers can support more than one optical mode, in fact, it is common that a multi-mode fiber can support more than hundreds of modes. In the telecommunication industry, because of its mature fabrication technics, low propagation loss and low modal dispersion, the step-index single-mode fibers working at the wavelength of 1310 nm and 1550 nm are widely used. Because of their mass adoption in the telecommunication industry, the cost for this type of optical fibers is very low (see Table 1 below for comparison), resulting in unparalleled accessibility. In addition, most of the fabrication and characterization methods for the custom step-index, single-mode fibers are valid for multimode fibers. ***Considering these advantages of the step-index fiber, I have chosen the single-mode step-index fiber (SMF-28, Corning) from Corning for all the works done in this dissertation.*** The SMF-28 fiber's core has a diameter of 8.2 μm and a refractive index of 1.452, its fiber cladding has a diameter of 125.0 ± 0.7 μm and a refractive index of 1.447.

Fiber Type	Cost per meter ($)	Optical Loss (dB/km)	Working Wavelength (nm)
Step-index Single-mode fiber	0.08	≤ 0.32	1310
Step-index Multi-mode fiber	4.82	≤ 8	250-1200
Graded-index Multi-mode fiber	1.29	≤2.3 @ 850 nm ≤0.6 @ 1300 nm	800-1600
Photonic crystal fiber	160.74	≤ 3	1550

1.2.2 Optical modes of regular step-index optical fibers

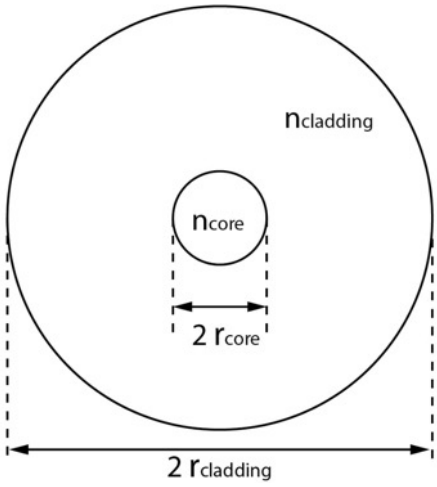

Figure 1 Schematic of the cross section of a regular optical fiber.

Consider a step-index optical fiber with core radius of r_{core}, core refractive index n_{core}, and cladding refractive index $n_{cladding}$, as shown in Figure 1. The optical modes supported by this fiber can be found by solving the source-free Maxwell's equations (Equation 1-4) under the boundary condition (Equation 5-6) that at the core-cladding boundary the tangential components of the electric field $\vec{E}_t$ and the magnetic field $\vec{H}_t$ should be equal [15].

$$\nabla \cdot \vec{D} = 0 \tag{1}$$

$$\nabla \cdot \vec{B} = 0 \tag{2}$$

$$\nabla \times \vec{E} = -\frac{\partial \mathrm{B}}{\partial t} \tag{3}$$

$$\nabla \times \vec{H} = \frac{\partial \vec{\mathrm{D}}}{\partial t} \tag{4}$$

$$\vec{E}_t^{core} = \vec{E}_t^{cladding} \tag{5}$$

$$\vec{H}_t^{core} = \vec{H}_t^{cladding} \tag{6}$$

In the above equations, $\vec{E}$ is the electric field, $\vec{B}$ is the magnetic flux, $\vec{D} = \epsilon\vec{E}$ is the electric displacement field, where ϵ is the permittivity of the medium, and $\vec{H} = \frac{\vec{B}}{\mu}$ is the magnetic field, where μ is the permeability of the medium.

For most of the step-index fibers, the refractive index difference between the core and the cladding are very small, and hence a simplifying approximation of $n_{core} \cong n_{cladding}$ can be applied [15] to the solutions of the above equations. This approximation is called the weakly guiding approximation. The simplified solutions of the optical modes are called the linearly polarized modes (LP modes). The optical intensity distributions of different LP modes at the cross section of the fiber core are shown in Figure 2 (a). The relation between the linearly polarized modes in a step-index fiber and the fiber core radius and light wavelength are characterized in a plot called the dispersion-curves plot as shown in Figure 2 (b). In the plot, the normalized frequency (or V-number) $V = \frac{2\pi}{\lambda} r_{core}\sqrt{n_{core}^2 - n_{cladding}^2}$, the normalized propagation constant $b = \frac{n_{eff}^2 - n_{cladding}^2}{n_{core}^2 - n_{cladding}^2}$, where n_{eff} is the effective refractive index of the optical mode. To find out the LP modes supported by the step-index fiber at different V-number, one can draw a line perpendicular to the V-number axis and look for the crossing between the line and the dispersion curves. From the dispersion-curves plot, it is obvious that as the V-number decreases, the number of supported LP modes will also decrease. In fact, when the V-number value is below 2.405, a step-index fiber will support only the LP_{01} optical mode [15]. As a result, the V-number value of 2.405 is a critical value that can be used to determine whether a step-index fiber is single-mode or multi-mode.

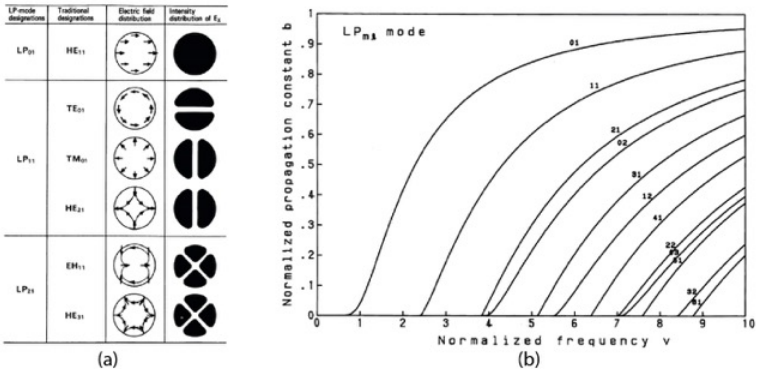

Figure 2 (a) Optical intensity distribution of different LP modes at the cross section of the fiber core. (b) The dispersion curves of different LP modes.

1.3 STATE OF THE ART OF SPECIALLY SHAPED FIBERS

Various special-shape fibers for a wide range of applications have been developed [XX], to cover all of them here is not realistic. In this dissertation, I will review 6 specially shaped fibers that is most representative and also most relevant to the work of this dissertation (special-shapes that facilitate the light-environment interactions), including **straight tapered fibers** [9,16–19], **dimpled tapered fibers** [9,10], **tapered fiber coils** [7,8,14,20,21]**, tapered fiber knots** [7,11,22–26]**, tapered fiber loops** [27–31]**, and D-shape fibers** [32,33]**.**

1.3.1 Straight tapered optical fibers

We will start our review of state-of-the-art of special-shape fibers with straight tapered fibers. Straight tapered fibers are first reviewed not only because it has a wide range of applications but also because it is the basis for several other special-shape fibers including the dimpled tapered fibers, the tapered fiber coils, the tapered fiber knots and the tapered fiber loops.

1.3.1.1 Basic information of the straight tapered optical fibers

Geometric parameters of a tapered fiber

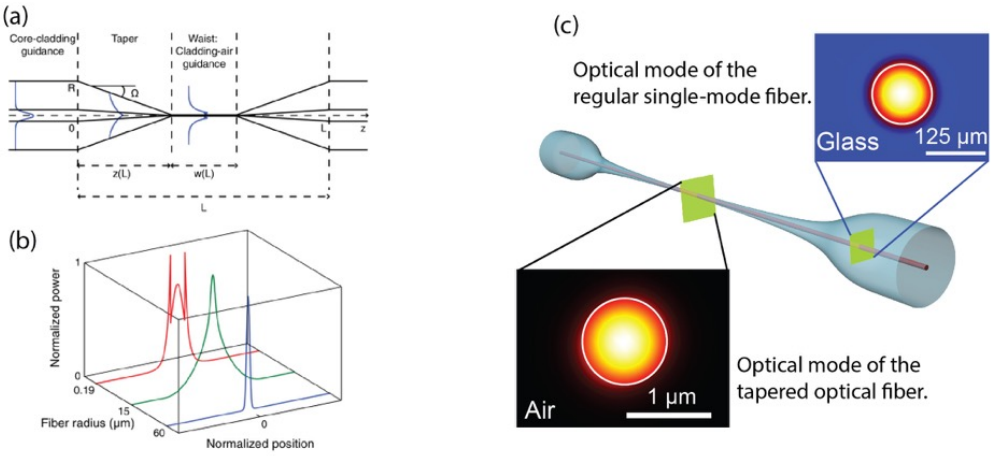

Figure 3 Schematic of the different sections of the tapered fibers [18] (b) Calculated electric intensity profile of tapered fibers with different diameters. [18] (c) 3-D schematic of the straight tapered fiber. The insets show the simulation results of the optical modes at different parts of the tapered fiber.

Straight tapered fibers are fabricated from regular single-mode step-index optical fibers by tapering down a part of a regular fiber. A straight tapered fiber can be separated into three different

sections as shown in Figure 3 (a), including the regular fiber section, the taper section or the transition section, and the waist section. The regular fiber section is not affected by the tapering and has the same geometry as an un-tapered regular fiber. In the transition section, the diameter of the tapered fiber gradually decreased from that of a regular fiber to that of the waist section. The total length of the two transition sections are called the tapering length. In the waist section, the diameter of the tapered fiber reaches the smallest value and has a uniform profile.

Optical modes and the evanescent field of a tapered fiber

When the light is launched into a tapered fiber, it will be coupled from the regular fiber section through the transition section into the waist section of the tapered fiber. At the waist section, as shown in Figure 3 (b-c), the light will no longer be guided by the core-cladding boundary, instead, it will be guided by the cladding-environment boundary, in the case of Figure 3 (b-c) the environment is the air. This means that in the waist section, the previous cladding of a regular fiber will become the effective core and the surrounding air will become the effective cladding. At the waist section, as shown by the inset in Figure 3 (c), part of the electromagnetic field of the propagating light is extended into the environment. This extended electromagnetic field is due to the boundary conditions imposed by the electromagnetic theory [15] which says that the tangential electric field ($\vec{E}_t$) and magnetic field ($\vec{H}_t$), and the normal electric displacement field $\vec{D}_n$ and magnetic flux $\vec{B}_n$ should be equal at the boundary of two source-free dielectric medium. When light is propagating in an optical fiber, because the electromagnetic field within the fiber core is continuous and is not zero at the core-cladding boundary, part of the electromagnetic field will have to extend outside the core and into the cladding, so that the boundary conditions are satisfied. This extended electromagnetic field is also known as the evanescent field of a waveguide. For input light with the wavelength of ~1.3 μm, the range of the evanescent field is only a few micrometers, so that in the regular fiber section, the evanescent field is embedded within the 125 μm fiber cladding. However, in the waist section of a tapered fiber, because the effective cladding has become the environment (e.g. air, water), the evanescent field will be able to extend into the environment and the light carried by the evanescent field is ready to be exploited for light-environment interactions.

High-quality straight tapered fibers

The quality of a straight tapered fiber is determined by both its optical insertion loss and its tapering length (total length of the two transition sections). A high-quality tapered fiber with low-insertion loss is called an adiabatic tapered fiber. The word "adiabatic" is borrowed from thermodynamics, which means a process that does not involve the transfer of heat or matter into or out of a system. In here, adiabatic means that the process of light coupling from the regular fiber section to the waist section has low optical loss [18]. Correspondingly, the tapering process that fabricates adiabatic tapered fibers is called an adiabatic fiber tapering process. The requirement for the tapering length for a high-quality tapered fiber is different for different applications. A long tapering length is preferred when a long interaction length between the light and the environment [34] or the tapered fiber itself [35] is required, while a short tapering length is preferred when the application require the tapered fiber have high mechanical stability and can be maneuvered easily [9]. With the abovementioned two requirements for the high-quality tapered fiber, an ideal fiber tapering setup should have the capability of fabricating high-transmission tapered fibers with different lengths.

1.3.1.2 Existing fiber tapering methods

We have mentioned in the section above that a tapered fiber is fabricated by tapering down a part of a regular fiber, in practice, mainly two fiber tapering methods have been used, namely, the heat-and-pull method [9,18,36,37] and the HF-etching method [38,39]. Detailed reviews for both methods are presented in the following sections.

1.3.1.2.1 The heat-and-pull fiber tapering method

In the heat-and-pull method, both ends of a straightened regular fiber will first be clamped onto two motorized stages, the center part of the fiber is then heated up by a heat source to a temperature above the transition temperature of the glass and becomes soft. The softened fiber will be pulled by the two motorized stages and being thinned down. To illustrate the fiber tapering setup based on the heat-and-pull method, a general schematic of the setup is shown in Figure 4 without specifying the type of heat source used.

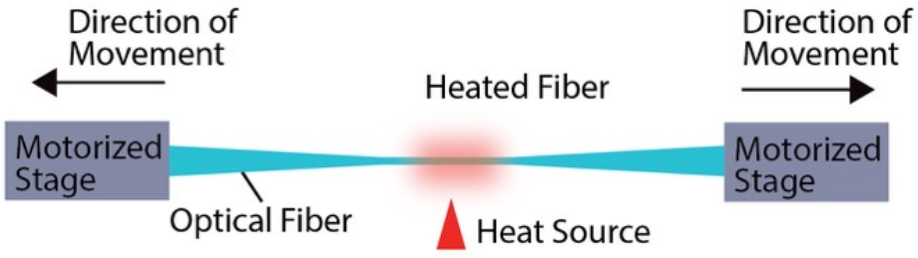

Figure 4 A general schematic of the heat-and-pull based fiber tapering setup.

Effective heating length and its relationship with the tapered fiber geometry

For most of the heat sources put in a room environment, there is a temperature gradient within the heat source. The effective heating length of a heat source used for the fiber tapering is defined as the length of the heat source within which the temperature is higher than the glass' transition temperature (meaning it is high enough to soften the glass for the tapering). The geometry of a tapered fiber fabricated by the heat-and-pull method can be described by Equation (7-8) with parameters defined in Figure [5].

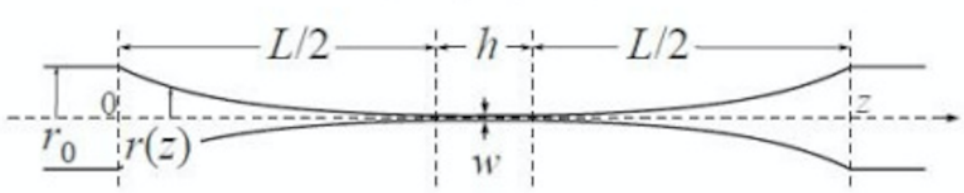

Figure 5 Schematic of a tapered fiber fabricated by the heat-and-pull fiber tapering method [40]. The parameters defined in the schematic is used in Equation (7-8). r_0: radius of a regular fiber; $r(z)$: radius of the fiber at the transition section; w: radius of the tapered fiber waist; L: the tapering length; h: effective heating length.

$$r(z, L) = r_0 \exp\left(\frac{-z}{h}\right) \quad \text{for } 0 < z < \frac{L}{2} \tag{7}$$

$$r(z, L) = w \equiv r_0 \exp\left(\frac{-L}{2h}\right) \quad \text{for } \frac{L}{2} < z < \frac{L+h}{2} \tag{8}$$

Flame-based fiber tapering setups

Flame can easily achieve the temperature required for the fiber tapering (transition temperature of glass) and is widely used as the heat-source for the fiber tapering [9,19,37,40,41]. Mainly two types of flames have been used for the fiber tapering [41], including oxygen-butane torch generated flame [36] and oxygen-hydrogen torch generated flame [9], as shown in Figure 6 (b).

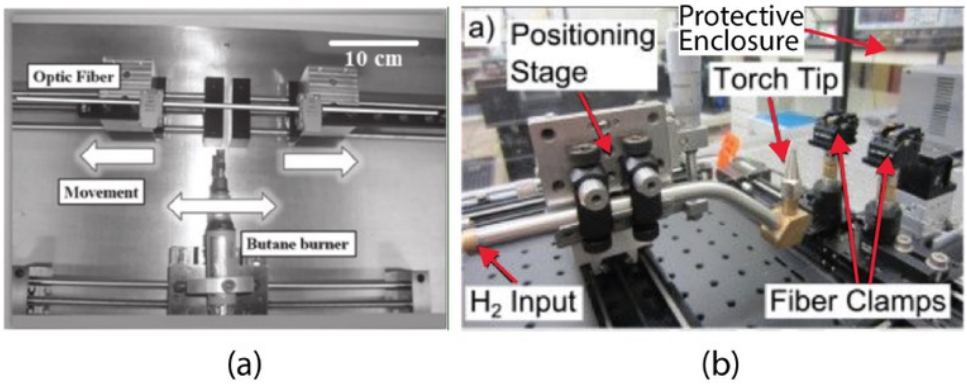

Figure 6 (a) An oxygen-butane-torch based fiber tapering setup [36]. (b) An oxygen-hydrogen-torch based fiber tapering setup [9].

While flames can be easily accessed, it need to be carefully controlled to generate high-quality adiabatic tapered fibers. Firstly, to prevent the environment's disturbance on the flame, such as environmental air flows, the tapering setup need to be enclosed in a segregated environment. As we can see in Figure 6 (b), the oxygen-hydrogen-flame-based tapering setup is enclosed by an acrylic protective enclosure. Secondly, even in an environment that the air flow is static, the flame can still be fluctuating due to the unstable gas flow [27]. Furthermore, in the case of oxygen-butane torch, to ensure a complete combustion, the ratio between the oxygen and butane flow need to be well controlled. An incomplete combustion of oxygen-butane gas will generate soot and contaminate the tapered fiber. To stabilize and well control the gas flow, a relatively complex gas flow control setup is required, such as the one shown in Figure 7 (a).

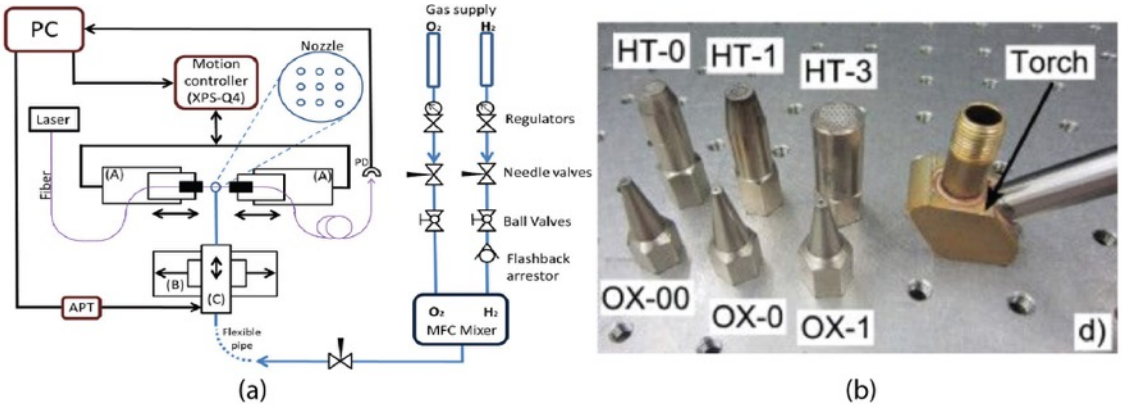

Figure 7 (a) Schematic of a gas flow control system for an oxygen-hydrogen flame for the fiber tapering. [41] (b) Flame torches with different nozzle diameters. The sizes of the nozzles goes from the largest to the smallest by HT-3, HT-1, HT-0, OX-1, OX-0, and OX-00. [9]

For a flame-based, heat-and-pull fiber tapering setup, there are two ways to change the tapering length of a tapered fiber. One is to change the size of the flame by using torches with different nozzle sizes as shown in Figure 7 (b) [9]. A larger flame size will give a larger effective heating length and hence longer tapering length and vice versa. Another way to change the tapering length is to create a relative movement between the torch and the fiber. As shown in Figure 6 (a-b), the torches were mounted on motorized stages, during the tapering the torches will move relatively to the fibers in a brushing-like motion. By controlling the movement of the torch, the tapering setup can mimic different effective heating lengths longer than the size of the flame from the torch nozzle.

Currently the flame-based fiber tapering setup is being widely used [41], but many of them cannot repeatedly fabricate high-transmission tapered fibers. *The limitations of the flame-based fiber tapering setup are summarized below:*

i. The stability of the temperature and position of the flame heat source is susceptible to the flow fluctuation of the environment. A non-stable flame will influence the adiabaticity of the transition-section of the tapered fiber and results in a low-transmission tapered fiber.
ii. The stability of the flame heat source is will also be influenced by the unstable gas flow.
iii. Incomplete combustion of the flame-based heat source will generate soot which will contaminate the tapered fiber and results in a low-transmission tapered fiber.

CO_2-laser-based setups

A CO_2-lasers-based fiber tapering setup shown in Figure 8 (a) and (b). In the fiber tapering setup based on direct CO_2-laser heating, as shown in Figure 8 (a), part of the optical fiber is being heated by a focused CO_2-laser spot which is scanning along the glass fiber. The heating mechanism is based on the glass fiber absorbing radiation energy from the CO_2-laser [37]. Since the energy absorption efficiency of the glass fiber has an inverse square relationship with the diameter of the glass fiber, the minimum diameter of the tapered fiber achievable using the CO_2-laser-based fiber tapering setup is limited (~3 μm) [37]. The effective heating length of the setup can be actively controlled by changing the scanning length and scanning speed of the laser spot [37].

In the fiber tapering setup based on the indirect CO_2-laser heating as shown in Figure 8 (b), the optical fiber is inserted into a sapphire tube which is being heated by a focused laser beam. The sapphire tube will absorb energy from the CO_2 laser and the temperature within the sapphire tube will be raised above the glass transition temperature, which will allow the optical fiber to be

softened for the fiber tapering. In this case, the effective heating length will be determined by the length of the sapphire tube.

The limitation of the CO_2-laser-based fiber tapering setup is summarized below:

i. For the fiber tapering setup based on direct CO_2-laser heating, the minimum achievable tapered fiber diameter is limited (~ 3 μm).

ii. For both setups, to achieve efficient heating, it is critical that the CO_2-laser light spot is focused onto the glass optical fiber or the sapphire tube. To satisfy this requirement, the CO_2-laser beam need to be re-aligned every time before usage.

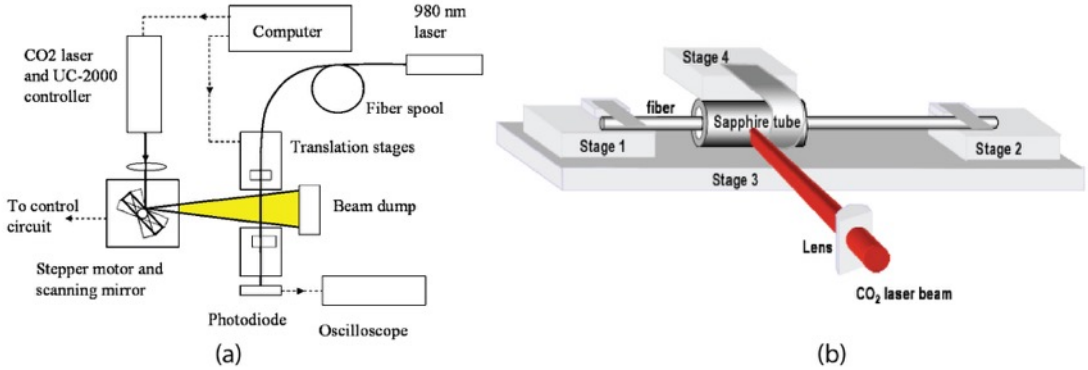

Figure 8 (a) A fiber tapering setup based on direct CO_2-laser heating. [37] (b) A fiber tapering setup based on indirect CO_2-laser heating [8]. In the schematic, the fiber within the sapphire tube is indirectly heated by the CO_2-laser.

Commercial ceramic micro-heater-based setup

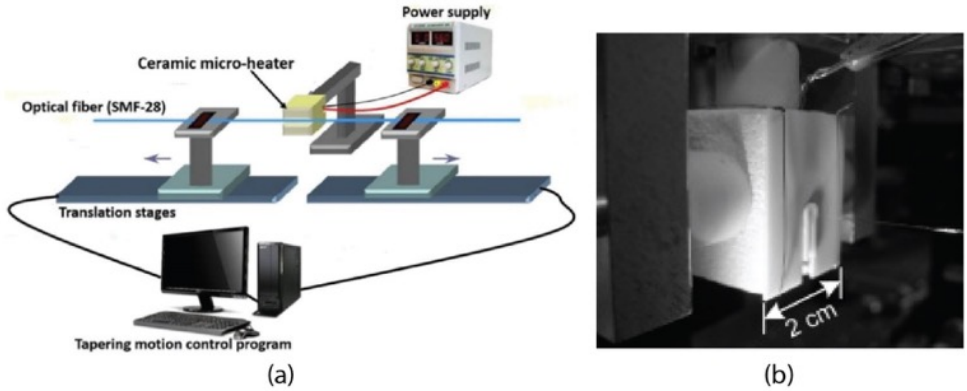

Figure 9 (a) Schematic of a commercial micro-heater-based fiber tapering setup [42]. (b) Photo of a commercial ceramic microheater [27].

A commercial ceramic micro-heater-based fiber tapering setup is shown in Figure 9 (a). The heating mechanism of the microheater is based on electrical resistive heating. A close-up photo of

the micro-heater is shown in Figure 9 (b), the electrical heating element is embedded in a ceramic housing which insulates the heating chamber from the environment. The glass fiber can move into and out of the main heating chamber through a slot-like opening on the ceramic housing. Compared to the flame and CO_2-laser, the micro-heater does not have the concern of unstable heating temperature, soot contamination, and require only little maintenance.

Although with the abovementioned advantages, in the published tapered fiber works, the commercial micro-heater-based fiber tapering setup was not used as much as the flame and the CO_2-laser based setup. The reasons that prevented the commercial micro-heaters' wide adaption for the fiber tapering is mainly because it is relatively difficult to access these micro-heaters. To the best of the author's knowledge, there are only two companies are currently selling micro-heaters that can be used for the fiber tapering. One is from Micropyretics Heaters International Inc. (MHI), and another one is from NTT Advanced Technology (NTT-AT). The microheater from MHI has a high price tag of $20600, which is much higher than most of the flame or CO_2-laser based fiber tapering setups. The microheaters from NTT-AT have a comparatively lower price of $2500. However, according to a researcher in other lab that is using the NTT-AT micro-heater, the life span of the microheater is only around 1 year. Furthermore, considering the lead time for the NTT-AT microheater is 4 to 6 months, using the NTT-AT microheater can cause serious time delay in the experiment. A comparison of the two commercially available micro-heaters is organized in Table 1.

	Price	Life span	Lead Time
MHI	$20600	N/A	8 to 12 weeks
NTT-AT	$2500	~ 1 year (form unofficial sources)	4 to 6 months

Table .1 Comparison of two commercially available ceramic microheaters.

1.3.1.2.2 The HF-etching-based fiber tapering method

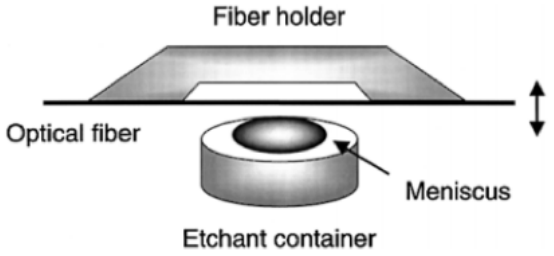

Figure 10 A schematic of the HF-etching based fiber tapering setup. [43]

A fiber tapering setup based on hydrofluoric acid (HF) etching is shown in Figure 10 [43]. In this method, a section of the glass fiber is tapered down through chemical etching. Compare to the heat-and-pull method, although the HF-etching-based fiber tapering method is more straightforward, it is much less used [44]. This is mainly due to the high insertion loss of the tapered fiber fabricated by the HF-etching method. The high insertion loss is mainly caused by the light scattering at the rough etched surface. According to one published work [43], an HF-etching fabricated tapered fiber with diameter of ~2 μm will only have 10% light transmission. In comparison, most of the heat-and-pull methods can routinely fabricate tapered fibers with transmissions higher than 80% [9,41]. In one recent work [44], to alleviate the insertion-loss problem in the HF-etching based fiber tapering, a surface-tension driven HF flow was used to both smoothen the fiber surface and to create a more gradual diameter change in the transition region. However, the etch time required by the surface driven flow is exceedingly long (~75 minutes), when compared with the heat-and-pull fabrication method that can fabricate a tapered fiber in around 7 minutes.

1.3.1.2.3 Existing monitoring method for the fiber tapering and their limitations

During a tapering process, the tapered fiber waist will experience a change of from the single-mode state to the multi-mode state and back to the single-mode. In most applications [9,18], it is desired that the tapered fiber waist is at the single-mode state. To satisfy this requirement, the diameter of the tapered fiber waist need to be decreased below a critical value (details about the critical value will be discussed in later sections). However, while a waist diameter below the critical value can always be achieved through fiber tapering, a too small waist diameter will either

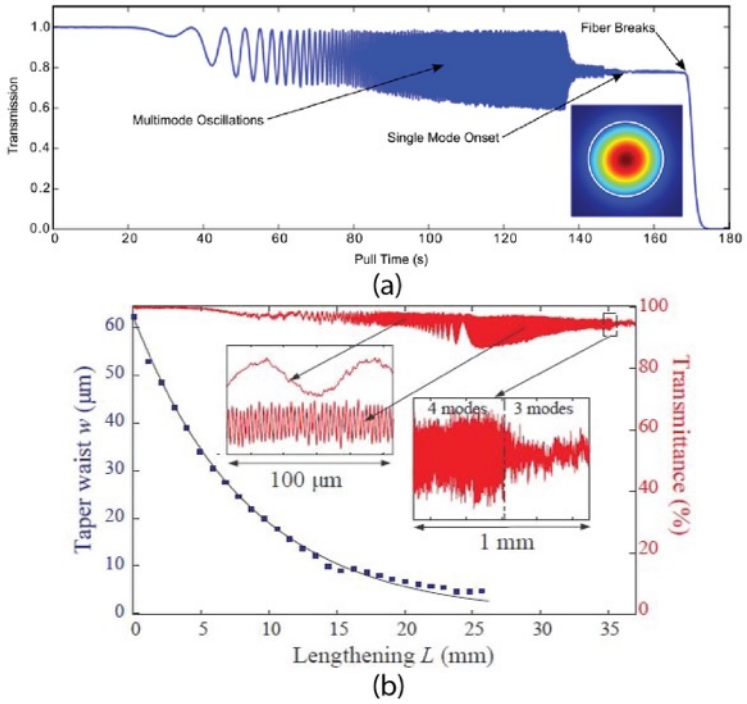

Figure 11 (a) and (b) Recorded real-time optical transmission signals during the fiber tapering processes. In (a) [9], the decrease of the fluctuation amplitude when the tapered fiber reached the single-state can be differentiated by bare eyes. In (b) [40], the decrease of the fluctuation amplitude when the tapered fiber reached the single-state cannot be differentiated by bare eyes.

cause the tapered fiber to break or become mechanically weak. The most ideal time to stop the tapering process is right after the tapered fiber waist has reached the critical value and has back to the single-mode state. However, considering that during the tapering the tapered fiber waist is either being placed in a high-temperature heat source or in a highly erosive acid, it is difficult to directly monitor the diameter change of the tapered fiber waist in real-time. An indirect monitoring method based on the real-time optical transmission of the tapered fiber has been developed and is widely used. In this method, the tapered fiber waist's transition from the multi-mode state to the single-mode state is determined by looking at the change of the fluctuation amplitude of the real-time optical transmission signal. As shown in Figure 11 (a), when the tapered fiber waist has changed from multi-mode state back to the single-mode state, the real-time transmission signal has also become stabilized. However, in some cases, when the tapered fiber waist changed from the multi-mode state to the single-mode state, the fluctuation amplitude change of the real-time transmission is not obvious. This will lead to a misjudgment of the stoppage of the tapering and results in a too big or too small tapered fiber diameter. For example, in the transmission shown in

Figure 11 (b), before the tapered fiber waist reached the single-mode state (still have 3 co-propagating modes), the transmission signal has already stabilized and has a similar fluctuation amplitude to that of the single-mode state tapered fiber. A monitoring method that can more reliably determine the stoppage of the tapering process is yet to be demonstrated.

1.3.1.3 Applications of the straight tapered fibers

1.3.1.3.1 Straight-tapered-fiber-based sensors

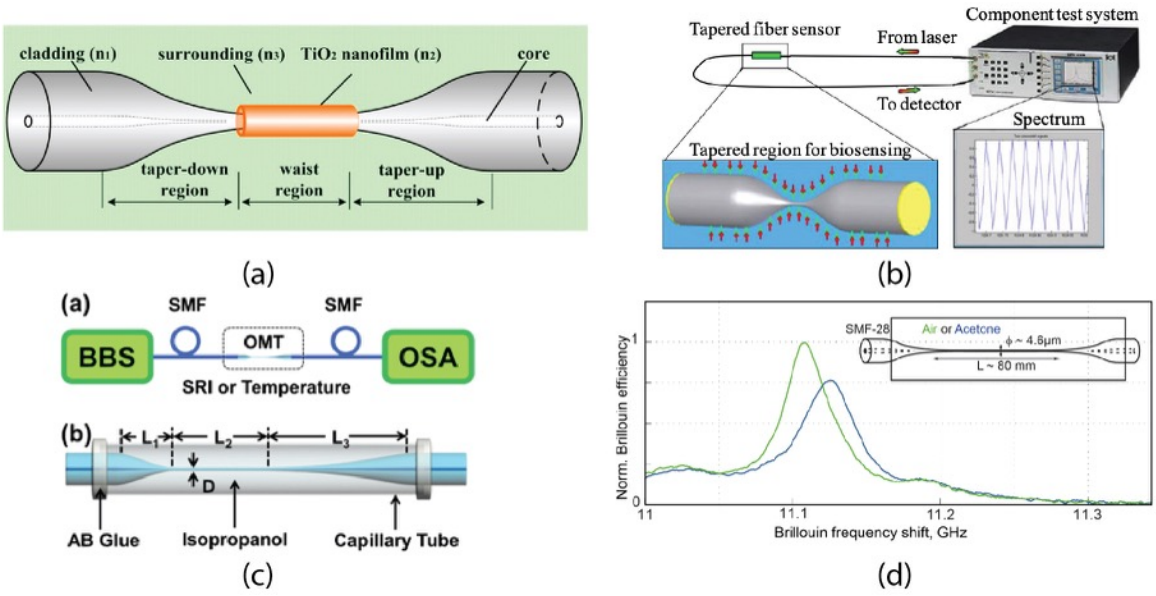

Figure 12 Straight-tapered-fiber-based sensors. (a) A refractive sensor based on a tapered fiber with TiO_2 nanofilm coating [45]. (b) A biosensor based on a tapered fiber with antibody coating [46]. (c) A Temperature sensor based on a tapered in an isopropanol environment [47]. (d) A liquid-property sensor based on a tapered fiber using the backscattering Brillouin phenomenon. The sensor can give mechanical property of the surrounding liquid [48].

Figure 12 (a) shows a high sensitivity refractive index sensor based on a TiO_2 coated tapered fiber [45]. The ~50 nm thick TiO_2 is coated onto the tapered fiber using the atomic layer deposition (ALD) technology. Since the nanofilm has a higher refractive index than the silica fiber taper, the light cannot be confined by total internal reflection. The nanofilm acts as a Fabry-Perot cavity. The transmission spectrum of the sensor is related with the environmental refractive index. When the environmental refractive index increases the whole spectrum will red shift. A sensitivity of 7096 nm/RIU was demonstrated. A tapered-fiber-based biosensor is shown in Figure 12 (b) [46]. To fabricate the sensor, a layer of antibody was coated onto the surface of a tapered fiber whose waist diameter is ~10 μm. When a broad-band light is input into the tapered fiber, the interference between the HE_{11} and HE_{12} optical modes will cause fringes in the transmission spectrum. When

an antigen layer is attached to the antibody, the refractive of the coating at the tapered fiber surface will be changed, which will cause a shift in the spectrum. As a result, the sensor can be used for label-free biomolecule detection. Figure 12 (c) shows a tapered-fiber-based temperature sensor [47]. To fabricate the sensor, a 7.2 μm diameter MF was inserted into a capillary filled with isopropanol (IPA). Similar to the sensor shown in Figure 12 (b), because of the interference between the fundamental HE_{11} mode and the higher order modes fringes can be seen in the output optical spectrum. When the temperature changes, it will change the refractive index of the IPA which will cause the shift of the output optical spectrum. The sensor has shown a temperature sensitivity of ~3.88 nm/◦C. A tapered fiber sensor based on the backscattering Brillouin phenomenon is shown in Figure 12 (d) [48]. The backwards Brillouin scattering is generated when the light is back scattered by the surface acoustic wave on the tapered fiber waist. The frequency of the backscattering Brillouin signal is related with the mechanical property of the environment. In the example shown in Figure 12 (d), when the environmental medium is changed from air to acetone, a 14 Hz frequency shift was observed.

1.3.1.3.2 Micro-particle manipulation using the straight tapered fiber

Tapered fibers offer a strong transverse confinement of the guided fiber mode while exhibiting a pronounced evanescent field surrounding the fiber. This unique combination allows to efficiently couple particles on or near the fiber surface to the guided fiber mode, making tapered optical fibers a powerful tool for their detection, investigation, and manipulation [49]. In Figure 13 (a), a 0.95 μm diameter straight tapered fiber was used to trap and propel polystyrene particles with a diameter of 3 μm in water. The particles were trapped at the waveguide surface by the optical gradient force, which is directed toward the surface, and were then propelled along the surface by the optical scattering force, which occurs in the direction of light propagation [50]. In Figure 13 (b) a straight tapered fiber (600 nm diameter) is used to trap and propel biological samples, in this case, E. Coli (length: 1.8 μm, diameter: 500 nm) in a fluidic environment [51]. The evanescent field of the straight tapered fiber can also be used for atomic trappings. In Figure 13 (c), a 500 nm diameter tapered fiber is used to trap cold cesium atoms [49]. The trapping force is the optical dipole force exerted by the evanescent field. The capability of the tapered fiber to detect, spectroscopically investigate, and mechanically manipulate cold atoms made it a powerful tool in quantum optics and cold-atom physics. Other than the optical force, the evanescent field can also exert photophoretic force to the nearby particles, and achieve massive particle trapping and

manipulations. The photophoretic force is generated when the leaked light from the tapered fiber is focused onto the back side of the transparent particle and caused the local temperature to increase [52]. As shown in Figure 13 (d), a straight tapered fiber (~1μm diameter) is used to demonstrate massive SiO_2 particle manipulations based on the photophoretic effect [52].

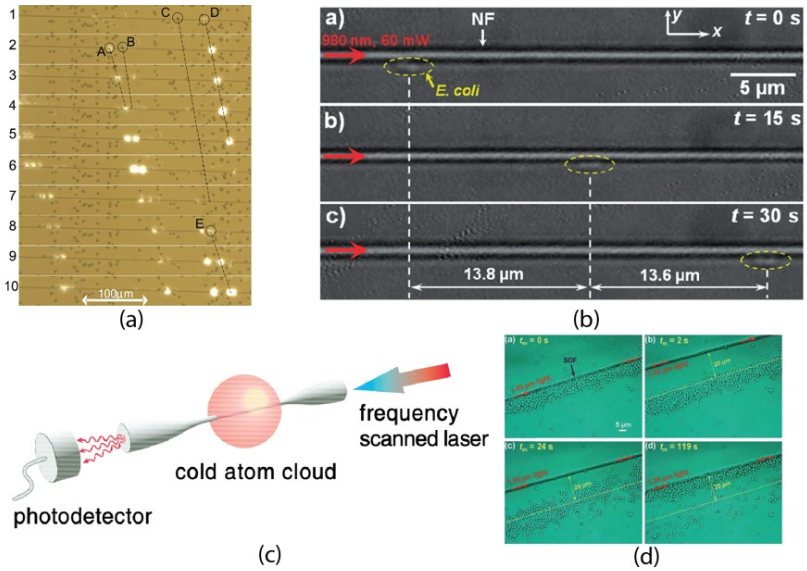

Figure 13 (a) and (b) show optical trapping and propelling of polystyrene particles [50]. and E.coli [51] respectively. (c) Trapping of cold cesium atoms using a straight tapered fiber [49]. (d) Massive micro-particle manipulation based on the photophoretic effect [52].

While the straight tapered fibers have been widely used in micro/nano-particle manipulations, they also have certain limitations due to the straight-line geometry.

i. A straight tapered fiber can only achieve in-plane particle manipulation. This limited its application in microfluidic applications where out-of-plane particle focusing is often desired.

ii. Since most of the particle manipulations happen at the bottom of a fluidic environment (Figure 13 (a), (b), and (d)), to approach these particles the straight tapered fiber needs to be lowered down to a distance that is very close to the bottom substrate. This may cause the one section of the straight tapered fiber to be in contact with the bottom substrate and cause unwanted optical scattering loss.

iii. The straight tapered fiber cannot selectively trap and propel a single desired particle from a group of particles. This is obvious in Figure 13 (a), where the straight tapered fiber was always in contact with several particles that were randomly distributed along the tapered fiber.

1.3.1.3.3 Integration of straight tapered fiber sensor with microfluidic devices

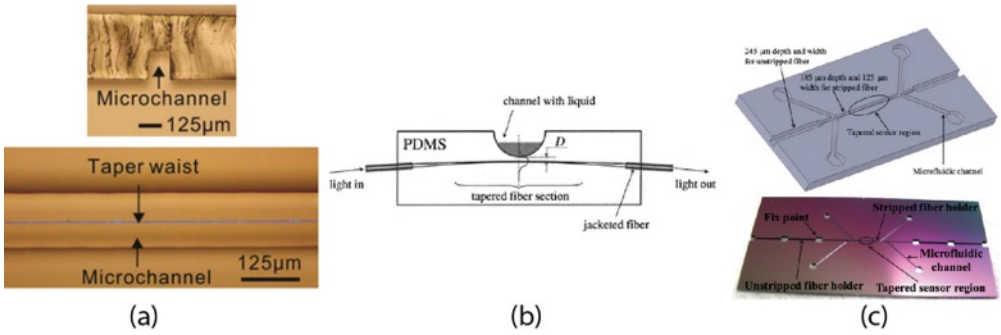

Figure 14 Examples showing the integration of straight tapered fiber sensor with microfluidic devices. (a) Photo showing a straight tapered fiber inserted in the microfluidic channel for chemical and biological sensing. [53] (b) A liquid refractive sensor based on a straight tapered fiber embedded below a PDMS microfluidic channel. [54] (c) A label-free biomolecule sensor based on a straight tapered fiber inserted in a silicon-based microfluidic channel. [46]

A tapered fiber has the advantages of small size (~ 1 μm at the waist section) and high sensitivity to the environmental changes (e.g. environmental refractive index change). A microfluidic device can manipulate fluids at micro-scale at a fast rate with high accuracy. Combining the tapered fibers with the microfluidic devices can allow accurate high throughput sensing of fluids. As shown in Figure 14 (a), Tong *et al.* integrated tapered optical fiber with microfluidic chips for ultra-sensitive chemical and biological sensing with very low sample requirement. The work demonstrated bovine serum albumin (BSA) measurement with a detection limit of 10 fg mL^{-1} (using a sample volume of only 500 nL) [53]. Polynkin *et al.* developed a microfluidic device [54] that can allow a highly accurate measurement of the refractive index of the fluids in the microfluidic channel as shown in Figure 14 (a). To fabricate the device, a straight tapered fiber was embedded a few micrometers below the microfluidic channel. The evanescent field of the tapered fiber was able to penetrate into the fluidic channel and will cause scattering loss due to the refractive index difference between the PDMS and fluids within the channel. The value of the scattering loss is higher when the refractive index difference between the PDMS and the fluids is larger. As a result, one can monitor the refractive index change of the fluids within the channel by looking at the optical transmission loss of the tapered fiber. Refractive index measurement accuracy as small as $\Delta n \approx 5 * 10^{-4}$ has been demonstrated. Tian *et al.* developed a silicon-based microfluidic device that can allow a tapered-fiber-based biosensor to be inserted into the microfluidic channel for label-free biomolecule detections, as shown in Figure 14 (b) [46]. The microfluidic channels were fabricated using photolithography and deep dry etching on silicon. The straight tapered fibers were fabricated using

the heat-and-pull method and can support two optical modes to propagate, the HE_{11} and the HE_{12} mode. To insert the tapered fiber into the channel, the two arms of the tapered fiber with the polymer coating (250 μm diameter) were tightly fit into the 245 μm wide silicon channels. After the tapered fiber is inserted, the silicon channel will be sealed by a PDMS cover. In the sealed silicon channel, the tapered fiber can be in direct contact with the fluids flowing by. Particularly in this case, the tapered fiber waist is coated with a layer of IgG antibody and can be used to detect whether the fluids flowing by contains the IgG antigen.

While the works mentioned above have demonstrated the great potential of integrating tapered fibers with microfluidic devices, neither the silicon-based microfluidic device nor the PDSM-based microfluidic device is an ideal solution for the following reasons:

i. ***The fabrication processes for both devices are challenging.*** For the PDMS-based microfluidic device, the tapered fiber needs to be embedded into the PDMS before it is cured. In this process the highly viscous uncured PDMS may break the thin tapered fiber waist. Furthermore, it is challenging to control the distance between the embedded tapered fiber and the microfluidic channel. If the distance is too far, the evanescent field will not be able to penetrate into the channel, and if the distance is too close, the tapered fiber might break into the channel and cause fluids leakage. For the silicon-based microfluidic device, during the insertion process of the tapered fiber, it is challenging to keep the thin tapered fiber waist straight and not touching the channel walls while also keeping it tension free and not breaking it.

ii. ***The tapered fiber within the microfluidic device is not replaceable after the fabrication.*** It is desired that when the tapered fiber in the microfluidic device is broken or contaminated one can easily replace the old fiber with a new fiber without breaking the microfluidic device. However, this is not possible with both microfluidic devices described above. For the fiber embedded in the PDMS microfluidic device, one cannot take the fiber out without breaking the PDMS channel. For the fiber inserted into the silicon channel, since the device is permanently sealed by a PDMS cover, one cannot access the silicon channel without breaking the PDMS cover.

iii. For the silicon-based microfluidic device, the fabrication process that involves photolithography and deep dry etching is ***expensive, time consuming, and is not widely accessible.***

1.3.1.3.4 Straight-tapered-fiber-based optical probes

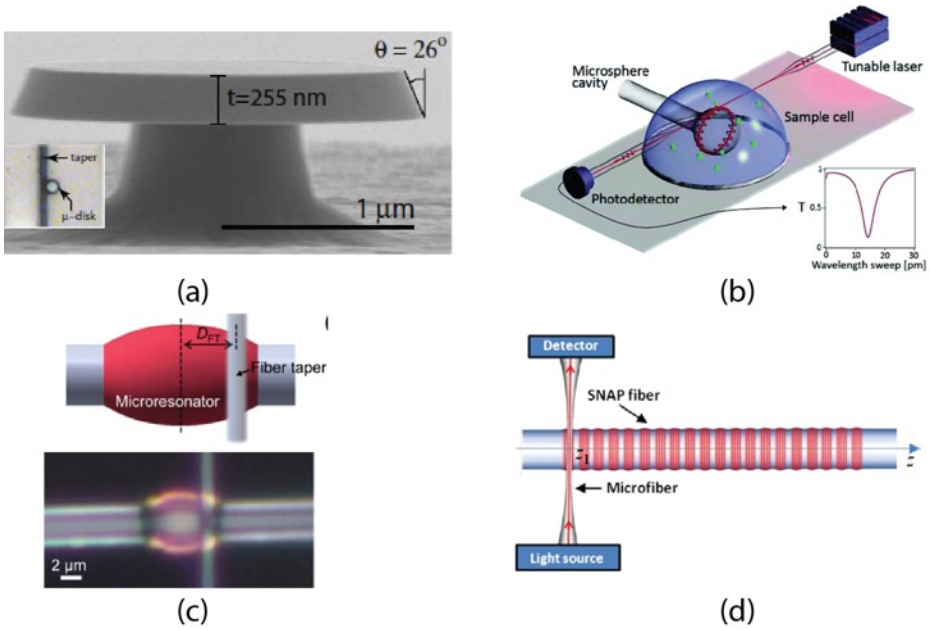

Figure 15 Different types of optical micro-resonators that are probed by the straight tapered fiber. (a) A 2 μm micro-disk optical resonator [55]. (b) A micro-sphere optical resonator [56]. (c) A micro-bottle optical resonator [57]. (d) A surface nanoscale axial photonic (SNAP) device [58].

Thanks to its large evanescent field and natural connections to regular single-mode fibers, the straight tapered fiber can be used as an optical probe to provide efficient light coupling into and out of micro-optic devices, particularly optical micro-resonators. In Figure 15 (a) shows an isolated 2 μm micro-disk resonator whose environment has been etched down [55]. The inset photo in Figure 14 (a) shows a straight tapered fiber coupling light into the micro-disk resonator. Figure 14 (b) shows the schematic of a micro-sphere-resonator based optical sensor used for single virus detections [56]. As shown in the schematic, a 2 μm diameter straight tapered fiber is used to couple light into and out of a ~100 μm micro-sphere. The input light from the tapered fiber will excite an equatorial whispering gallery mode (WGM) on the microsphere. The output light from the same tapered fiber will give information of the resonance wavelength of the equatorial WGM, which is sensitive to the binding of a single virus and can be used for single virus detections. Figure 15 (c) shows a single-mode lasing device based on a polymer bottle micro-resonator [57]. A straight tapered fiber is not only used to couple pump light into the bottle resonator, but also to bring optical losses to suppress the higher-order WGM and to achieve single-mode lasing. In the schematic shown in Figure 15 (d), a straight tapered fiber is used to couple light into a surface nanoscale axial

photonic (SNAP) device which is a standalone glass rod (~40 μm diameter) that has nanoscale surface variations [58].

Limitations of the straight tapered fiber probe.

i. Because of the flat straight-line profile, the optical device that the straight tapered fiber is approaching need to have certain clearance from the environment. Otherwise, the thick arms of the tapered fiber (regular fiber) may interfere the light coupling that happens at the thin tapered fiber waist. For example, when using a straight tapered fiber for monolithic in-plane device probing, the thick arms of the tapered fiber may interfere with the substrate or other devices. In fact, the reason that the surrounding environment of the micro-disk in Figure 15 (a) is etched down, is to prepare the device for the straight tapered fiber probing.

ii. While the straight tapered fiber probe can efficiently couple light into and out of an optical resonator device, the alignment between the straight tapered fiber and the resonator need to be carefully maintained and hence limited the sensing devices' portability. It is desired that the optical micro-resonator can be integrated with a tapered fiber and acting as a portable standalone sensing device.

1.3.2 Dimpled tapered fibers

As we have mentioned in the above section, when using a straight tapered fiber to approach an in-plane monolithic device its thick arms may interfere with the environment or other devices and cause unwanted optical losses. To solve this problem, another specially shaped optical fiber called the dimpled tapered fiber [9,10] can be used. The dimpled fiber will be discussed in this section.

1.3.2.1 Fabrication of dimpled tapered fiber

The fabrication process of a dimpled tapered fiber is shown in Figure 16. Briefly, after a straight tapered fiber is fabricated, its center waist section is first slightly relaxed by moving the two fiber clamps that is holding the arms of the tapered fiber slightly closer (~10 μm), as shown in Figure 16 (a). Then, a cleaned single-mode fiber covered with a thin layer of graphite powder is raised to first get in touch with the center of the relaxed tapered fiber waist, and then was further raised up for approximately 5 mm, while simultaneously relaxing the tapered fiber, as shown in Figure 16 (b). The dimple shape was then permanently fixed by annealing with a hydrogen torch, as shown in Figure 16 (c). The thin graphite layer on the mold fiber is to prevent the tapered fiber stick to

the mold at this annealing step. Finally, the relaxed tapered fiber is removed from the mold by the gentle pressure applied by a hydrogen flow, as shown in Figure 16 (d). The fabricated dimpled tapered fiber, as shown in the microscopic photos in Figure 16 (d) and (e), has a small protrusion at the center of the tapered fiber waist. As shown in the transmission in Figure 16 (f), after creating the dimple at the tapered fiber waist, an optical loss of around 8% was introduced to the tapered fiber.

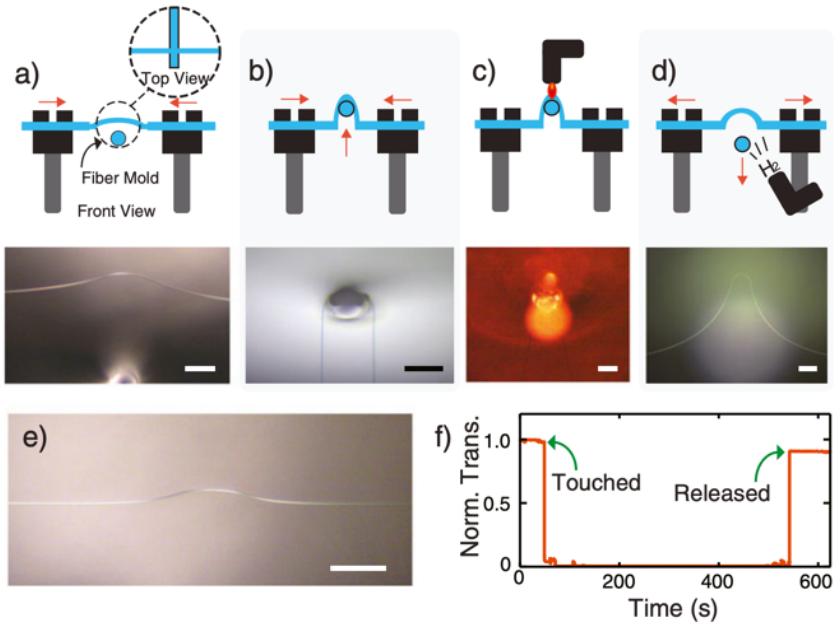

Figure 16 (a-d) Schematics showing the fabrication process of the dimpled tapered fiber. (e) Optical microscope image of the fabricated dimpled tapered fiber. (f) Recorded normalized real-time transmission during the fabrication of the dimpled tapered fiber. (a-f) are from the work [9]

1.3.2.2 Application of the dimpled tapered fiber

With the small protrusion, the dimpled tapered fiber can be used to probe closely spaced, planar integrated photonic devices without worrying about thick arms interfering with the environment or other devices [9,10]. In Figure 17 (a), the dimpled tapered fiber was able to approach the in-plane micro-disk optical resonator without touching the surrounding environment. In Figure 17 (b), the dimpled tapered fiber was able to selectively couple light into one of the twenty-five in-plane micro-disks but not coupling light into any of the neighboring disks [10].

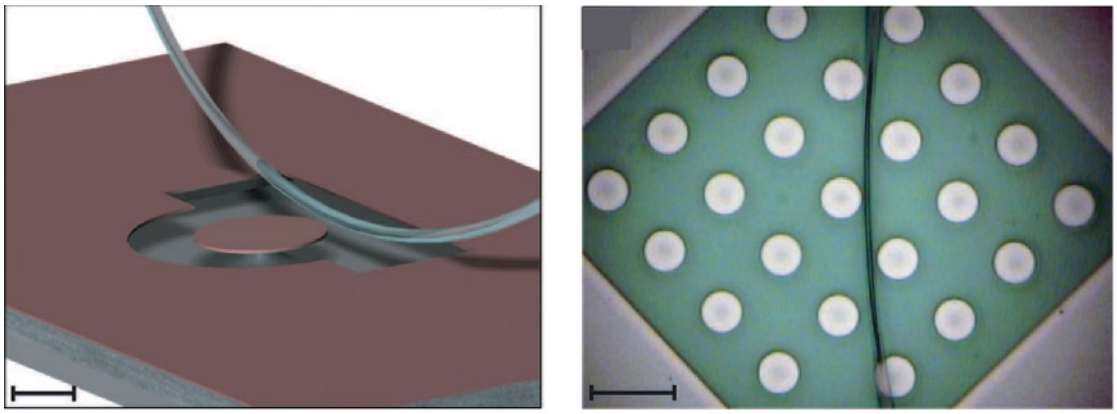

Figure 17 (a) Schematic of a dimpled tapered fiber coupling light into a micro-disk [10]. (b) Microscope image showing a dimpled tapered fiber probe coupling light into a micro-disk resonator [10].

1.3.2.3 Limitations of the dimpled tapered fiber

While the dimpled tapered fibers can solve the light-coupling problem faced by the straight tapered fibers as we have discussed above, its complex fabrication process that lacks controllability and repeatability made it challenging for other users to adopt the technic Some of the challenges that one might face when fabricating the dimpled tapered fiber is listed below:

i. In step 1 of the fabrication shown in Figure 16 (a), when applying the graphite powder to the optical fiber mold, it is challenging for a user to control the amount of graphite power covered on the optical fiber mold. If the graphite powder layer is too thick, it will not be fully burnt during the flame annealing process and will become a contamination to the dimpled tapered fiber and cause additional optical loss. If the graphite powder layer is too thin, the dimpled tapered fiber will stick to the glass mold and cannot be separated.

ii. In step 2 of the fabrication shown in Figure 16 (b), when using the mold to depress the center tapered fiber waist, it is challenging for a user to coordinate the movement of the mold and the two fiber clamps. If the two fiber clamps are moving too fast comparing to the mold, the tapered fiber waist will be overly relaxed and cannot form the desired dimple shape. If the two fiber clamps are moving too slow, the increased tension within the tapered fiber waist might cause breakage of the tapered fiber.

iii. In step 3 of the fabrication shown in Figure 16 (c), when using the flame to anneal the dimple shape, it is challenging for a user to determine the duration of the annealing process. Especially considering that, as shown in Figure 16 (f), the real-time optical transmission

is close to zero and cannot be used to monitor the process. If the flame annealing duration is too long, the heated part might become too soft and deform more than desired, or even melt and stick to mold. If the flame annealing duration is too short, the dimple shape will not be permanently fixed.

1.3.3 Tapered fiber ring resonators

Tapered fiber ring resonators are optical micro-resonators that composes of purely glass fibers. As shown in in Figure 18, three types of tapered fiber ring resonators have been demonstrated [59], including, the tapered fiber loop resonator, the tapered fiber knot resonator, and the tapered fiber coil resonator. Different from other resonators we have previously discussed (e.g. on-chip resonators, bottle resonators, and sphere resonators), the tapered fiber ring resonators do not have an external resonator structure, instead the ring resonator is formed by the tapered fiber itself and it is naturally coupled to the input and output tapered fiber [23]. Details of the three tapered fiber ring resonators, the tapered fiber loop resonator, the tapered fiber knot resonator, and the tapered fiber coil resonator are detailed in the following section.

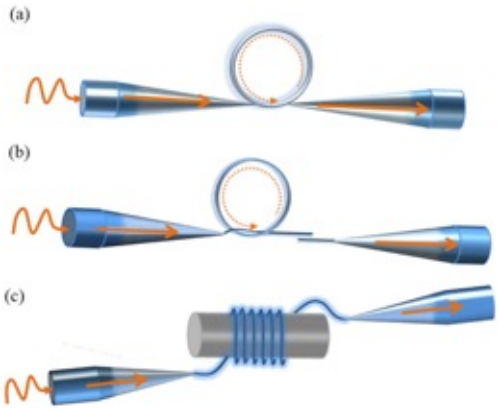

Figure 18 Schematics showing the three types of ring resonators, (a) tapered fiber loops, (b) tapered fiber knots, and (c) tapered fiber coils [59].

1.3.3.1 Fabrication of the tapered fiber ring resonators

Tapered fiber loops

Two fabrication methods for the tapered fiber loops have been demonstrated. [27,31]In one method [27], as shown in the upper figure of Figure 18, after the fabrication of a straight tapered fiber, the center waist of the tapered fiber was first relaxed by 1 mm, and then a torsion was applied to the waist by rotating the regular fiber arms of the tapered fiber, a loop with multi-twisted

connection part was formed (Figure 19 (a)). To form the loop structure with a single crossing at the cross-section as shown in Figure 19 (b), a tension was applied to the multi-twisted loop to dissemble the multi-twist connection. In the other method [31], as shown in the lower figure of Figure 18, one end of a straight tapered fiber is mounted on a rotational stage while the other end is mounted onto a 3D translation stage. By manipulating the translation stages and the rotation stage simultaneously, the straight tapered fiber can be bent into a self-touching loop. The flat connection of the two arms of the loop is ensured by the van der Waals force. The figure of merit most often quoted for an optical resonator is the Q-factor, which is the ratio of the resonance wavelength to the full width at half-maximum (FWHM) of its resonance spectra [60]. To the beset of the author's knowledge the highest Q-factor for a tapered fiber loop resonator is around 630,000.

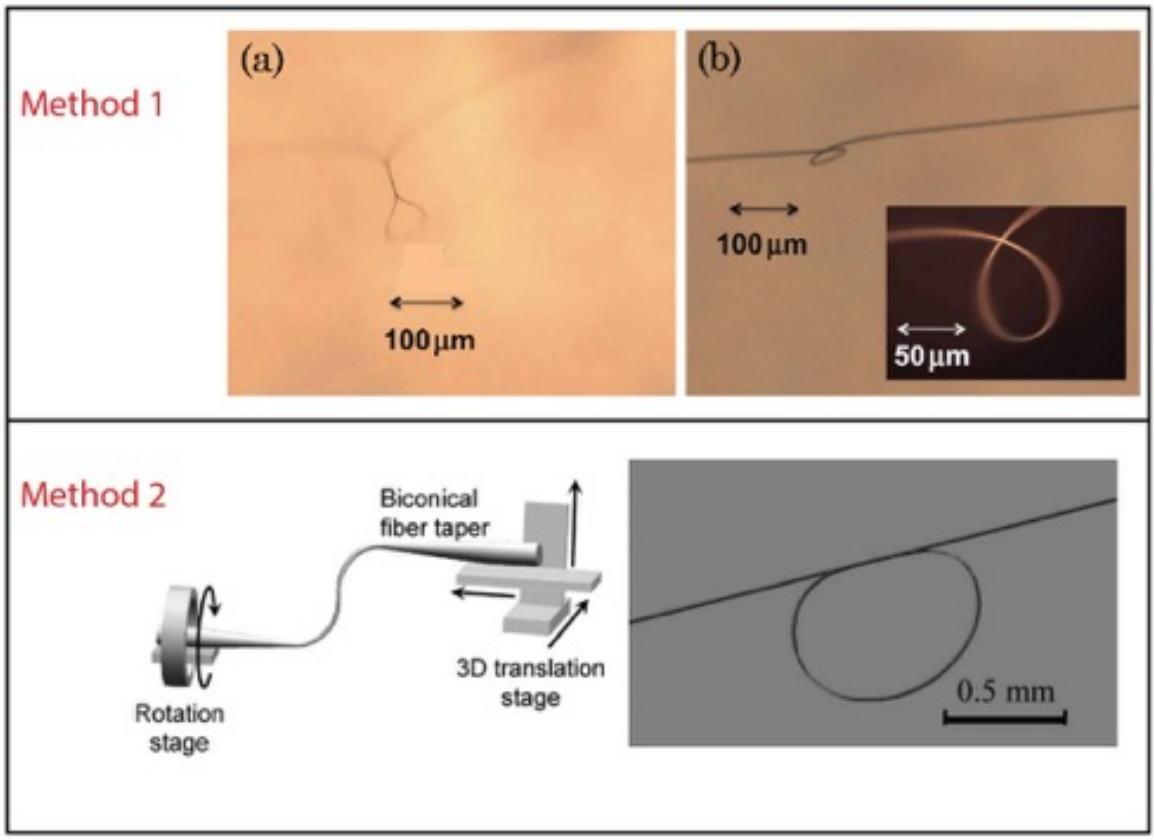

Figure 19 Schematics showing the two fabrication methods of the tapered fiber loops. The upper figure [27] and the lower figures [31] show the two methods respectively.

Limitations of the tapered fiber loops:

i. Tapered fiber loops fabricated by both methods are susceptible to environmental fluctuations and can be dissembled easily.

ii. The loop fabricated by the first method has a angled arm-connection, which resulted in a low optical coupling efficiency and low optical quality factor for the resonator.

iii. For the loop fabricated by the second method, since its flat arm-connection is maintained by the weak van der Waals force, it can only sustain a large loop radius. If the loop is bended to a smaller radius, the van der Waals force will no longer be able to maintain the increased strain within the arms.

Tapered fiber knots

Two fabrication methods of the tapered fiber knots have been demonstrated. In the first method, as shown in the upper figure in Figure 20, the tapered fiber knot was fabricated by manually knotting a free-standing tapered fiber (part of a straight tapered fiber) using a polymer microfiber and adhering (the adhering force is the van der Waals force) it to another free-standing tapered fiber. In the second method, as shown in the lower figure in Figure 20, a double-ended straight tapered fiber was used to fabricate the tapered fiber knot [23]. First a millimeter size large knot was made by knotting the regular fiber arms of a straight tapered fiber, then the knotted regular fiber arms were carefully mounted to two translation stages manually. The final micro-size tapered fiber knot is formed by using the translation stages to pull the two regular fiber arms and shrinking the diameter of the knot. To the best of the author's knowledge the highest Q-factor demonstrated by the tapered fiber knots is around 100,000 [23].

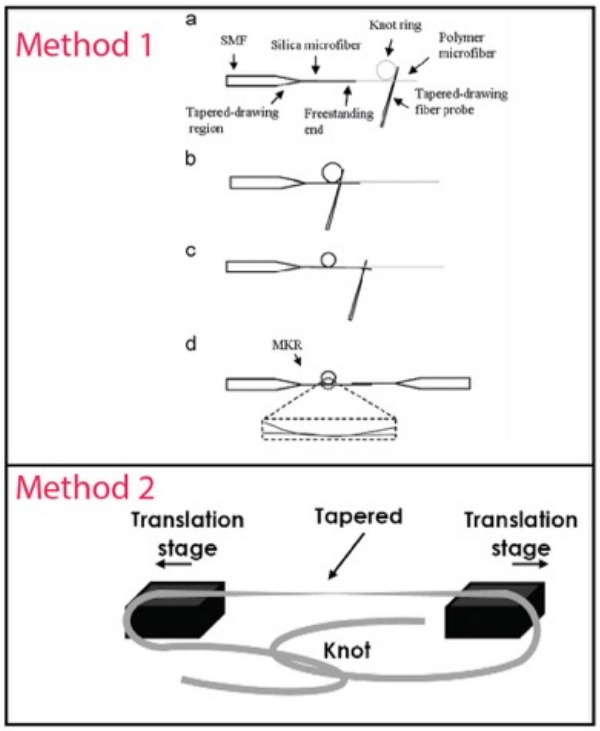

Figure 20 Schematics showing the two fabrication methods of the tapered fiber knots. The upper figure [61] and the lower figures [23] show the two methods respectively.

Limitations of the tapered fiber knots:

i. The first fabrication method relies on the weak van der Waals force to connect the tapered fiber knot to another tapered fiber. This weak connection makes the structural integrity of the tapered fiber knots fabricated using the first method susceptible to environmental disturbance and is difficult to be directly used in real-world applications.

ii. Both methods involve manual manipulation of delicate tapered fibers, and these fabrication processes can be challenging even for a trained user.

Tapered fiber coils

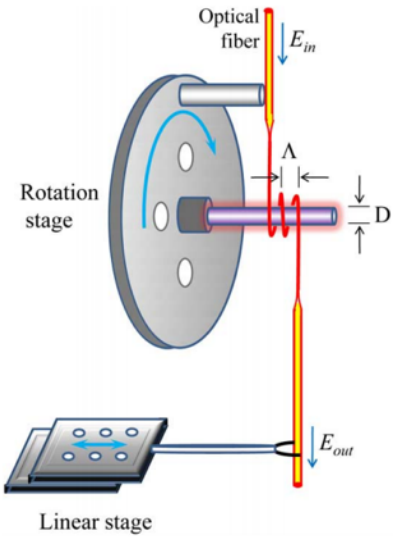

Figure 21 Schematic showing the fabrication setup of a tapered fiber coil [62].

Tapered fiber coils are fabricated by wrapping a long-straight tapered fiber around a rod structure. The rod should have a lower refractive index than the tapered fiber to ensure the light being guided within the tapered fiber. The distance between each coil, which is controlled by the angel between the microfiber and the rod in the fabrication setup as shown in Figure 21, should be within the coupling range of the evanescent field of the tapered fiber to ensure an efficient light coupling. To the best of the author's knowledge the highest Q-factor demonstrated by the tapered fiber coil is around 220,000 [62].

Limitation of the tapered fiber coils:

While the rod that the fiber coil is mounted on provided the coil better structural stability compared to the tapered fiber loop and knot, the rod has also limited its mobility which is a desired feature in many applications.

1.3.3.2 Sensing applications of the tapered fiber ring resonators

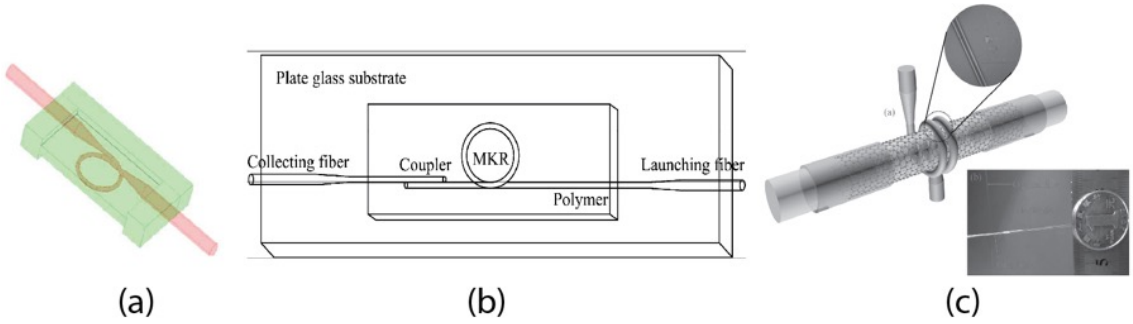

Figure 22 Schematics showing different the different applications based on the tapered fiber ring resonators. (a) a tapered fiber loop based refractive index sensor [30], (b) a tapered fiber knot based temperature sensor [24], (c) a tapered fiber coil based electrical current sensor [63].

In a tapered fiber ring resonator input light that is certain wavelengths will circulate within the ring resonator, which will result in an output optical spectrum with resonances. The free spectral range (FSR) of the resonance signal which represents the wavelength difference between two successive minima in the resonator transmission can be written as: $FSR = \frac{\lambda^2}{n_{eff}\,L}$, in which, λ is the light wavelength, n_{eff} is the effective index of a mode, and L is the cavity length (in this case the circumference of the ring resonator) [24]. The relation between the effective mode index n_{eff}, the cavity length L, and the FSR is exploited for different sensing applications. Figure 21 (a) shows a tapered fiber loop based refractometric sensor [30]. To fabricate the sensor, a tapered fiber loop is embedded in a low-refractive-index polymer UV375 (green). The polymer coating has a thick edge that supports the integrity of the structure and a thin center layer that allows the evanescent field of the tapered fiber loop to be exposed into the environment. The working principle of the sensor is that when the environmental refractive index changes, it will cause the effective mode index n_{eff} to change, which, according to the relation $FSR = \frac{\lambda^2}{n_{eff}\,L}$, can be read out from the optical transmission spectrum. The sensor has demonstrated a sensitivity as high as 700 nm/RIU. Figure 22 (b) shows a tapered-fiber-knot based temperature sensor [24]. To fabricate the sensor, a tapered fiber knot is stick to a 20 μm low-refractive-index polymer through the van der Waals force. The thin polymer layer is supported by a glass substrate. When the temperature changes, the refractive index change of the polymer will cause the effective mode index n_{eff} of the knot resonator to change, and the expansion of the polymer due to the heating will cause the cavity length L of the

knot resonator to change. These changes will cause the FSR of the resonance spectrum to change, which can be used for temperature sensing. The knot-based temperature sensor has demonstrated a sensitivity as high as 0.27 nm/°C. Figure 22 (c) shows a tapered fiber coil based current sensor [63]. The sensor is fabricated by wrapping a tapered fiber coil around a glass fiber coated with a monolayer graphene sheet and two gold electrodes. When a current is passing through, the graphene layer will generate electrical resistance heating and cause the temperature of the graphene to change. Similar with the tapered-fiber-knot based temperature sensor, this temperature change of the graphene can be read out from the transmission spectrum of the tapered fiber coil. An ultra-high sensitivity of ultra-high sensitivity of 67.297 $\mu m/A^2$ has been demonstrated [63].

1.3.4 D-shape optical fibers

As we have mentioned earlier, other than the straight tapered fiber, the D-shape fiber is another type of specially shaped fiber that can expose the light guided in the fiber core to the environment. In this section the fabrication methods and applications of the D-shape fiber are reviewed.

1.3.4.1 Fabrication of D-shape fibers

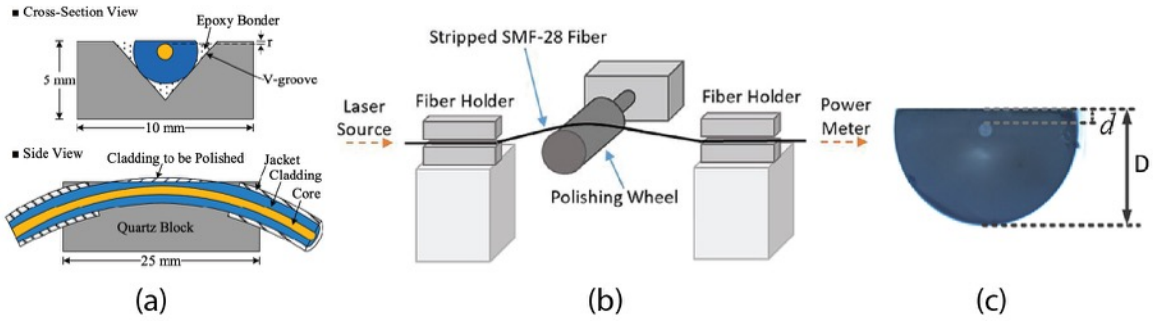

Figure 23 Schematics showing the fabrication methods of the D-shape fiber. [64] In (a), the optical fiber was embedded in a quartz supporting substrate during the polishing. In (b), the optical fiber was polished by a polishing wheel. [65] (c) A microscope image of the cross section of the D-shape fiber. [33]

A D-shape fiber can be fabricated from a single-mode optical fiber through side-polishing. The side-polished fiber, as shown in Figure 23 (c), will have a cross section that looks like a D shape, and hence the name D-shape fiber. Two types of side-polishing methods have been developed [64–66]. In the one method, as shown in Figure 23 (a), a slightly curved single-mode optical fiber is first being mounted onto a supporting substrate using epoxy, the substrate in this case the quartz block. Then the fiber section that is outside the quartz block is being polished using

a flat polishing plate [64]. The downside of this fabrication method is that it is difficult to remove the fabricated D-shape fiber from the polishing setup. As a result, D-shape fibers fabricated using this method often have to be used together with the bulky substrate which greatly reduced their portability and flexibility. In the other method, as shown in Figure 23 (b), a single-mode optical fiber is held by two fiber holders and is stretched and partially wrapped around a polishing wheel [65]. During the polishing, the rotating polishing wheel will polish off the cladding of the fiber section that is wrapped around it. Different from the first polishing method, the second polishing method allows the fiber to be removed from the polishing setup after the fabrication and be used as a free-standing regular fiber Because of this, the second polishing method is preferred in most of the applications. One limitation of these two fabrication methods is that they can only fabricate double-ended D-shape fibers not single-end D-shape fibers. The single-end geometry can enable the D-fiber to be used like a probe that have both the light input and output at the same end. Such probe-like configuration is beneficial when the space for implementing the D-fiber is limited. A fabrication method of single-end D-shape fiber is yet to be demonstrated.

1.3.4.2 Applications of the D-shape fibers

1.3.4.2.1 Lossy-mode-resonance-based D-shape fiber sensors

The lossy mode resonance (LMR) is first discussed in the seminal work by Batchman *et al.* in 1982 [67], in which he proved that at certain cladding thicknesses, optical wavelengths, and light incidence angles the propagation of light in semiconductor cladded waveguides will experience some attenuation maxima. The LMR phenomenon is further explained by M. Marciniak *et al.* in his work in 1993 [68], in which he pointed out that the attenuation maxima is due to the coupling between waveguide modes and a specific lossy mode of the semiconductor thin film. However, afterwards, little attention was paid to the lossy mode resonance for decades. One possible reason for the limited development of the LMR technology during this period might because the LMR phenomenon were mainly demonstrated in on-chip waveguides. And since there lack an efficient way to couple light into and out of the on-chip waveguide at that time, the LMR technology was not able to be fully exploited.

In 2010 Villar *et al.* demonstrated a lossy-mode-resonance-based optical fiber sensor for sensing applications [69]. Unlike the on-chip waveguides, optical fibers can naturally and efficiently transmit light and excite the LMR signals. Since then, the idea of integrating LMR phenomenon with fiber optics has attracted a great many interests and have found a large number

of sensing applications [32,69–77]. However, most of these LMR sensors are fabricated on the core of a multimode fiber [78,79], as shown in Figure 24 (a). The symmetric cylindrical fiber core does not allow the sensor to differentiate the TE and TM lossy mode resonances and has limited the sensor's sensitivity. In 2014, the work by Arregui *et al.* demonstrated that the sensitivity of the LMR sensor can be dramatically increased by switching to a D-shape fiber [80]. The asymmetric D-shape fiber, as shown in Figure 24 (b), can allow the differentiation of the TE and TM lossy mode resonances. The D-shape LMR sensor has demonstrated a sensitivity as high as 304 360 nm/RIU, which has surpassed the surface plasmon resonance based sensors [32].

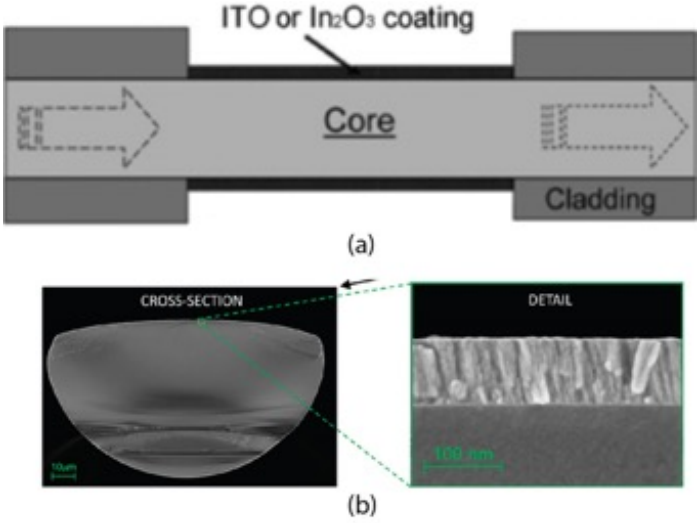

Figure 24 (a) Schematic showing a lossy-resonance-resonance sensor based on a cylindrical multi-mode fiber. [81](b) SEM images of lossy-mode-resonance sensor based on a D-shape fiber [32].

Working principle of the lossy-mode-resonance-based D-shape fiber sensors

An LMR-based D-shape fiber is fabricated by coating a layer of optically lossy material, in this case ITO, onto the polished surface of the D-shape fiber, as shown in Figure 24 (b). The D-shape fiber with the ITO film coating can support both the core mode (HE_{11}) and the film mode (TE_{11}). Figure 25 shows the simulation results of electric field intensity of the core mode and the film mode at the cross section of the D-shape fiber at different wavelengths. At lower wavelengths (<1420 nm), the HE_{11} mode is confined within the core and the TE_{11} mode is confined within the film layer. At the wavelength of 1420 nm, for the electric field distribution of the HE_{11} mode, a subtle yellower color showed up at the proximity of the thin-film. This indicates that part of the power transmitted by the core mode is coupled to the ITO thin-film, which corresponds to the LMR. For wavelengths larger than 1420 nm, the HE_{11} mode is again confined within the core, and

the TE_{11} mode became a radiation mode and is no longer supported by the film layer. These results indicate that, if a broadband light source whose wavelength range covers the wavelength from 1170 nm to 1690 nm is input into the ITO coated D-shape fiber, we will see an attenuation maxima in the output spectrum at the wavelength of 1420 nm, because part of the light is coupled into the ITO film layer and is absorbed by the optically lossy ITO film. The optical spectrum with the attenuation maxima is called the LMR spectrum, and the wavelength that is corresponding to the attenuation maxima is called the LMR wavelength. The LMR wavelength is sensitive to the environmental refractive index changes. When the environmental refractive index increases, the LMR wavelength will increase and vice versa.

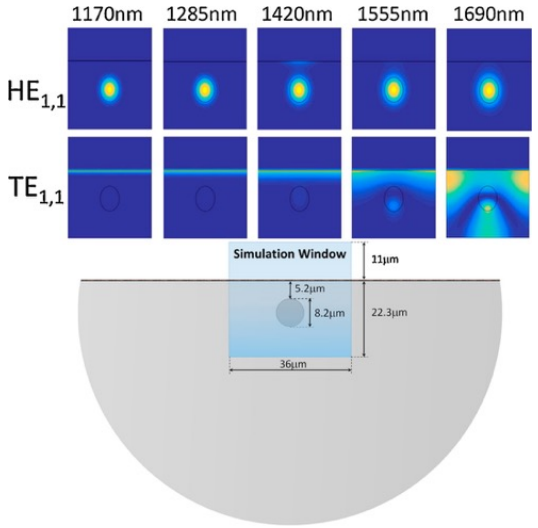

Figure 25 Simulation results of the optical modes of a D-shape lossy mode resonance sensor. [32]

Applications of the lossy-mode-resonance-based D-shape fiber sensor

A characterization setup for the lossy-mode-resonance-based D-shape fiber sensor is shown in Figure 26 (a). A broadband light whose polarization is controlled by the polarization controller is input into the LMR sensor, the output spectrum is readout using an optical spectrum analyzer [82]. Figure 26 (b) shows the measured LMR spectrum using the setup. The TE and TM polarization resonance spectra were measured using TE and TM polarized input light respectively. The unpolarized resonance spectrum was measured by removing the polarization controller. The unpolarized resonance spectrum measured from the D-shape fiber is similar to the LMR spectrum measured from a cylindrical multi-mode fiber based LMR sensor which cannot differentiate the TE and TM mode. From the comparison of the spectra in Figure 26 (b), it is clear that the TE or

TM resonance spectrum of the D-shape fiber has a much better visibility than that of a cylindrical multi-mode fiber based LMR sensor [82]. Figure 26 (c) shows LMR wavelength shift of the sensor at different refractive index. The sensor has a higher sensitivity when the refractive index difference between the film coating and the environmental refractive index is larger. At the refractive index range between ~1.447 to ~1449 the sensor demonstrated a sensitivity as high as 304 361 nm/RIU. Since the lossy-mode-resonance-based D-shape fiber sensor has just been demonstrated recently in around 2014 [80], it has mainly been demonstrated for refractive index sensing and not many other applications yet. More applications taking advantages of the high sensitivity of the lossy-mode-resonance-based D-shape fiber sensor is yet to be demonstrated.

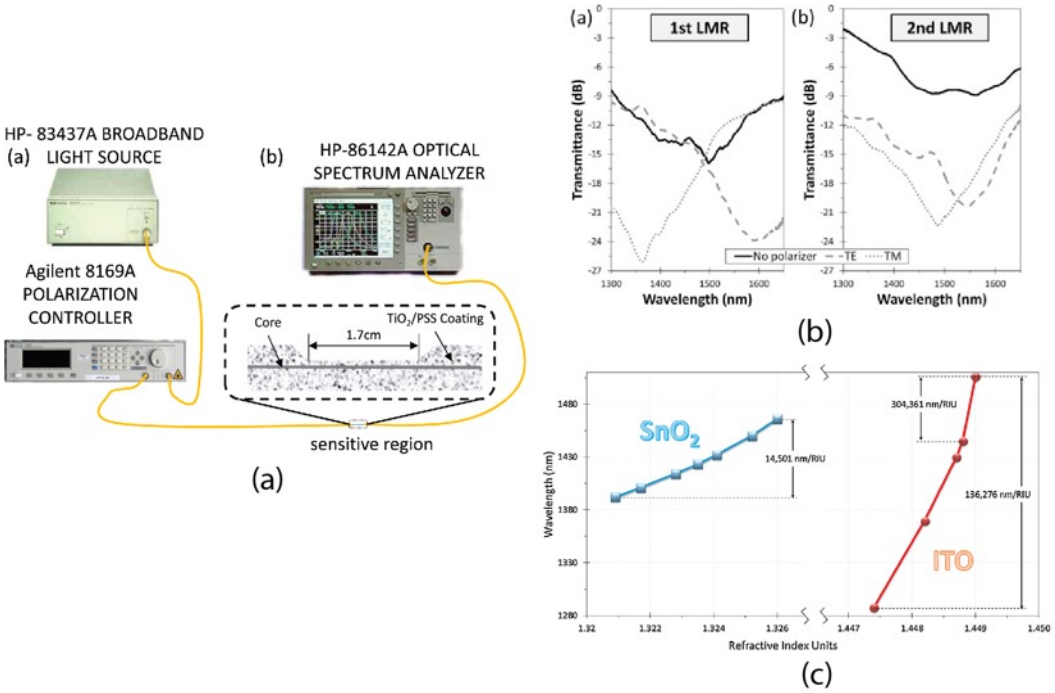

Figure 26 (a) A characterization setup of the lossy-mode-resonance-based D-shape fiber sensor. [82] (b) The first and second LMR modes for TE, TM and unpolarized light input. [82] (c) Refractive index measurement using the LMR sensor. [83]

1.3.4.2.2 Other D-shape fiber sensors

Violakis *et al.* demonstrated a magnetic field sensor based on a ferrofluid encapsulated D-shape optical fiber as shown in Figure 26 (a) [84]. The sensor has demonstrated an azimuthal dynamic range of the order of 12 dB with sensitivity of 0.2 dB/° and magnetic field flux sensitivity of 0.015 dB/Gs. Zhang *et al.* demonstrated a surface-enhanced Raman scattering (SERS) sensor based on D-shape fiber as shown in Figure 27 (b) [85]. The SERS fibers were created by mixing 20 μL of

silver nanoparticles with 5 μL of 0.1 mM rhodamine 6G (R6G) and drying a drop of this solution on the fiber under ambient conditions. The D-shape fiber sensor can provide a SERS active layer with surface area as much as 1 cm x 8 μm, which is around 3 orders of magnitude larger than the SERS sensor based on end-polished fibers. Nayk *et al.* demonstrated a plasmonic sensor based on a graphene-coated D-shape fiber as shown in Figure 27 (c) [86]. The sensor demonstrated a sensitivity of 6800 nm/RIU and a resolution of 8.05×10^{-5} RIU. Sherwood *et al.* demonstrated a novel optical fiber sensor based on micro-ring resonators fabricated on side-polished fiber on the D-shape fiber as shown in Figure 27 (d) [86]. The polymer ring resonator was fabricated using the two-photon polymerization at a position that can allow evanescent light coupling between the fiber and the ring.

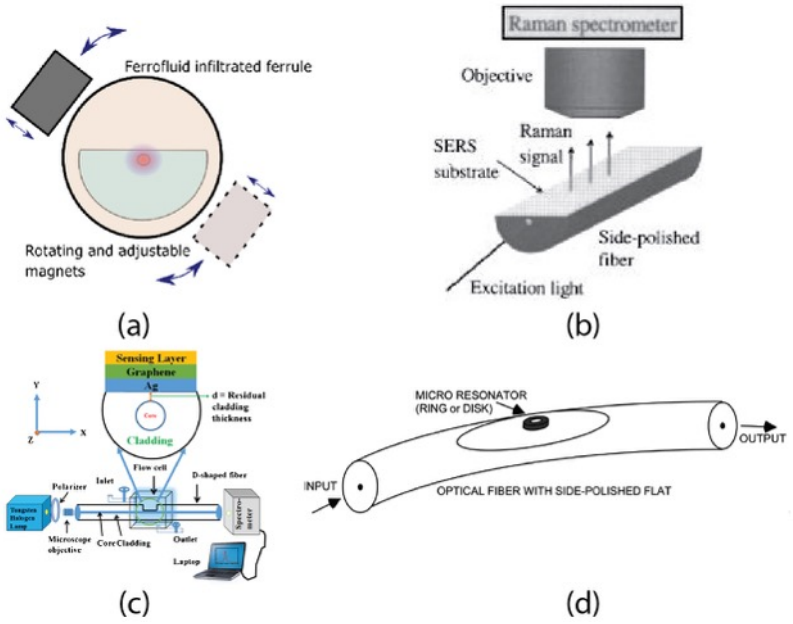

Figure 27 Schematics showing different types of D-shape fiber based optical fiber sensor. (a) a magnetic field sensor [84], (b) a SERS sensor [85], (c) a plasmonic sensor [86]. (d) a micro-ring resonator sensor on a D-shape fiber [87].

1.4 MOTIVATION OF THIS DOCTORAL RESEARCH

A regular fiber can deliver light to a point of interest with low transmission loss. This superior light delivering capability has enabled a variety of applications, most notably, boosting the development of the telecommunication industry in the last few decades. However, many optical sensing and actuation applications require that after the light has been delivered to a specific point, the light can interact with the matter around it [9,88]. In order to achieve light-matter interactions

without sacrificing the benefits of the regular fibers, an ideal solution is the specially shaped optical fiber. However, current research on the specially shaped fibers is far from complete. The most important challenges that motivate this doctoral research is summarized below:

- **Challenge 1: Low optical transmission of specially shaped optical fibers.**
  The low transmission of specially shaped fibers is due to the high optical coupling loss between the specially shaped fiber section and the regular fiber section. The high coupling loss is because light is susceptible to the geometries of the lightguide, a rough lightguide surface will cause serious optical scattering loss; an abrupt geometry change in the lightguide can cause serious optical radiation loss [18]. An efficient coupling is especially challenging when the specially shaped fiber has a sub-wavelength dimension, such as for tapered fibers discussed in section 1.3.1. New designs of specially shaped fibers that can efficiently couple light between the regular fiber part and the special-shape part need to be developed based on an enhanced fundamental understanding of the optical properties of specially shaped fibers.
- **Challenge 2: Specially shaped fiber designs based on fiber tips are far from fully investigated.** Fiber-tip-based specially shaped fibers can have a probe-like design, which will endow it with higher mechanical strength, and further reduce its size. More work needs to be done to develop specially shaped fibers with such designs.
- **Challenge 3: The areas and lengths, over which light interacts with matter, are limited in the specially shaped fibers.** A majority of specially shaped fibers allows light to interact with the matters around it through the optical near-field effects. The optical near-field effects quickly decay with the distance from the fiber surface and are generally limited within a few micrometers. As a result, the strength of light-matter interactions is limited, especially compared with that enabled by free-space propagating light. An enhanced interaction length is desired in the special shape of the fiber, in order to boost the light-matter interactions. A common and straight forward solution is to increase the length of the specially shaped fiber, so that the near-field interaction can take place along a longer fiber length, which can amplify the light-matter interactions. However, increasing the length will not help if the matters of interest are not uniformly distributed in the medium, but are only located at specific places. For example, in the case of straight tapered fiber probe discussed in section 1.3.1.3.4, solely increase the length of the tapered fiber, will not

help it to approach in-plane devices more effectively. More novel designs that can facilitate the light-matter interactions are yet to be developed.

- **Challenge 4: The meager material selections has limited the light-matter interactions of the specially shaped fibers.** Other than using the special shape of the fiber to facilitate and amplify the light-matter interaction, it is also possible to use new materials to achieve this goal. One way to integrate new materials to glass fibers is by coating a thin layer of the material to the specially shaped fiber surface. The coated material can not only facilitate and amplify the light-matter interactions that happens at the surface of the material, it can also endow the specially shaped fibers with enhanced light manipulation capabilities, such as the metal coating enabled surface plasmonic resonances [85] and the semiconductor material enabled lossy mode resonances [89]. Since different material can facilitate different light-matter interactions, more research on materials for specially shaped fibers need to be done.
- **Challenge 5: The existing fabrication methods for the specially shaped fibers are far from optimized.** Existing fabrication systems for the specially shaped fibers lacks repeatability and controllability, which have hindered the further advancement of the specially shaped fibers. Especially, it is difficult to use the existing fabrication systems to achieve novel designs of specially shaped fibers. Both the physical setup and the software used to in the fabrication system need to be developed and improved.

1.5 OBJECTIVES AND SCOPE OF THE DISSERTATION

The overall goals of this dissertation are to further the fundamental understanding of specially shaped fibers and to develop novel specially shaped fibers for different applications. In addition, the final part of this dissertation work proposed a microfluidic platform that can potentially improve the light-matter interactions of the specially shaped fibers in fluidic environments. Specific objectives include the following:

1. **Develop novel designs of specially shaped fibers with enhanced light-matter interactions.** This addresses challenges 2 and 3.
2. **Develop innovative methods to create specially shaped fibers based on fundamental understanding of light manipulation.** This addresses challenges 1, 2, and 5.

3. **Expand and enhance the functionalities of the specially shaped fibers.** This addresses challenges 2 ,3, and 4.

To achieve the abovementioned objectives, three major research thrusts are carried out in this dissertation work.

Research thrust 1: System development, experimental study, and modeling of the specially shaped optical fiber fabrication setups. This thrust addresses Specific Objectives 1.

Research thrust 2: Development of specially shaped optical fibers for integrated photonic, microfluidic, and optical sensing applications. This thrust addresses Specific Objectives 2 and 3.

Research thrust 3: System development and experimental study of a novel microfluidic platform that is compatible with specially shaped optical fiber integrations. This thrust addresses Specific Objectives 3.

The scope of this dissertation is following the above thrusts, while focusing on two particular specially shaped optical fibers, namely, the tapered optical fiber and the D-shape optical fiber. These two types of fibers exemplified two most commonly used form factors for the specially shaped fibers, including the in-line form factor (tapered fibers) and the probe-like form factor (D-shape fiber). Tapered fibers, including straight tapered fibers and tapered fiber loops and helices, are ideal for in-line, embedded monitoring, while D-shape fibers with a fiber-tip form factor are ideal for applications that require quick and easy insertion and removal of the fiber.

The rest of this dissertation is organized in the following way. In Chapter 2, I will focus on straight fiber tapers, tapered fiber loops, and tapered fiber helices. I will start with the fabrication methods for two special shape tapered fibers, namely, the tapered fiber loop and the tapered fiber helix,

The rest of this dissertation is organized in the following way. In Chapter 2, fabrication methods for two specially shaped tapered fibers, namely, the tapered fiber loop and the tapered fiber helix are introduced, followed by an experimental characterization of their optical properties. The applications of the tapered fiber helix in integrated photonic device characterizations and

micro-particle manipulations are also studied. In chapter 3, a fiber tapering setup based on a customized ceramic microheater are developed. A detailed parametric study of the setup's performance is carried out. The setup's capability of fabricating high-quality tapered fibers in a highly repeatable way is experimentally demonstrated. A reliable monitoring method based on the optical mode theory is developed and experimentally demonstrated. In chapter 4, a tip-based lossy-mode-resonance D-shape fiber relative humidity and moisture content sensor is experimentally demonstrated. The lossy mode resonance (LMR) generated by the D-shape fiber is experimentally and numerically characterized. The LMR's dynamic response to a continuously changing relative humidity is experimentally characterized. The LMR sensor's capability of monitoring the moisture content change in food samples is experimentally demonstrated. In chapter 5, a reconfigurable acrylic-tape microfluidic platform is introduced. The laser-ablation-based fabrication method of the acrylic microfluidic channel is experimentally studied. Various functions enabled by the reconfigurable functional sealing tapes are experimentally studied. An initial experimental demonstration of the integration of D-shape optical fibers with the acrylic-tape microfluidic device is presented.

Chapter 2 TAPERED OPTICAL FIBER LOOPS AND HELICES FOR INTEGRATED PHOTONIC DEVICE CHARACTERIZATIONS AND MICROPARTICLE MANIPULATIONS

In this chapter, we demonstrated two special geometries of tapered optical fibers, namely the tapered fiber loops and helices. The tapered fiber loops demonstrated in this chapter are distinct from previous ones in terms of their superior mechanical stability and high optical quality factors in air, thanks to a post-annealing process. We experimentally measured an intrinsic optical quality factor of 32,500 and a finesse of 137 with a tapered fiber loop. The tapered fiber helix demonstrated in this chapter is a novel geometry that has never been demonstrated in other works using tapered fibers. The tapered fiber helices' applications in integrated photonics and microfluidics are presented.

The rest of this chapter is organized as the following. In section 2.1, applications and fabrication methods of the existing special-shape tapered fibers are briefly reviewed. In section 2.2, the development of the fabrication setups for the tapered fiber loops and tapered fiber helices based on an alcohol-lamp-based fiber tapering setup are presented. In section 2.3, the tapered fiber loop's and helices' optical spectroscopies and the tapered fiber loop's mechanical stability are optically characterized. In section 2.4, experimental demonstration of the tapered fiber helices' capability in integrated photonic device characterizations is presented. In section 2.5, the tapered fiber's capability of microparticle manipulation in fluidic environment is experimentally demonstrated.

2.1 A BRIEF REVIEW OF THE EXISTING SPECIAL-SHAPE TAPERED FIBERS

2.1.1 Existing special-shape tapered fibers and their applications

In recent years, tapered optical fibers [8,14,23,26,29,31,90,91], through which guided light can interact with the environment, have found a wide range of applications, including nanophotonics [10,28,92], microfluidics [93,94] and micro/nanoscale sensing [54,95]. In these applications, free-space optical beams are limited in the spatial resolution due to the diffraction

limit. In addition, they suffer from the limited focal depth of objective lenses and from diffraction, especially for object features that are comparable with or smaller than the light wavelength. On-chip optical waveguides [96] provided a solution to these challenges, but they impose additional steps or difficulties on the fabrication process, and their positions cannot be adjusted after fabrication. Tapered optical fibers, however, with diameters in micrometers or sub-micrometers, can deliver guided light into and out of tightly spaced micro/nanoscale systems with readily adjustable positions and high spatial resolution.

Various geometries of tapered optical fibers have been developed and investigated. The most studied geometries include straight tapered fibers [2,34,93,97,98], dimpled tapered fibers [9,10], tapered fiber knots [12,23,24,90,99], tapered fiber coils [14,91] and tapered fiber loops [27,28,31]. Each of these geometries has its own unique advantages and hence has found various applications. For example, tapered optical fibers with circular geometries, such as loops, coils and knots are stand-alone optical ring resonators. Their high optical quality factors (Q factor up to 97260 [23]) allow them to find applications in sensing [3,12,25] and fiber-based lasers [26,100,101]. Optical trapping and sorting of particles have been mainly demonstrated with straight tapered optical fibers [94,102]. Tapered optical fibers have been particularly useful for nanophotonic device characterization. It is challenging for a straight tapered fiber to couple light to a monolithic in-plane device (see section 2.4.2). The surrounding area of the device has to be etched down [97], which makes the fabrication process more complex. Dimpled fibers [9,10], which have a depression part in the tapered region, and fiber loops [28] have been used to characterize tightly spaced in-plane devices.

2.1.2 Fabrication methods of the existing special-shape tapered fibers

Difficulties of the fabrication of different special-shape tapered fibers are different. Straight tapered fibers are generally fabricated with the heat-and-pull method [97], which is straight forward. The fabrication process of tapered fiber knots is relatively complex and requires delicate handling of the tapered optical fiber. In most of the demonstrated tapered fiber knots [12,25,26,99], one tapered fiber arm was broken during the fabrication process and reconnected to a separate straight tapered fiber after the knot was formed, resulting in poor mechanical stability. One recent work [23] demonstrated a tapered fiber knot fabrication method without breaking the tapered fiber. Tapered optical fiber coils were fabricated by wrapping a straight tapered optical fiber around a

cylindrical rod, which limits their spatial flexibility and agility [14,21]. Dimpled tapered fibers were fabricated by wrapping the waist section of a tapered fiber around a mold while heating the taper, and the process could be time-consuming and lacks controllability and repeatability. Tapered fiber loops have been fabricated by introducing internal torsional stress [28,31] or by bending [90] the straight tapers into a loop shape. Due to the residual torsional or bending stress in the loops, the two fiber arms may intersect with each other with an angle, resulting in low optical Q factors [8]. In most work, the shapes of the tapered fiber loops were not permanently fixed, but rather temporarily maintained by either the torsional stress or van der Waals and electrostatic forces, causing the loops mechanically unstable [23,28]. In order to make the loops stable and to achieve a high optical Q, the size of the loop was kept large (a few hundred μm to a few mm) [31], and sometimes the loop was fixed by glue [103] or by being embedded in a gel matrix [30].

2.2 DEVELOPMENT OF FABRICATION SETUPS FOR THE TAPERED FIBER LOOPS AND HELICES

2.2.1 Fiber tapering system based on an alcohol lamp

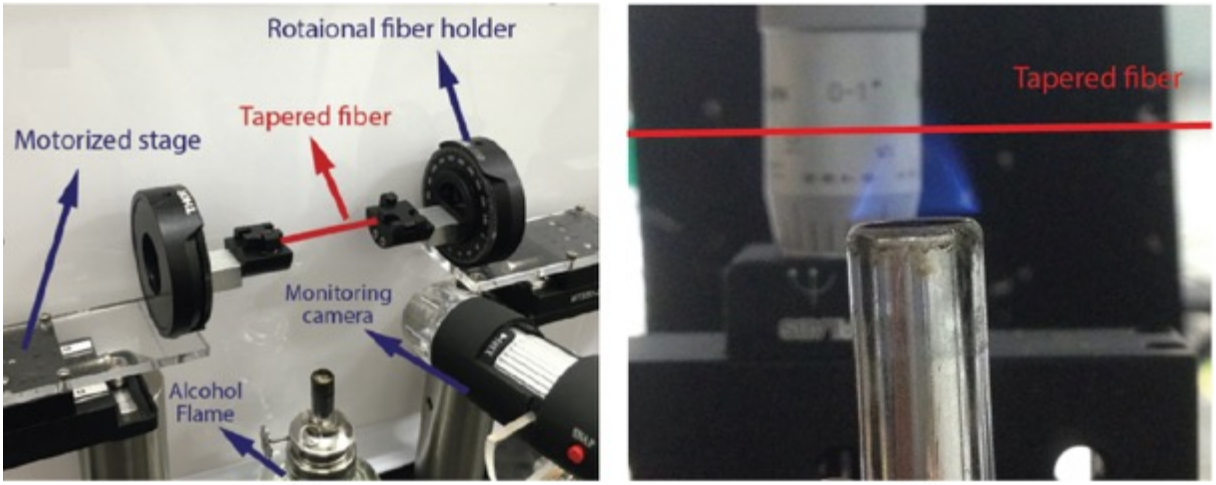

Figure 28 (a) The fiber tapering setup. (b) A microscope photo showing the optimum relative position between the flame and the fiber.

Tapered fibers used in this chapter are all fabricated from regular Corning SMF-28 fibers using the heat-and-pull method [9]. The fiber tapering setup is shown in Figure 28 (a). The fiber being

tapered was held between two fiber clamps (SM1F1-250, Thorlabs) which were connected to two rotational holders (RSP1, Thorlabs). The rotational holders are not used in the fiber tapering process but will be used in the fabrication of tapered fiber loops and helices (detailed in section 2.2.2). The two rotational stages were mounted onto two customized acrylic boards which sat on two motorized translational stages (MTS25-Z8, Thorlabs). A microscope camera (Jiusion-1000x) was used to monitor the tapering process. A commercially available alcohol lamp (LMP-422, from EURO TOOL) was used as the heat source for the fiber tapering. During the tapering, the alcohol lamp was put on a 3-D stage, so that the relative position between the flame of the lamp and the tapered fiber can be adjusted. The optimum position of the flame is when the tapered fiber sits within the tip of the flame as shown in Figure 28 (b). This is because this part of the flame has a more uniform temperature distribution and generates minimum soot.

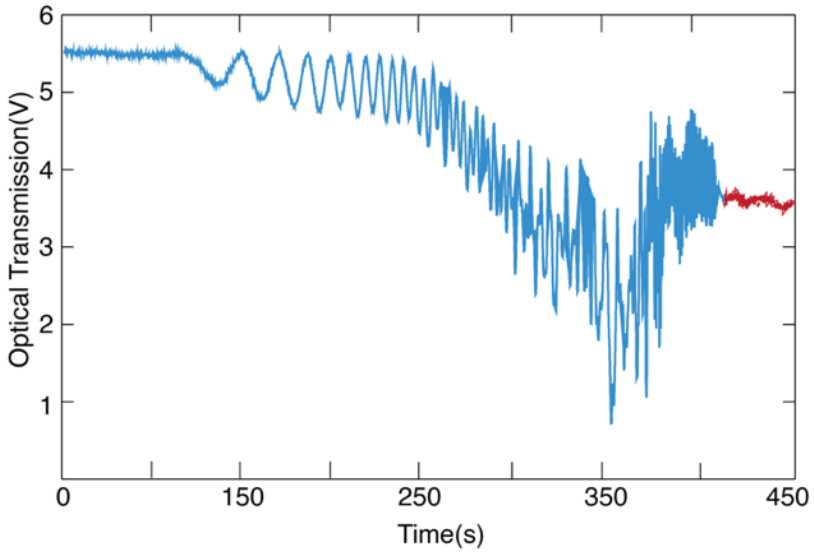

Figure 29 Optical transmission of straight tapered fiber tapering during the fabrication process. The heat-and-stretch process started at 0 second and stopped at 450 second. The transition from the oscillating part (blue) to the stable part (red) indicated the trigger to stop the tapering process.

During the tapering, both motorized stages move at a speed of 0.05mm/s. The tapering process was monitored using the real-time optical transmission from the tapered fiber. A typical transmission curve is shown in Figure 29. The tapering process was stopped when the optical transmission became stable (red part of the curve in Figure 29), which indicated that the tapered fiber's radius fell below the cut-off of higher order modes, and the tapered fiber has become single mode [9]. As a result, all the tapered fibers in this work had similar diameters. According to the

SEM images, the diameters of fiber tapers range from 600 nm to 2 μm. The typical tapering length of the tapered fiber is between 35 to 40 mm, and the typical optical transmission is between 70~85% (a fiber tapering setup that can produce higher transmission tapered fibers will be discussed in Chapter 3).

2.2.2 Fabrication methods for the tapered fiber loops and helices

After the straight tapered fiber was fabricated, we relaxed the tension in the straight fiber taper by moving the two fiber arms closer by 1 mm to avoid breaking the fiber in the following steps. The two rotational fiber holders were rotated in the opposite directions by 360° to introduce torsion to the straight tapered fiber, as shown in Figure 30 (a). We further moved the two fiber arms closer until the loop was formed in the center of the tapered region, as shown in Figure 30 (d). At this point, the diameter of the loop was around 300 μm to 500 μm. We shrunk the loop size by moving the two fiber arms apart. The final loop diameter could be continuously adjusted by the stage positions, and loop diameters as small as 15 μm have been experimentally demonstrated.

Similar with most of the previous work [28,31,90], fiber loops at this stage had poor optical quality factors and were mechanically unstable. Even a small air current could cause considerable change of the geometry and the optical transmission. Different from the previous work, we used a flame to anneal the loop for a few seconds. The diameter of the flame (a few mm) was much larger than the loop diameter (< 100 μm), so the whole loop was heated and annealed without moving the flame. This post-annealing released the torsional stress in the fiber loop and hence "fixed" the loop shape, as shown in Figure 30 (b) and (e). Fiber loops after the post-annealing were mechanically stable. The annealed fiber loops could not be unwrapped by the air flow. In fact, for all the tapered fiber loops we fabricated and tested, the loops' geometry was reserved even when they were broken by a strong air flow. The loop's mechanical stability will also be optically characterized in section 2.3.2.

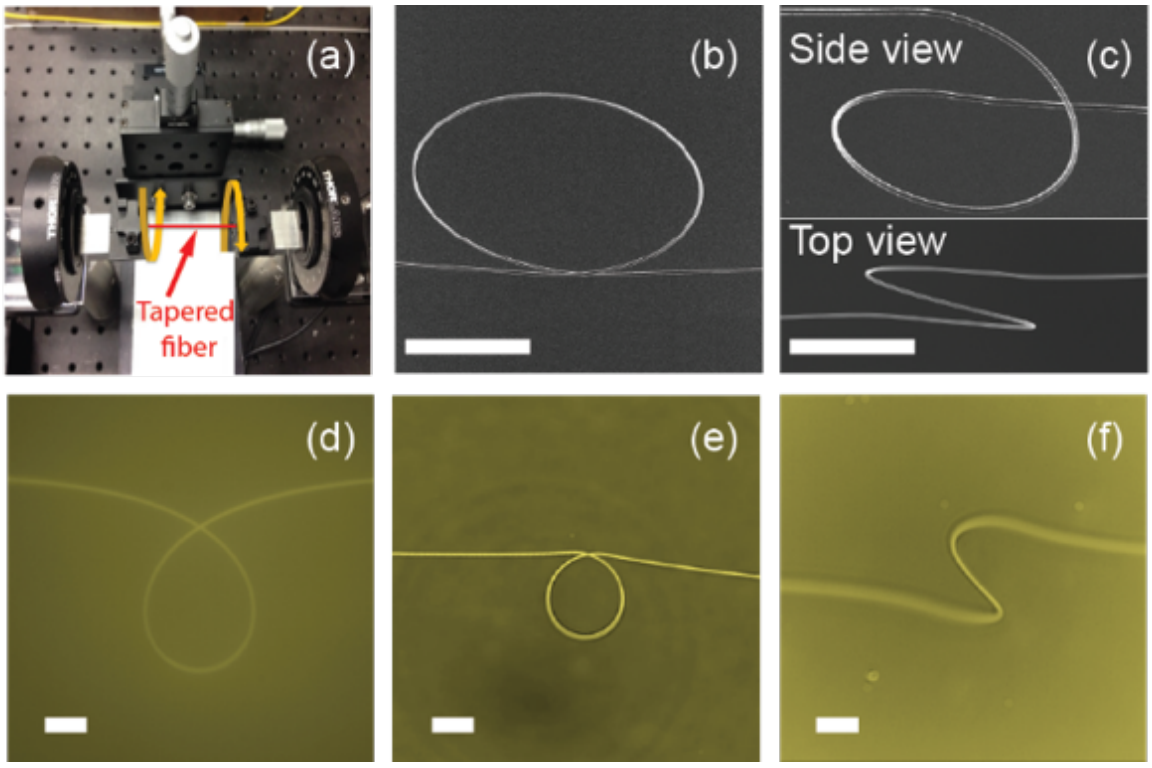

Figure 30 (a) The fabrication setup for the tapered fiber loops and helices. The rotational fiber holders are on both sides of the fiber. SEM images (b, c) and optical microscope images (d-f) of fabricated tapered optical fibers. (d) A tapered fiber loop before annealing. (b, e) A tapered fiber loop after annealing. (c, f) A tapered fiber helix. Scar bars: 15 μm.

When we applied additional tension to an annealed tapered fiber loop by moving the fiber arms apart, the tapered fiber loop was stretched into helical shapes, with the two fiber arms separated from each other, as shown in Figure 30 (c) and (f). Fiber helices were even more stable than loops, thanks to the additional tension. Because the loop geometry was fixed in the annealing process, the geometry of the fiber probe can be readily switched between a helix and a loop by controlling the tension. The fabrication processes of the loops and helices are highly repeatable, a successful rate of more than 90% has been experimentally demonstrated.

After the tapered fiber loops/helices was fabricated, we turned the two fiber arms to a U-shape (as shown in Figure 31 (a-b)) and mounted the fiber loop on a homemade fiber holder (as shown in Figure 31 (c)), which could adjust the tension along the fiber and hence could switch the geometry between a loop and helix. This way of holding a fiber helix allowed it to serve as a probe that could easily reach out to devices for light coupling, similar with previous work of fiber dimples.

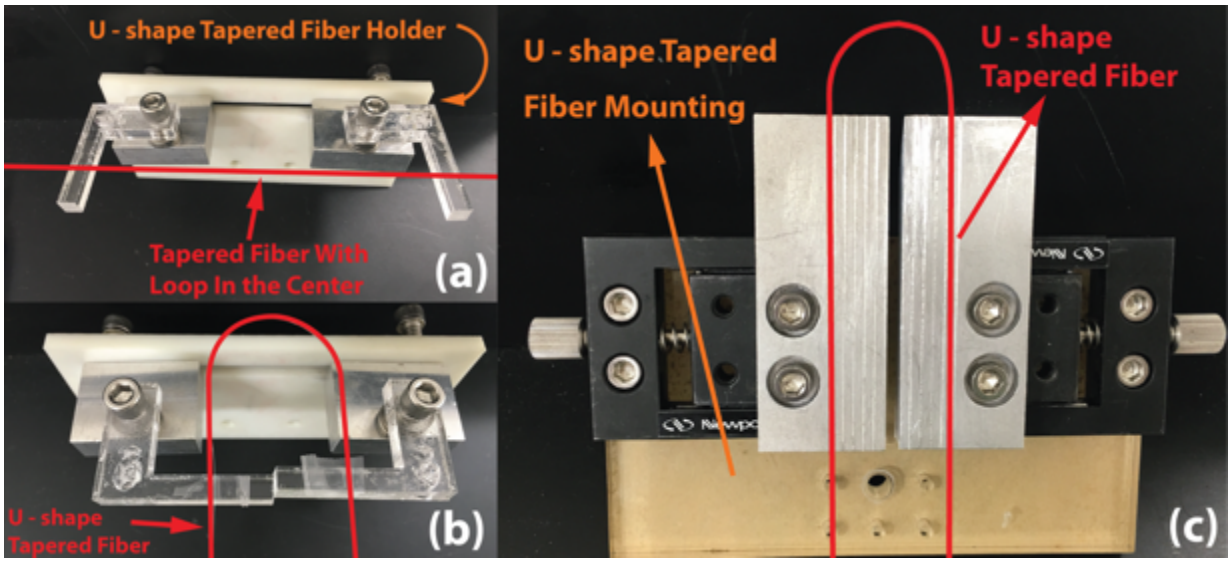

Figure 31 . (a), (b) show a tapered fiber loop with straight arms being turned into U-shape by the transfer fiber holder. (c) shows the U-shape tapered fiber on the mounting. The two fiber arms are taped onto two translational stage separately, so the U-shape tapered fiber can be stretched and relaxed by moving the translational stage. In (a), (b), and (c) the tapered optical fiber is marked by red lines for better visualization.

2.3 OPTICAL CHARACTERIZATIONS OF THE TAPERED FIBER LOOPS AND HELICES

2.3.1 Optical spectroscopies of the tapered fiber loops and helices

Swept-wavelength spectroscopies were used to characterize the optical properties of the tapered optical fiber loops and helices. Light from a tunable laser source (Newport, New Focus 6700) was coupled into one end of the fiber, and the optical transmission was measured from the other end by a photodetector (Thorlabs, PDA50B). The transmission spectra of a loop before annealing, one after annealing, and a fiber helix are shown in Figure 32 (a), (b), and (c), respectively.

Multiple optical modes were observed in the annealed tapered fiber loop (Figure 32 (b)), with an intrinsic optical quality factor Q = 32,500 and a finesse of 137. The post-annealing created a smooth transition region at the intersection of the two fiber arms (Figure 30 (e)), which reduced the scattering loss and resulted in a high Q. Compared to on-chip silicon resonators [23, 33], which can provide higher Q and finesse, the tapered optical fiber loops are standalone optical resonators that do not require separated devices for optical input and output. No optical resonance was observed in the fiber loops without annealing (Figure 32(a)) and fiber helices (Figure 32(c)). The

two arms of a tapered fiber loop without annealing intersected with each other at a sharp angle (Figure 30 (d)), resulting in a high scattering loss and hence no observation of optical modes.

Thanks to the evanescent field of the guided light that extends outside the tapered fibers, both the tapered fiber loops and helices can allow the guided light to interact with the environment. They are useful tools for delivering the light into and to interact with micro/nanoscale systems, with each having its unique advantages. The high optical Q-factor enables a high optical energy built up in the annealed tapered fiber loops, which helps increase the sensitivity in near-field sensing applications [12]. The resonances in the tapered fiber loops can also potentially be used for fiber-based laser applications [26,101]. By contrast, the tapered fiber helices have high optical transmission, high mechanical stability, and no optical resonances, which made it an ideal probe to characterize the optical and mechanical performances of integrated photonic devices. In the section 2.4 and 2.5, we will focus on the experimental demonstration of two particular applications of the fiber helices, namely, the in-plane integrated photonic device characterization and the micro-particle manipulation.

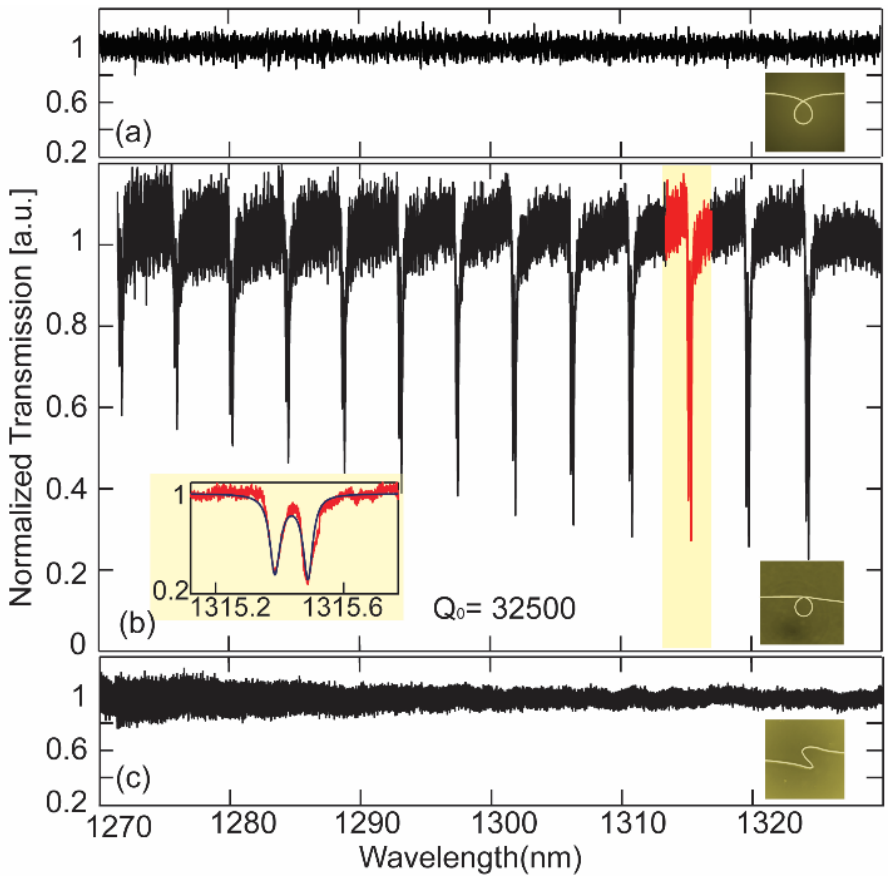

Figure 32 Transmission spectra of (a) a tapered fiber loop before annealing, (b) a tapered fiber loop after annealing, and (c) a tapered fiber helix. No resonance was observed in the tapered fiber helix and the tapered fiber loop without annealing. Multiple optical modes were observed in the annealed tapered fiber loop. Left inset in (b) shows the zoomed-in transmission spectrum of the optical resonances. The two resonances correspond to two optical modes with the same mode number and different polarization states. An intrinsic optical quality factor of 32,500 is obtained from the curve fitting (blue solid line in the left inset in (b)). Insets on the right in (a-c) are the optical microscopy images of corresponding tapered optical fibers.

2.3.2 Mechanical stability of the annealed tapered fiber loops

One of the major differences between our tapered fiber loops and the previous work is the additional annealing process, and hence the mechanical stability of the loops. To quantify the mechanical stability of the annealed tapered fiber loops, we measured the transmission spectra of an annealed loop over time, when the loop was exposed to air for two days. The measured spectra at 5 hours, 20 hours, and 48 hours after the loop was fabricated are shown in Figure 33. The free spectral range (FSR) of the measured spectra shifted by around 0.95% from 5 hours to 20 hours, and around 1% from 5 hours to 48 hours. Accordingly, the loop diameter was changed by around

1% from 5 hours to 48 hours, assuming the refractive index of the medium remained the same. It is noted that the loop was exposed in an air-conditioned room without precise control of the humidity. It can be seen that all the optical resonances were shifted to longer wavelengths over time. This red shift of the optical resonances (up to 0.4 nm from 5 hours to 48 hours) indicates moisture accumulated on the fiber loop surface. This water layer might have contributed to the shift of the FSR, so the fiber loop diameter change could be smaller than 1%.

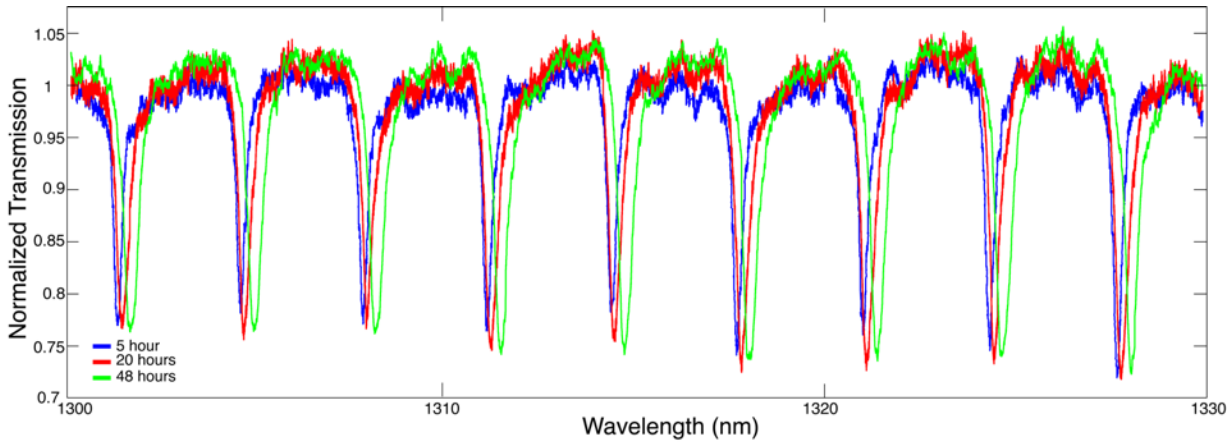

Figure 33 Measured transmission spectra of the tapered fiber loop in air at 5 hours, 20 hours, and 48 hours after the loop was annealed.

2.4 EXPERIMENTAL DEMONSTRATION OF INTEGRATED PHOTONIC DEVICE CHARACTERIZATION USING THE TAPERED FIBER HELICES

2.4.1 Brief description of the integrated photonic device used in the experiment

The integrated photonic device used in this experiment is a Si_3N_4 tuning fork cavity optomechanical sensor. The device is fabricated by my lab mate Rui Zhang. A more detailed description of the device and its working principle can be found in his previous work [104]. Here, we give a brief description of this integrated photonic device to facilitate a better understanding of the experimental results discussed later. The integrated photonic device consists of a tuning fork nanomechanical resonator and a 15 μm diameter microdisk optical resonator. The device was fabricated on a 250-nm-thick stoichiometric Si_3N_4 film. The prongs of the tuning fork are 150 nm in width and 20 μm in length. The tuning fork and the microdisk are separated by a gap of 150 nm, enabling near-field optomechanical coupling. The mechanical displacement of the tuning fork

modulates the optical whispering gallery modes of the microdisk, which in turn will causes the fluctuation of the optical transmission in an optical fiber probe (in this case, the tapered fiber helix) near-field coupled to the microdisk.

2.4.2 Comparison of straight tapered fibers and tapered fiber helices for in-plane integrated photonic device characterization

It is challenging for a straight tapered fiber to couple light to an in-plane integrated photonic device without its two arms touching the surrounding substrate, as shown in Figure 34 (a). The straight tapered fiber can reach a device only when the surrounding substrate is etched down and other devices removed, as shown in Figure 34 (b). By comparison, the tapered fiber helix, which looks like a loop from the side view, can couple light into any device of interest in an array, as shown in Figure 34 (c). This makes the fiber helix a versatile optical probe that can be used to characterize tightly spaced in-plane integrated photonic devices on the fly.

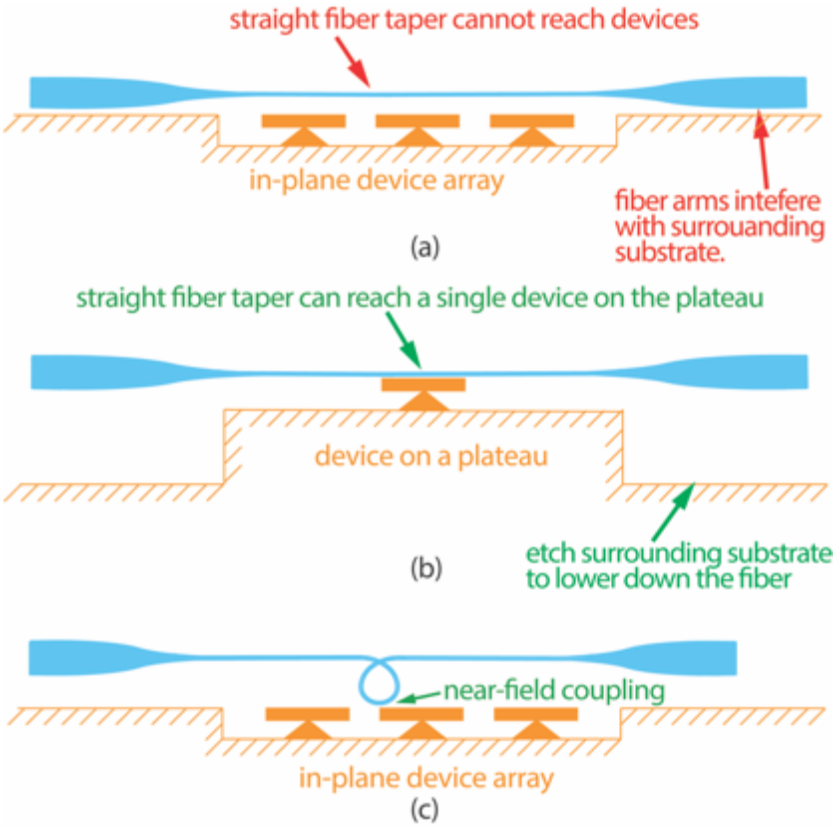

Figure 34 (a) The two arms of the straight tapered fiber interfere with the surrounding substrate and devices before the tapered fiber can reach the in-plane integrated photonic device. (b) After the surrounding substrate is etched down and other devices removed from below the fiber, the

straight fiber taper can reach a single device on a plateau. (c) The fiber helix can near-field couple light to any in-plane device in an array.

2.4.3 Experimental characterization results

In this section, we used the tapered fiber helix to experimentally characterize the integrated photonic device we introduced in section 2.4.1 (Si_3N_4 tuning fork cavity optomechanical sensor). The experiment was carried out in air. A laser was input from one arm of the fiber helix and coupled from the lowest position of the tapered fiber helix to the microdisk, and the optical transmission of the fiber helix was read out by a photodetector.

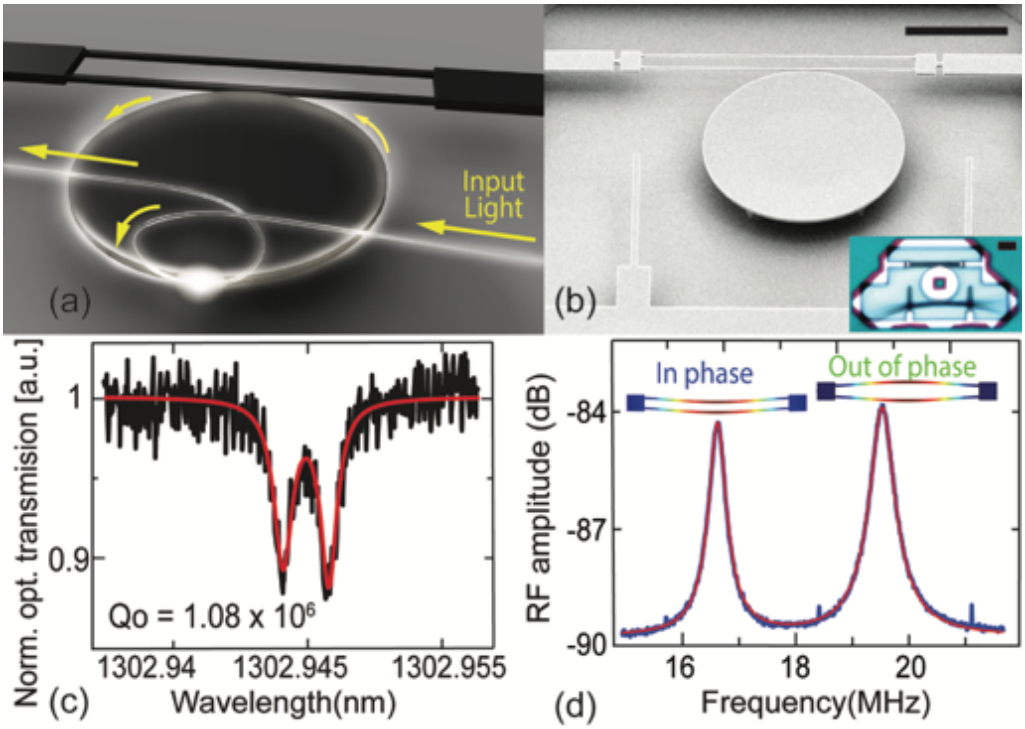

Figure 35 (a) A computer generated schematic showing the optical coupling between a tapered fiber helix and a microdisk resonator, the yellow arrows indicate the light propagation direction. (b) SEM image of the integrated photonic device (a tuning fork cavity optomechanical sensor). Inset shows an optical microscope image of the device being tested, and the fiber helix is near-field coupled to the microdisk resonator. The scale bars are 10 μm. (c) Transmission spectrum of the tuning fork device. A Q-factor of 1.08 x 10^6 was readily obtained with the fiber helix probe. (d) Mechanical spectrum of the same tuning fork device. The two mechanical modes correspond to in-phase and out-of-phase tuning fork modes, respectively. The device was tested in air, thanks to the mechanical stability of the fiber helix.

The optical spectrum of the tuning fork device was shown in Figure 35 (c). A Q above a million was readily obtained. The output of the photodetector was sent to an electronic spectrum analyzer (ESA), and the mechanical spectrum of the thermal motion of the tuning fork was obtained and

shown in Figure 35 (d). Both the in-phase and out-of-phase mechanical modes were clearly observed, well above the noise ground. The mechanical quality factors in this work were lower than previously published results [104] due to higher damping in air compared with that in vacuum. The tapered fiber helix is mechanically stable thanks to the additional tension, which allows precise control of the separation between the tapered fiber helix and the microdisk, bestowing on the helix the capability of characterizing nanophotonic devices in air. Furthermore, similar with fiber dimples [9,10], the helical shape allows near-field light coupling between the fiber and the in-plane device while preventing the two fiber arms from touching the substrate. This can be seen in Figure 35 (a), where the fiber helix curves away from the device plane on both sides. Compared to that of the tapered fiber dimples, the fabrication process of the fiber helix is straightforward, controllable, and repeatable.

2.5 EXPERIMENTAL DEMONSTRATION OF MICROPARTICLE MANIPULATIONS USING THE TAPERED FIBER HELICES

In addition to characterizing integrated photonic devices, the fiber helix is also a useful tool in microfluidics for radiation-pressure-based microparticle trapping and manipulation. To demonstrate this capability, we used the tapered fiber helix to optically trap and propel microscale silica beads in water. An illustration showing the microparticle manipulation using the tapered fiber helix is shown in Figure 36 (a). The evanescent field of the tapered fiber helix applies two components of optical forces to the nearby beads: a gradient force that attracts beads towards the fiber, and a scattering force that propels the beads along the fiber. The fiber helix can thus be used as a helical-shaped optical conveyor belt for particle transportation. The experimental setup is shown in Figure 36 (b). The U-shape tapered fiber helix was mounted onto a three-dimensional translation stage and a one-dimensional rotational stage for position and orientation control. The fiber helix was inserted into a solution of 4.64-μm-diameter silica beads in a transparent petri dish. A 500-mW continuous-wave laser at wavelength of 1330 nm was used as light source. The microparticle manipulation experiment was monitored and recorded on an inverted microscope platform.

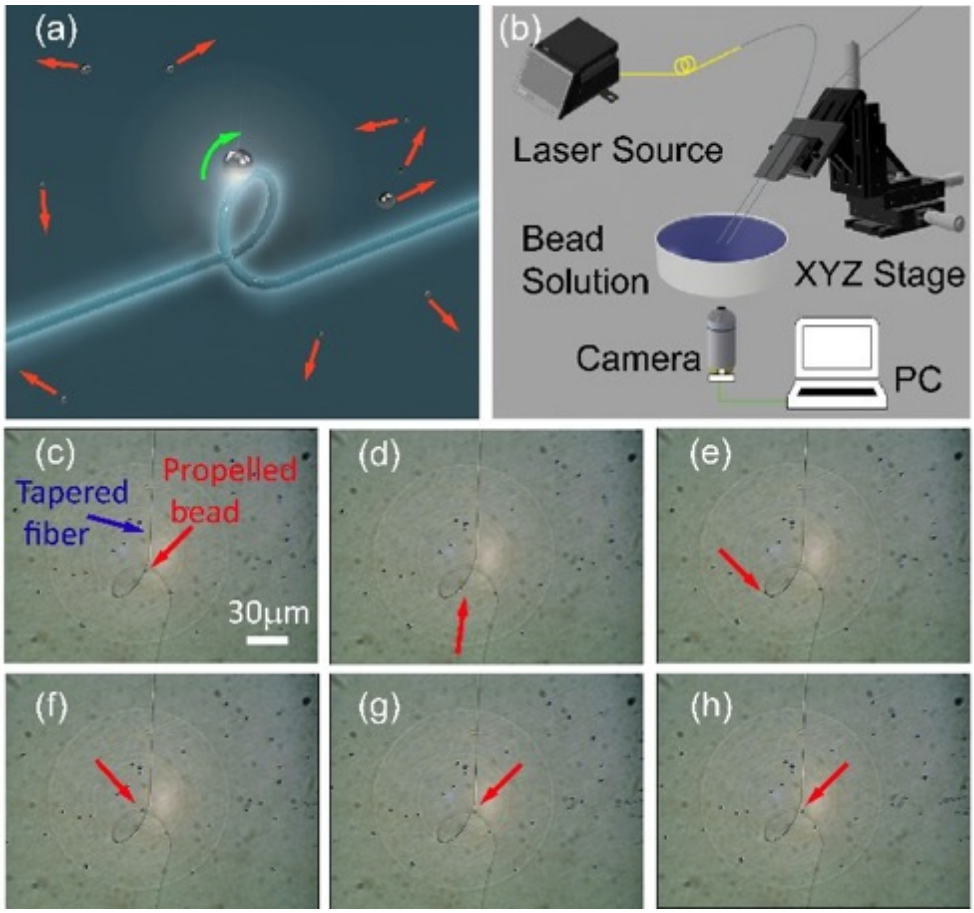

Figure 36 (a) A computer generated schematic showing a silica bead trapped and moved (green arrow) by a tapered fiber helix. The red arrows show the un-trapped beads moving in random directions because of the Browning motions. (b) Schematic of the microfluidic trapping setup. (c-h) Successive pictures showing the trapping results. The light guided in the tapered fiber helix propagated from top to bottom. The red arrows indicate the position of the bead being trapped and propelled. The time interval between each adjacent frame is 3 seconds.

The optical trapping experimental results are shown in Figure 36 (c-h). A single silica bead with a diameter of 4.64 μm was trapped and subsequently propelled along the tapered fiber helix. We note that the particle trapping in water can be influenced by the transmission of the tapered fiber helix. The optical transmission of the tapered fiber helix in water was around 20%. The transmission was considerably lower than that in air, which could cause the trapping to be unstable. This reduced transmission in water might be caused by bending induced optical loss [8] in the helix. Other possible reasons include, the tapered optical fiber geometry is only adiabatic in air but not in water and optical absorption loss caused by the water. Work is underway to optimize the

fiber tapering process in order to increase the transmission efficiency of tapered optical fiber helix in water.

Compared with straight fiber tapers [93,94], the geometry of the tapered fiber helices allowed optical transportation of microscale particles along more complex, three-dimensional trajectories. In a stationary fluidic environment, the fiber helix can be used to selectively approach, trap, and propel a particular particle lying on the substrate from a group of particles, which is challenging for straight tapered optical fibers. In a microfluidic channel, the fiber helix can be used to pre-focus particles to the center of the channel, as they pass through the channel. The three-dimensional shape of the tapered fiber helix allows for much more efficient particle focusing than straight fiber tapers. This pre-focusing is important for effective subsequent optical detection or interrogation, such as flow cytometry [105] and cell stiffness measurements in optical stretchers [106].

2.6 SUMMARY

In this chapter, we have demonstrated tapered optical fiber loops and helices with a straightforward and repeatable fabrication method. Due to a post-annealing process, tapered fiber loops and helices exhibited high mechanical stability. The highest measured optical quality factor (Q-factor) of tapered fiber loops was around 32,500. In addition, the fiber geometry can be readily switched between a loop and a helix by adjusting the mechanical tension. A tapered fiber helix was used to characterize both optical and mechanical resonances of a monolithic in-plane integrated photonic device. In addition, we also used a tapered fiber helix to optically trap and propel microscale silica beads in fluidic environment. Thanks to their repeatable fabrication process, outstanding mechanical stability, and the ability of near-field probing in-plane devices, tapered fiber loops and helices can find wide applications including integrated photonic device characterizations, microparticle manipulations, and optical sensing.

Chapter 3 HIGHLY ACCESSIBLE AND LOW-LOSS FIBER TAPERING SETUP BASED ON A CERAMIC HOUSED ELECTRIC FURNACE (CHEF)

In the previous chapter, a fiber tapering setup based on an alcohol lamp was used to fabricate all the tapered fibers used in the experiment. The setup was used between the year 2014 to 2016. During the time, we found that the alcohol-lamp-based fiber tapering setup has many limitations which are detailed in the following. 1) The fiber being tapered may break during the tapering process. Around 3 to 4 fibers may break in ten fiber tapering experiments. 2) For the tapered that was not broke, they do not have a high optical transmission. The typical optical transmissions of the fabricated tapered fibers are between 70% to 85%. The highest optical transmission achieved is around 90%. These limitations are mainly caused by the alcohol lamp heat source. 1) and 2) are caused by the instability of the alcohol-lamp flame. The alcohol lamp flame may fluctuate both due to environmental air current disturbance and instable alcohol supply from the wick. For 3), it is because the flame sizes required for the fiber tapering and the loop annealing processes are different, and the flame size of the alcohol lamp has a low controllability (controlled by manually adjusting the wick). Furthermore, after 2 to 3 months usage, the wick of the alcohol lamp might degrade, and start to generate soot in the flame. The soot will contaminate the tapered fibers and cause them to fail.

In order to increase the transmission of the tapered fiber, and to improve the controllability and repeatability of the fabrication process of the tapered fibers, between 2017 and 2018, we developed a new heat source called the ceramic housed electric furnace (CHEF) and a CHEF-based fiber tapering system. This CHEF-based fiber tapering system can fabricate high-performance tapered fibers with a much higher repeatability compared to the flame-based fiber tapering setup used in Chapter 2. While the performance of the CHEFs fabricated at different times may fluctuate due to the manual fabrication process, a fabricated high-performance CHEF can maintain its performance for as long as 6 months. I have experimentally demonstrated that using a high-performance CHEF, the successful rate of fabricating a tapered fiber with transmissions higher than 95% is more than 90%.

The rest of this chapter is organized as the following. In section 3.1, a brief review of the current heat sources used in the heat-and-pull fiber tapering setup is presented. In section 3.2, the development of the CHEF-based fiber tapering setup is presented. Recommendations to prevent failure of CHEF fabrication are given at the end. In section 3.3, an experimental parametric study of the CHEF is carried out, followed by a temperature characterization of the CHEF. In section 3.4, a theoretical fundamental understanding of the fiber tapering process is presented. In section 3.5, based on the fundamental understanding in section 3.4, the experimentally measured optical transmission from a tapered fiber is analyzed. In 3.6, based on the transmission analysis in section 3.5, we developed a new monitoring method for the fiber tapering. This method can reliably determine the optical modes that are propagating in the tapered fiber. In section 3.7, a close to perfect-adiabatic tapered fiber is experimentally demonstrated using the CHEF-based fiber tapering setup. Its tapering process is analyzed based on the fundamental understanding developed in section 3.4, 3.5 and 3.6.

3.1 Review of current heat sources used in the heat-and-pull fiber tapering setup

As we have mentioned in the Chapter 2, tapered optical fibers have found a wide range of applications, including chemical and biological sensing [54,107], micro-particle [34, 88] and atom trapping [18], and low-loss light delivery [9,108]. Particularly, tapered fibers are widely used as an optical probe for on-the-fly device characterizations in monolithic integrated photonics [9]. Since the audience of integrated photonics is quickly expanding, it becomes increasingly important that tapered fibers with high performance can be fabricated in a readily accessible and repeatable way.

Currently, most of the tapered optical fibers are fabricated using a heat-and-pull method [36]. Specifically, a section of the fiber is heated and softened by a heat source while being pulled and thinned by two motorized stages. While little needs to be done on motorized stages to improve the fabrication method, the currently used heat sources are far from ideal. A desired heat source should satisfy the following two requirements. Firstly, it should enable a highly repeatable fabrication process and produce tapered fibers with high optical transmission. This requires the heat source to maintain a stable and controllable temperature for the tapering. Secondly, the heat

source should be readily accessible, which means it should be low-cost, easy-to-use, and can be easily fabricated. Additionally, it is beneficial if the heat source allows the fabrication of tapered fibers with various tapering lengths to adapt for different applications. For example, in tapered-fiber-based Brillouin scattering [35], a tapered fiber with a relatively long tapering length (~80 mm) is used for enhanced optomechanical interactions. By comparison, for the integrated photonic device characterization [9], a relatively short tapered fiber length (~30 to 40 mm) is preferred for its high maneuverability and mechanical stability.

Several types of heat sources have been reported, including flames [9], CO_2 lasers [9], and commercially available micro-heaters [27]. Flame based heat sources are susceptible to environmental fluctuations including air currents, which can result in a poor repeatability of fiber tapering. Furthermore, flames produced by low-cost sources, such as an alcohol lamp [27], may contain soot that can contaminate the tapered fiber and cause high transmission loss. Compared with the flame, the CO_2 lasers can provide a stable, soot-free heating zone that will not be influenced by air currents. However, CO_2-laser-based heat sources need to be carefully aligned using a relatively complex free-space beam steering setup. This setup needs constant re-alignments by a trained user, which limits the accessibility of the setup and the repeatability of the tapering results. Compared with the flame and the CO_2-laser-based heat sources, commercially available micro-heaters [27] can provide a heating zone that is stable and free from contamination and has a straightforward and compact design that do not require special alignment in the system setup. However, the commercially available micro-heaters used in published works are relatively expensive (ranging from $2500 to $20,000 each), and any replacement or repair of such systems could result in additional costs and a long lead time.

It is clear that the key to make the high-performance tapered fibers that have high transmissions and suitable tapering lengths more accessible is the heat source. The desired heat source that is low-cost, easy-to-use, and can generate repeatable tapering results without being influenced by the environment is yet to be demonstrated.

3.2 DEVELOPMENT OF THE CHEF-BASED FIBER TAPERING SETUP

3.2.1 Fiber tapering setup based on the CHEF heat source

The CHEF-based fiber tapering system is developed based on the alcohol-lamp-based fiber tapering setup introduced in section 2.2.1. The schematic and photo of the CHEF-based fiber tapering system are shown in Figure 37 (a) and (c). There are mainly two differences between the CHEF-based and the alcohol-lamp-based fiber tapering setup. As their name suggested, the first difference is that the two setups are using different heat sources (CHEF and alcohol lamp). The second difference is that the alcohol-lamp-based fiber tapering setup monitors the fiber tapering process based on the time-domain optical transmission signal, while the CHEF-based fiber tapering setup monitors the fiber tapering process based on the frequency-domain optical transmission signal. The frequency-domain-based monitoring method can more reliably determine the triggering of the single mode state of the tapered fiber (detailed in section 3.5), which is a feature desired by many applications. The heating mechanism of the CHEF is based on the electric resistant heating. During the tapering, a DC power supply (GENH150-5, TDK-Lambda) is used to input electrical driving current into the electric heating wire (A1 Resistance Wire, KANTHAL) coiled within a ceramic tube housing, as shown in Figure 37 (b) and (d). The heat generated by the electric heating wire is partially insulated by the ceramic tube and can raise the temperature within the tube to be higher than the transition temperature of the glass fiber. This temperature will soften the optical fiber within the tube and allow it to be tapered using the heat-and-pull method [9].

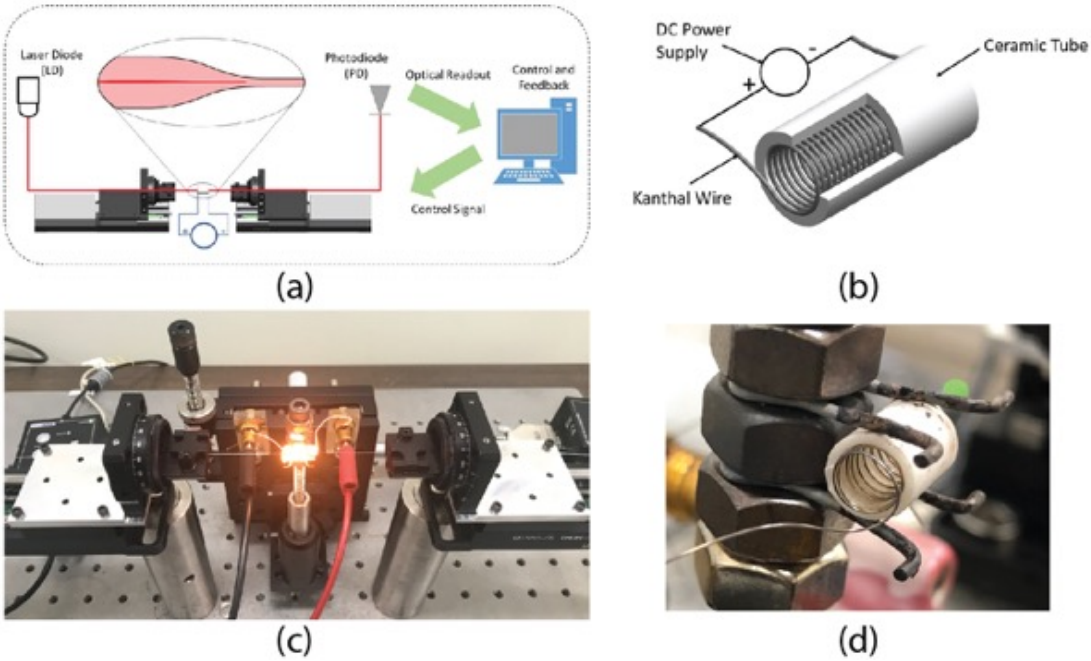

Figure 37 (a) and (c) show the schematic and photo of the fiber tapering setup respectively. (b) and (d) show the schematic and photo of the CHEF heat source respectively.

3.2.2 Fabrication of the CHEF

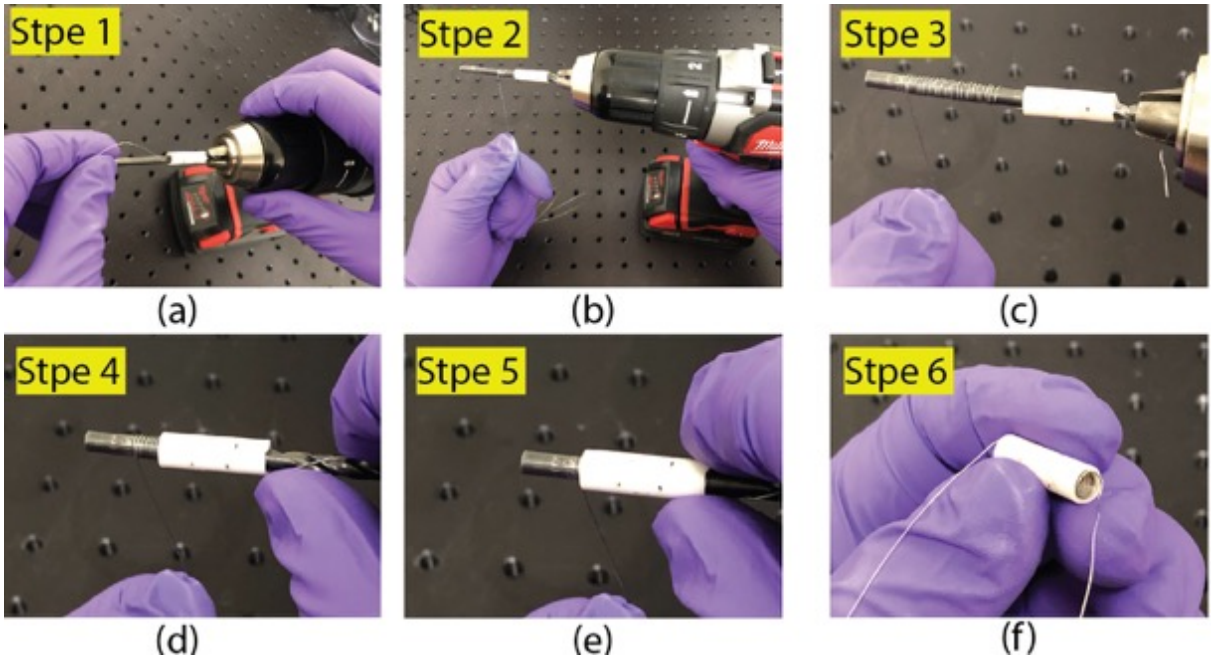

Figure 38 Photos showing the fabrication process of the CHEF. (a)-(c) show how the heating coil is winded using a hand drill. (d)-(e) show how the coiled heating wire is inserted into ceramic housing. (f) shows the fabricated CHEF.

As we have shown in Figure 37 (b) and (d), a CHEF is made of two components, the coiled heating wire and the ceramic tube housing. To fabricate the CHEF, we first slipped a ceramic tube onto a drill bit with diameter around 2.5 cm. Then a KANTHAL heating wire was threaded through the ceramic tube, and one end of the wire was clamped together with the drill bit into the drill head of a hand drill (M18, Milwaukee), as shown in Figure 38 (a). Then the KANTHAL wire was winded onto the drill bit by stretching one end of the wire with hand and rotating the drill bit using the drill, as shown in Figure 38 (b)-(c). After the desired coil length was achieved, the ceramic tube was pushed towards the coil by a finger until the coil was completely covered by the tube, as shown in Figure 38 (d)-(e). Finally, after releasing the clamped end of the heating coil, one can slide the coil together with the ceramic tube off the drill bit, and a CHEF was fabricated. The fabrication process of the CHEF is straightforward and highly repeatable. After several practices, a non-technical person can finish the process within 10 minutes.

3.2.3 Recommendations for the CHEF fabrication process

While the fabrication process of the CHEF is straightforward, there are some human-errors that could cause failure of the CHEF fabrication. A successfully fabricated CHEF has a uniformly spaced coil, while a failed CHEF has a nonuniformly spaced coil, as shown in Figure 39.

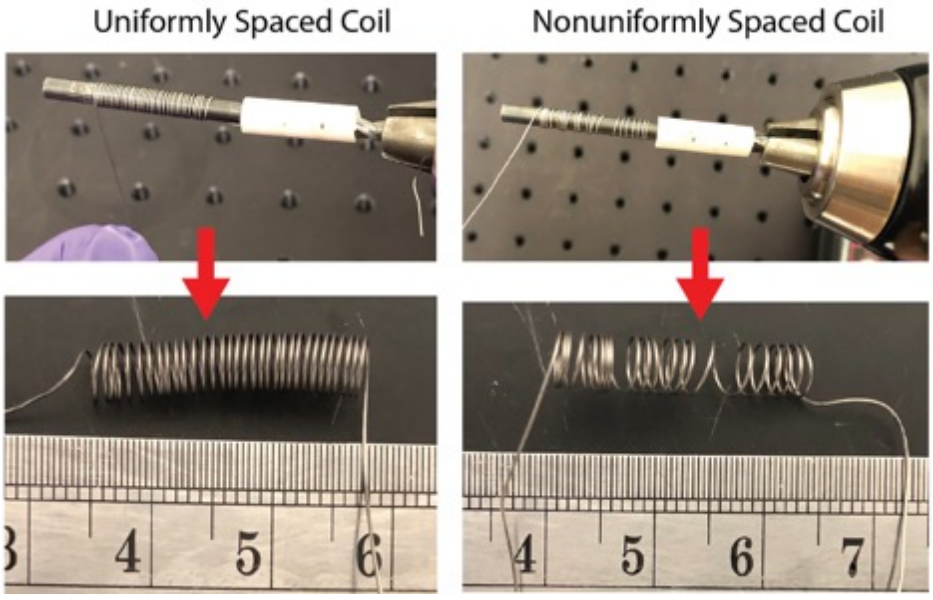

Figure 39 Photos showing uniformly spaced coil of a successfully fabricated CHEF (left column) and nonuniformly spaced coil of a failed CHEF.

To ensure the fabricated CHEF has a uniformly spaced coil we gave the following recommendations:

i. During the winding process, the hand that is holding the free end of the wire should move slowly at a constant speed comparable to the coil length's increasing speed. This can prevent the next coming wire stack onto the previous coiled wire.
ii. The angle between the free end of the coil wire and the drill bit should be kept the same throughout the winding process. This can ensure the distance between each wire is the same.
iii. During the winding process, keep a relatively slow rotation rate of the drill bit. A recommended ration rate is around 2-3 seconds per round. A slow rotation speed can will allow the user to achieve (i) and (ii) easier.
iv. Do not use a wire that is too hard or too soft for the fabrication. If the wire is too soft, when the fabricated coil is released from the drill bit, part of it will expand and deform, which may cause nonuniform coil spacings. If the wire is too hard, it will be difficult to control (i) and (ii) during the winding process. Recommendations related with how to choose the right wire thickness is further discussed in section 3.3.1.

3.3 EXPERIMENTAL STUDY AND CHARACTERIZATION OF THE CHEF

3.3.1 Parametric study and general design guidelines of the CHEF

We conducted a parametric study to fully understand how different CHEF designs and operation parameters affect the performance of the tapered fibers, as well as to elaborate a general design guideline for the CHEF. In the study, we fabricated CHEFs of different designs and experimentally characterized their fiber tapering results under different operation parameters. The results of the parametric study are presented in Table I. The table can serve as a useful guide for the users to fabricate high-performance tapered fibers using the CHEF.

In the table, the second and the third columns show different designs of the CHEF. Two design parameters were investigated in the parametric study, namely, the ceramic tube housing length (column 2) and the heating wire diameter (column 3). Specifically, for each parameter we selected three values, and in total nine designs with different combinations of ceramic housing lengths and heating wire diameters were studied. The fourth column of the table show the operation

TABLE I
Parametric Study of the CHEF

	Ceramic Housing Length (mm)	Heating Wire Diameter (mm)	Electric Driving Current (A)	Transmission (%)	Standard Deviation of the Trans.	Tapering Length (mm)
CHEF1	8	0.32	3.5	sliding		
			3.8	95.4	0.42	33.2
			4	< 70		
CHEF2		0.25	2.8	sliding		
			2.9	94	0.71	29.9
			3	< 80		
CHEF3		0.2	1.8	< 75		
			1.85	91.5	0.58	26.5
			2	< 40		
CHEF4	13	0.32	3.25	Sliding		
			3.5	98.4	0.42	39.7
			3.7	< 60		
CHEF5		0.25	3.1	< 50		
			3.35	97.5	0	44.8
			3.6	< 70		
CHEF6		0.2	1.5	< 70		
			1.7	95.5	1	47
			1.8	0.72		
CHEF7	20	0.32	2.85	< 34		
			3	96	1.5	48.6
			3.5	< 48		
CHEF8		0.25	2.08	Sliding		
			2.2	97.5	1.7	49.1
			2.3	< 70		
CHEF9		0.2	2.4	< 80		
			2.45	97	1.2	42.7
			2.55	broke		

parameter investigated in this study, which is the electrical driving current for the CHEF. For the same CHEF, the heating power generated through the resistant heating of the heating wire is proportional to the square of the driving current according to the equation $P=I^2*R$, where P is the Ohmic heating power, “I” is the driving current, and “R” is the resistance of the heating wire. As a result, the temperature within the CHEF will increase/decrease when the electrical driving

current increase/decrease. A more detailed study on the temperature distribution within the CHEF at different electrical driving currents is presented in section 3.3.2.

The performance of the CHEF was characterized mainly by two parameters, the transmission and the tapering length of the tapered fiber, which are shown in the fourth and sixth columns of the table. For each CHEF design, we have experimentally investigated a range of electrical driving currents for the fiber tapering and identified the optimum current. At these optimum driving currents, the tapered fibers all have an averaged transmission of higher than 90% as shown in the green highlighted rows of the table. The averaged transmissions were acquired from three consecutive experiments and all have a minimum standard deviation as shown in column 5 of the table. In the best cases, tapered fibers with transmissions close to 99% have been demonstrated (see section 3.7 for an example data). These results show that CHEFs of different designs are all capable of fabricating high transmission tapered fibers in a highly repeatable way. It is noted that an electrical driving current slightly deviated from the optimum value, say ± 0.1A, will still allow the CHEF to produce high-transmission tapered fibers. To give the user an idea of the range of the optimum electrical driving current, we have included the upper limits and the lower limits of the electrical driving currents for the fiber tapering in the table. At these limits, the CHEF starts to fail to produce high-transmission tapered fibers due to a too high or too low temperature.

As mentioned in section 3.1, a high-performance tapered fiber should not only have high transmission, but also a suitable tapering length for the desired application. Tapering length of a tapered fiber is determined by the effective heating length (effective heating length is defined in section 1.4.1.2.1) of the heat source (the reason will be detailed in section 3.4). In general, CHEFs with longer ceramic housings will have longer effective heating lengths, and hence can be used to fabricate tapered fibers with relatively long tapering lengths. In fact, as shown in the table, tapered fibers with relative short tapering lengths of 25.4 to 33.5 mm can be fabricated using the CHEF with the 8 mm long ceramic housing, while tapered fibers with relative long tapering lengths of 41.8 to 54.3 mm can be fabricated using the CHEF with the 20 mm long ceramic housing. These results show that it is possible to adjust and optimize the tapered fiber length for different applications by switching between CHEFs with different ceramic housing lengths. However, while the tapered fiber length can be controlled qualitatively, it is difficult to quantitatively control the tapered fiber length using the CHEF. This is because the effective heating length of the CEHF is

related with not only the length of the ceramic housing which can be easily controlled, but also other factors that cannot be well controlled. Particularly, the coil density of the heating coil which as described in the method section cannot be accurately controlled. A denser/looser coil will correspond to a longer/shorter effective heating length of the CHEF, and as a result a longer/shorter tapering length. In practice, a user after a reasonable amount of practice (~ 3 to 4 times) should be able to repetitively produce coils with similar density, which will allow the CHEF to produce tapered fibers with a tapering length variance within ±5 mm. Once a CHEF with an ideal heating coil is fabricated, its effective heating length will no longer changes during its usage and can reliably fabricate high-transmission tapered fibers with the desired tapering length.

One characteristic of the CHEF design that cannot be inferred from the data in the table is the difficultness of its fabrication. Here, drawing on our experience of fabricating the 9 CHEFs used for the parametric study, we give two design guidelines of the CHEFs. Furthermore, by combining these two design guidelines, we have selected a CHEF design that is most suitable for the manual fabrication method described in the method section.

i. Firstly, the ideal ceramic housing length for the CHEF fabrication is around 13 mm. CHEFs with shorter ceramic housings, for example the 8 mm ones, are less thermally insulated from the environment. As a result, to generate the temperature suitable for the fiber tapering they will require a more densely winded heating coil which can be difficult to make. CHEFs with longer ceramic housings, for example the 20 mm ones, do not have the concern of thermal insulation but will require heating coils with longer lengths. While it is easy to increase the length of the heating coil, to also ensure the uniformity of the coil density is challenging. A nonuniform coil density will cause the temperature distribution within the CHEF not suitable for the fiber tapering (detailed in section 3.4). The recommended ~13 mm long ceramic housings, on the other hand, not only have a sufficient thermal insulation but also only require a heating coil length that can be relatively easily achieved.

ii. Secondly, the most suitable heating wire diameter for the fabrication of the coil is ~0.32 mm. Thinner diameter wires, for example the 0.25 mm and 0.2 mm diameter wires, are more difficult to maintain the shape of the coil due to their high flexibility. If the flexible coils expand or shrink after the fabrication, different rounds of the coils will be in contact. This will cause parts of the heating coils to be electrically shorted and cannot generate enough heat for the tapering. While a thicker diameter wire can better maintain the shape

of the coil, it will have a smaller wire resistance, because the wire resistance (R) decrease quickly with the cross-section area A as $R \sim A^{-2}$. With the smaller wire resistance, from the equation $P=I^2*R$ we know that to generate the same heating power will require a higher driving current which may overload the DC power supply. On the other hand, the recommended ~0.32 mm diameter heating wires can well maintain the shape of a coil as long as 13 mm after its fabrication. It can also generate sufficient Ohmic heating power at an electrical driving current less than 4 amperes, which is within the capability of most of the DC power supplies.

Following the above two design guidelines, we recommend CHEF4 in the table with the combination of 13 mm ceramic housing length and 0.32 mm heating wire diameter to be most suitable for our manual fabrication method. Furthermore, since CHEF4 can produce high-transmission tapered fibers with a tapering length of around 40 mm which is suitable for most of the applications, CHEF4 is also in general the most optimum CHEF design.

3.3.2 Temperature characterization of the CHEF

Temperature within the CHEF is critical for the fabrication of high-performance tapered fibers. It directly affects the transmission and the tapering length of a tapered fiber. Here, the relationships between the temperature distribution within the CHEF and the electrical driving current, the ceramic tube length, and the heating coil density were investigated and discussed respectively. The temperature distributions were acquired by measuring at different points along the center axis of the CHEF using a K-type thermocouple (OMEGA).

First, we characterized the relationship between the temperature and the electrical driving current. A CHEF with the design of 13 mm long ceramic housing and 0.32 mm diameter heating coil (the recommended optimum design) was used for the experiment. Temperature distributions within the CHEF at 3.00 A, 3.10 A, and 3.25 A driving current were measured and shown in Figure 40 (A). The results show that the temperature within the CHEF at the same axial position is higher when the electrical driving current is higher. At electrical driving current of 3.25 ampere, the CHEF can produce tapered fibers with final transmissions higher than 95%. At electrical driving current of 3.10 ampere, fibers can still be tapered by the CHEF but will start to slide on the mechanical clamp during the tapering. This is because that at 3.10 ampere driving current, the highest temperature within the CHEF was about the same as the transition temperature of the glass fiber,

and the fibers were not soften enough for a continuous tapering. The averaged final transmission of the tapered fibers fabricated at 3.10 ampere electrical driving current is smaller than 90%. At electrical driving current of 3.00 ampere, the temperature within the CHEF was lower than the transition temperature of the glass fiber. In this case, the fibers were continuously sliding on the mechanical clamp during the tapering and cannot be tapered.

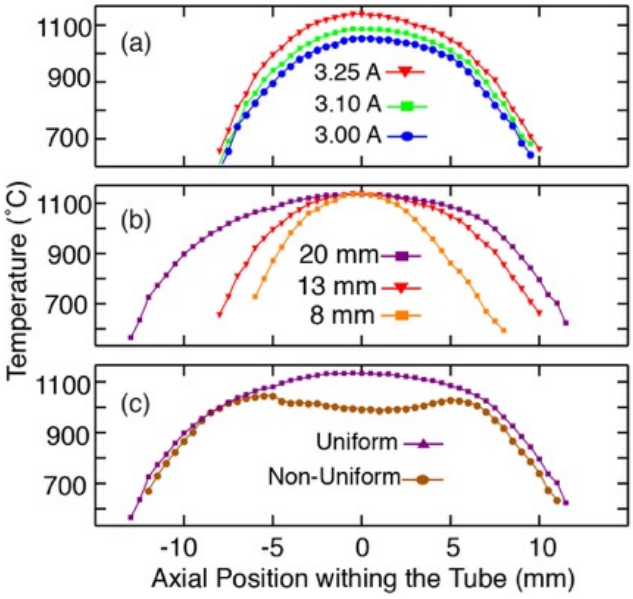

Figure 40 Temperature characterization results of the CHEF. (a) temperatures of the same CHEF at different driving currents. (b) temperatures of CHEFs with different tube lengths at the same driving current. (c) temperatures of CHEFs with uniform and non-uniform coils.

Figure 40 (b) shows the characterization results of temperature distribution within CHEFs of different ceramic housing lengths. From the results we can see that a longer ceramic housing can provide a longer heating zone and hence a longer effective heating length, which means they will produce tapered fibers with longer lengths. However, the above statement is only true when the heating coil densities of different CHEFs are the same. For example, Figure 40 (c) shows the comparison of temperature distributions within two CHEFs that have the same ceramic housing length but different coil densities. The purple triangle marked curve corresponds to the measured temperature within a CHEF that has a uniform coil density that is typical for most of the heating coils we made. The brown circle marked curve corresponds to the measured temperature within a CHEF that has an intentionally winded ununiform coil density. The ununiform heating coil has a looser than typical coil density in the center region. As a result, the center region temperature of the CHEF with the ununiform heating coil is much lower than that of the CHEF with the uniform

heating coil. The largest temperature difference is more than 100ºC. While the CHEF with the uniform heating coil can produce high-performance tapered fibers, the CHEF with the ununiform heating coil cannot taper the optical fiber at all. This means that the CHEF with the ununiform heating coil has an effective heating length of zero. In reality, most of the heating coils do not have such dramatic difference in their uniformity. But the presence of different effective heating lengths in CHEFs with the same ceramic housing length is relatively common. In fact, the reason that in Table 1, tapered fibers fabricated by CHEFs with the same ceramic housing length have different tapering lengths is mainly due to the differences in the heating coil densities. For example, for CHEF1 and CHEF2, CHEF2 has a looser coil density than CHEF1, and hence tapered fibers fabricated by CHEF2 have a shorter tapering length.

Another indication from the results in Figure 40 (C) is that if the heating coil has an ununiform coil density, the temperature within the CHEF will also be ununiform. While any temperatures above the glass transition temperature will allow the glass fiber to be tapered, a higher temperature will cause the glass fiber to be less stiff and be more easily elongated. As a result, a nonuniform temperature distribution will lead to an asymmetric shape of the tapered fiber, which will cause transmission loss to the tapered fiber. This is also the reason why in the guidelines of CHEF design we recommend avoiding long heating coils which is prone to be ununiform due to the manual fabrication method.

3.4 FUNDAMENTAL UNDERSTANDING OF THE FIBER TAPERING PROCESS

3.4.1 Shape of the straight tapered fiber

The shape of a tapered fiber fabricated by a uniform and constant heat-source using the heat-and-pull method can be described by a widely used model [18]. The model is derived based on the assumption of volume conservation of the fiber during the tapering. According to the model, the heat source used for the tapering has a section whose temperature is higher than the fiber's transition temperature. The length of this section is called the effective heating length. During the tapering, the diameter of the fiber within this section will be uniformly shrunk. But once the fiber moves outside this section its diameter will no longer be shrank. In a tapered fiber, the uniformly shrunk region is called the tapered fiber waist, and the regions that connect the tapered fiber waist

to the input and output single mode fiber are called the transition regions. The transition region has an exponentially decreasing diameter resulted from the tapering process [18]. A schematic of the cross-section of the tapered fiber is shown in Figure 41 in a cylindrical coordinate. The origin of the coordinate coincides with the beginning of the input transition region (left). The length of the tapered fiber waist region (h) is the same as the effective heating length (red lines in Figure 41). The total length of the transition region (L) is the same as the elongation of the fiber, which is often referred to as the tapering length (blue lines in Figure 41). The shape of the tapered fiber is symmetric with respect to $z = \frac{h+L}{2}$. The shape of a tapered fiber is fully described using the symmetry and the relations below:

$$r_{transition} = r_0 e^{-\frac{z}{h}} \qquad \left(0 \le z \le \frac{L}{2}\right) \tag{9}$$

$$r_{waist} = r_0 e^{-\frac{L}{2h}} \qquad \left(\frac{L}{2} \le z \le \frac{L+h}{2}\right) \tag{10}$$

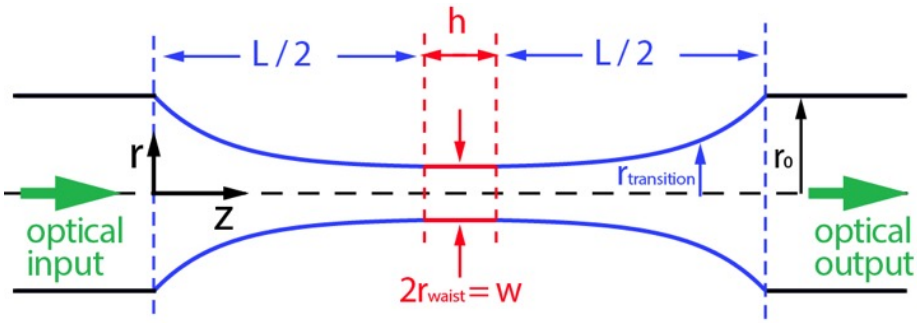

Figure 41 Schematic of the cross section of a tapered fiber along the longitudinal axis.

It is noted that while the model above provides a description of the tapered fiber shape with adequate accuracy for our following analysis, the shapes of most real tapered fibers do not match the model exactly. The deviation from the ideal tapered fiber shape is often due to the nonuniform temperature distribution of the heat source, which can cause the tapered fiber shape to be asymmetric. Compared to a tapered fiber with symmetric shape, a tapered fiber with asymmetric shape has lower optical transmission. The additional transmission loss is due to the guided light couple to higher order modes that are not of the fundamental mode family [18] (e.g. HE_{11} to HE21 mode), which will not happen in a tapered fiber with symmetric shape. For example, the spectrograms in Figure 44 and Figure 45 correspond to the transmission signal of a tapered fiber with asymmetric and symmetric shape respectively. More detailed discussion on these spectrograms on presented in the following sections.

3.4.2 Optical modes evolution in a tapered fiber

To study the evolution of the optical modes in a tapered fiber during its tapering process, we need to model the transition region and the tapered fiber waist region separately. While the tapered fiber waist region with a uniform diameter can be modeled as a straightforward step-index cylindrical waveguide, modeling the transition region that has a more complex geometry is relatively difficult. Analytical model [15] and numerical simulation studying [18] the optical modes in the transition region can be found in previous works. Here, only the more relevant optical modes in the tapered fiber waist region is studied.

At the beginning of a tapering process, all the light is confined within the fundamental HE_{11} mode of the core of the tapered fiber waist and is guided by the core-cladding boundary. However, as the diameter of the tapered fiber waist keeps decreasing, the fiber core will eventually become too small to guide the light and the light will escape into the cladding and guided by the cladding-air boundary. The tapered fiber waist will become a multi-mode step-index cylindrical waveguide whose effective core is the fiber's cladding and whose effective cladding is the air. Optical modes supported by the multi-mode cylindrical waveguide are found by solving the rigorous dispersion equation (11) for a step-index cylindrical waveguide without using the weakly guiding ($n_0 \cong n_1$) approximation. The weakly guiding approximation cannot be used here because for the cladding-air waveguide the difference of the refractive index between the effective core (fiber cladding, $n_{cladding} = n_1 \approx 1.447$) and the effective cladding (air, $n_{air}=n_0=1$) is relatively large and the light is under the strong guiding condition [15].

$$\left[\frac{J_n'(u)}{uJ_n(u)}+\frac{K_n'(w)}{wK_n(w)}\right]\left[\frac{J_n'(u)}{uJ_n(u)}+\left(\frac{n_0}{n_1}\right)^2\frac{K_n'(w)}{wK_n(w)}\right]=n^2\left(\frac{1}{u^2}+\frac{1}{w^2}\right)\left[\frac{1}{u^2}+\left(\frac{n_0}{n_1}\right)^2\frac{1}{w^2}\right] \quad (11)$$

In the dispersion equation (1) shown above, $u = d\sqrt{k^2n_1^2-\beta^2}, w = d\sqrt{\beta^2-k^2n_0^2}$ in which d is the diameter of the tapered fiber waist, $k=\frac{2\pi}{\lambda}$ is the propagation constant of the light in vacuum, and $\beta = k\, n_{neff}$ is propagation constant of the optical modes where n_{eff} is the effective refractive index of that mode, $J_n(u)$ and $J_n'(u)$ are the nth order Bessel function of the first kind and its derivative with respect to u respectively, $K_n(w)$ and $K_n'(w)$ are the nth order modified Bessel function of the second kind and its derivative with respect to w respectively. Dispersion curves showing the calculated effective refractive indices of different optical modes at different tapered fiber radiuses are plotted in Figure 42. From Figure 42 we can see that as the diameter of the multi-mode tapered fiber waist was being continuously shrunk, both the number of the

supported optical modes and the effective refractive index (n_{eff}) of each mode are continuously changing. Due to this change, the co-propagating optical modes will beat with each other and renders a time-dependent optical transmission that oscillates in a complicated way. More detailed discussion on this oscillation will be discussed later in section 3.5.2. To better visualize the cutoff of different higher order modes as the fiber diameter decreases, we calculated the electric field distributions of different optical modes supported by the waveguide when its diameter is approaching the critical cutoff value using the finite element method (FEM). The electric field distributions of the supported modes at different tapered fiber diameters are shown in the inset above the dispersion curve in Figure 42. The simulation results show that as the radius of the tapered fiber waist shrunk from 0.85 μm to 0.45 μm, all the higher order modes were cutoff and only the fundamental HE_{11} mode was supported at the radius of 0.45 μm.

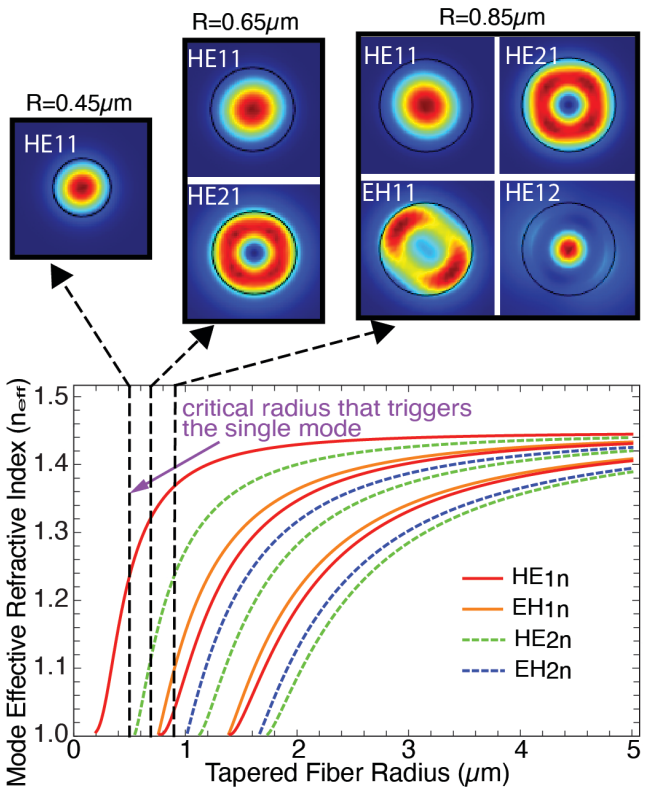

Figure 42 A plot of dispersion curves for different optical modes. The simulation results on top of the dispersion curve plot show the supported optical modes at different tapered fiber radiuses. Inset (a-c) show the electric field distribution of different modes supported at radius 0.45μm, 0.65μm, and 0.85μm. The color in the electric field distribution plot indicates power of the field, with red color the highest value and blue color the lowest value.

It is noted that, while the calculation shows that the multi-mode tapered fiber waist can support several higher-order modes before it reaches the critical radius, it does not mean that all these modes will be excited and propagate in the tapered fiber waist. To study exactly what modes will be generated will require analysis on the transition region of the tapered fiber, which as mentioned previously is not in the scope of this work. In general, if the tapering process is strictly adiabatic, the fundamental HE_{11} mode will be adiabatically coupled into and out of the tapered fiber waist, and no higher-order modes will be generated. However, since most of the tapering process in practice is not strictly adiabatic, higher-order modes will be excited and co-propagate with the fundamental mode into and out of the tapered fiber waist during the tapering.

3.5 EXPERIMENTAL AND THEORETICAL STUDY OF THE OPTICAL TRANSMISSION OF THE TAPERED FIBER

3.5.1 Experimentally measured time-domain and frequency-domain optical transmission signals

During the tapering process, the optical transmission for an adiabatically tapered fiber is different from that of a non-adiabatically tapered fiber. In an adiabatic tapering process of a single mode fiber (SMF-28), at any given time point, the optical transmission will only oscillate at a relatively small amplitude. This oscillation is due to the system noises such as noises from the laser source and the photodetector. However, our tapering processes are not strictly adiabatic, and the transmission signal will exhibit a more complicated oscillation pattern. A typical example of such oscillating transmission signals is shown in Figure 43 (a) and (b). The CHEF used for the experiment was made from a 0.32 mm diameter heating wire and a 13 mm long ceramic housing tube. Figure 43 (a) is a normalized time-domain oscillation signal acquired at a sampling rate of 1000Hz. Figure 43 (b) (i-vi) are power spectra calculated from samples acquired at different tapering lengths. The sampling time is one second for all the power spectra. The color of the power spectra in Figure 43 (b) correspond to the color of the vertical lines in Figure 43 (a) which indicate at what tapering lengths the power spectra were taken. Here, we first look at the qualitative relation between the oscillation amplitude of the transmission signal and the peaks in the power spectra at

different tapering lengths. A more detailed quantitative analysis of the relationship will be discussed in the following section 3.5.2.

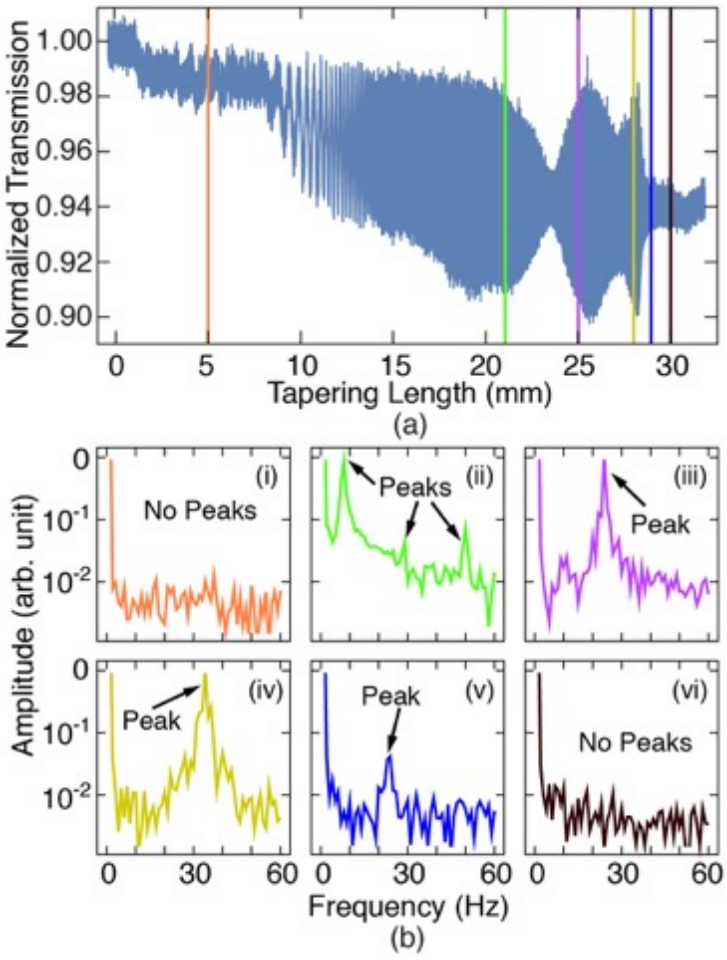

Figure 43 (a) Normalized time-domain transmission signal plotted against the tapering length of the fiber. The normalization is conducted by dividing the original time-domain transmission of the tapered fiber by the averaged transmission of an un-tapered SMF-28 fiber at the same optical input. (b) Power spectra of the sampled transmission signal at different tapering lengths. (i)-(vi) were taken at tapering lengths of 5, 21, 25, 28, 29, and 30 mm respectively

At the beginning of the tapering process, the time-domain optical transmission only oscillates at the system-noise level, and the corresponding power spectrum (orange spectrum in Figure 43 (b) (i)) shows no peaks in the plot. As the fiber diameter being further decreased, at the tapering length of 21 mm, the time-domain transmission signal shows a higher oscillation amplitude and a more complicated oscillation pattern. The power spectrum that corresponds to this period (green spectrum in Figure 43 (b) (ii)) shows three peaks. These peaks are due to the beating between the higher order modes and the fundamental mode. At the tapering length of 25 mm, as

shown in Figure 43 (b) (iii), there is only one peak left in the power spectrum. The disappearance of the other two peaks are due to the cutoff of the corresponding higher order modes due to the continuously decreasing tapered fiber waist diameter. Figure 43 (b) (iv-vi) show the frequency-domain signals that correspond to the end of the tapering process. First, from the tapering length of 28 mm (Figure 43 (b) (iv)) to the tapering length of 29 mm (Figure 43(b)(v)) both the oscillation amplitude of the time-domain signal and the amplitude of the peak in the power spectra have decreased. This means that the energy coupled to the higher order mode that is beating with the fundamental mode has decreased. From the tapering length of 28 mm Figure 43 (b) (iv) to the tapering length of 30 mm Figure 43 (b) (vi), while there is no obvious change in the oscillation magnitude of the time-domain transmission signal, it is clear that all the peaks in the power spectra has disappeared, which means the single-mode state of the tapered fiber waist has been triggered.

3.5.2 Theoretical analysis of the optical transmission signal

From the experimental results above, we know that the beating between the higher order modes and the fundamental mode can results in a complicated oscillating transmission signal. To better understand this signal, we analyzed the co-propagation of different optical modes in a non-adiabatically tapered fiber. The propagating optical modes vary in time and along the tapered fiber as $exp[i(\beta_i z - \omega t)]$, where z is the propagation length along the z-axis defined in Figure 41, and β_i is the propagation constant of the guided optical mode. β_i can be written as: $\beta_i = \frac{2\pi n_{effi}}{\lambda}$, where n_{effi} is the effective refractive index of the optical mode. Different optical modes have different propagation constants. When two optical modes co-propagate in an optical fiber, they will beat spatially and when they recombine at the output transition region, they will have a relative phase difference Φ_{ij} [40]: [40]

$$\Phi_{ij}(L) = 2\left\{\int_{L1}^{\frac{L}{2}} \Delta\beta_{ij}\left(r_{transition}(z)\right)dz + \Delta\beta_{ij}(r_{waist})\frac{h}{2}\right\} \tag{12}$$

In equation (12) shown above, $\Delta\beta_{ij}$ is the difference of the propagation constant between two different modes at different tapered fiber radius and is z-dependent. The integration parameter L_1 is the z-coordinate at which the two modes start to co-propagate along the tapered fiber. L_1 is a constant that is different for different higher-order modes. The integration parameter L is the tapering length of the tapered fiber. The efficiency of the two beating modes recombining back to

the output single mode fiber varies with the accumulated relative phase difference Φ_{ij} as $Cos(\Phi_{ij})$ [109]. Since the accumulated relative phase difference Φ_{ij} is a function of L, the recombination efficiency of the modes will vary during the tapering process. This variation in the recombination efficiency is the cause for the beating in the transmission signal. Combining equation (9), (10), and (12), the spatial beating frequency K_{ij} of the transmission signal can be written as :

$$K_{ij} = \frac{1}{2\pi}\frac{d\Phi_{ij}(L)}{dL} = \frac{1}{2\pi}\left(\Delta\beta_{ij}(r_{waist}) - \frac{r_{waist}}{2}\frac{d\Delta\beta_{ij}}{dr}\Big|_w\right) \tag{13}$$

Since our measured transmission signal is in the time-domain, the time-domain beating frequency $f_{ij} = \frac{1}{2\pi}\frac{d\Phi_{ij}}{dt}$ is more relevant to our experiment. Using the relationship $\frac{dL}{dt} = v_t$, where v_t is the total tapering speed. The relationship between the spatial beating frequency and the time-domain beating frequency f_{ij} can be written as:

$$f_{ij} = \frac{1}{2\pi}\frac{d\Phi_{ij}}{dt} = \frac{1}{2\pi}\frac{d\Phi_{ij}}{dL}\frac{dL}{dt} = \frac{1}{2\pi}v_t\frac{d\Phi_{ij}}{dL} = \frac{1}{2\pi}v_t K_{ij} \tag{14}$$

The time-domain beating frequencies (f_{ij}) at different tapering lengths can also be experimentally found from the real-time transmission samples as shown in Figure 43 (b). The peak frequencies in the experimentally measured spectra matched the time-domain beating frequencies calculated using theoretical equation (14) (calculation not shown). However, from the discrete spectra plot in Figure 43 (b) it is not obvious how the beating frequency f_{ij} continuously changes during the tapering process. To better capture the dynamics of the f_{ij} during the tapering process, including its amplitude change and frequency shift, we plotted the power spectra at different tapering lengths throughout the whole tapering process in a spectrogram as shown in Figure 44. In the spectrogram the y-axis is the time-domain beating frequency, the x-axis is the tapering length, and the brightness of the color in the spectrogram shows the amplitude of the frequency domain signal. The bright yellow intensity curves show the time-domain beating frequencies f_{ij} between different pairs of co-propagating modes. To identify the corresponding optical modes of the f_{ij} in the spectrogram, we fitted the f_{ij} using the analytical expression shown in equation (14). The effective heating length h is used as the fitting parameter to make the analytical f_{ij} fitting curve overlaps with the f_{ij} intensity curve in the spectrogram. From the fitting results, we determined two pairs of co-propagating modes, the EH_{22} and HE_{11} modes (red line) and the HE_{12} and HE_{11}

modes (black line). From the spectrogram we can clearly see the generation, shifting, and the disappearance of the time-domain beating frequencies f_{ij} during the tapering process predicted by the theory.

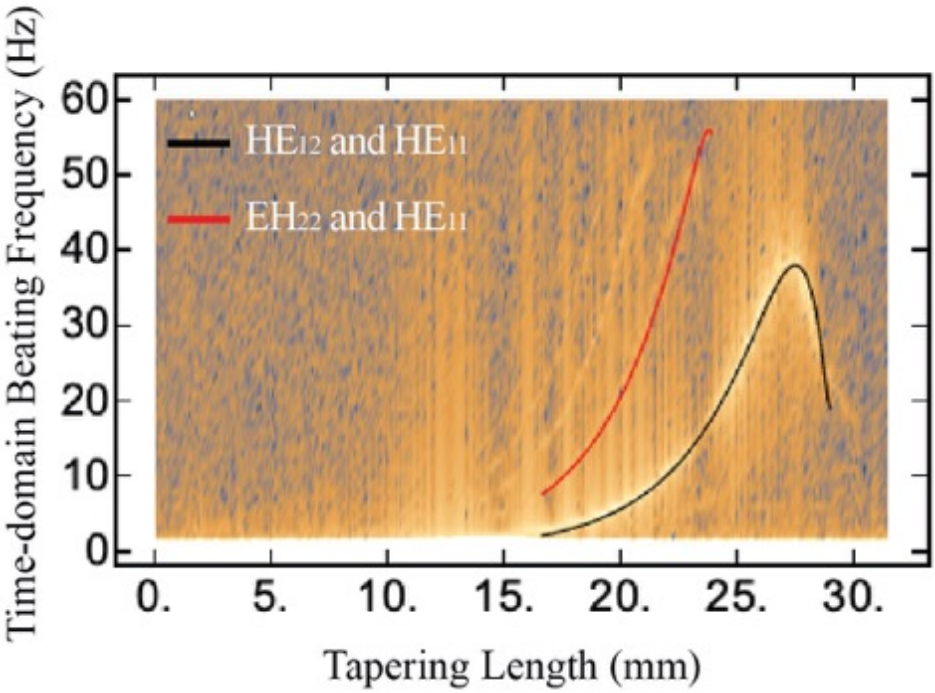

Figure 44 Spectrogram showing the evolution of the beating frequency. The solid curves are analytical fitting curves using equation (14).

3.6 DEVELOPMENT OF A RELIABLE FIBER TAPERING MONITORING METHOD

Single mode operation is desired at the tapered fiber waist region for characterizing integrated photonic devices, such as on-chip micro-resonators. In such applications, an ideal single mode to single mode coupling prevents parasitic coupling to unwanted device modes and readily enables the critical coupling, both of which help to achieve a minimum coupling loss. As a result, it is important to ensure that the fabricated tapered fiber has a single-mode tapered fiber waist. However, as mentioned in the previous section, most of the tapering processes are not adiabatic, and during the tapering process higher-order modes can always be excited and propagate in the waist region. Therefore, it is important to make sure that the diameter of the tapered fiber waist has been decreased enough to cut off all the higher-order modes and the single-mode state of the tapered fiber waist has been triggered. Although a single-mode tapered fiber waist can always be

achieved by decreasing the diameter of the tapered fiber waist, over-decreasing the diameter can result in a mechanically weak tapered fiber and even breakage. Therefore, an ideal time to stop the tapering process is right after the single-mode state of the tapered fiber waist has been triggered. This time-sensitive requirement necessitates a reliable monitoring method during the tapering process, which enables the real-time identification of the triggering of the single mode state and allows the tapering to be promptly stopped.

The most widely used monitoring method is based on the time-domain optical transmission signal of the tapered fiber, such as the one described in Chapter 2. In the time-domain-based method, the triggering of the single-mode state is determined by the change of the oscillation amplitude of the time-domain transmission signal. The feasibility of the time-domain-based method relies on the assumption that the beating-induced oscillation has a significantly larger amplitude compare to that of the system-noises-induced oscillations. With this assumption, when the last higher order mode in the tapered fiber waist has been cut off and the beating-induced oscillation has died out, there will be a large drop in the amplitude of the transmission signal. However, this assumption is not necessarily true, and the largest amplitude drop of the transmission signal might occur before the last higher-order mode is cut off. For example, in Figure 43 (a), the largest drop of the oscillation amplitude happened between the tapering length of 28 mm and 29 mm while the HE_{12} higher order mode still exists. Furthermore, right before the last higher order mode was cut off, which is between the tapering length of 29 mm and 30 mm, the oscillation amplitude of the beating-induced oscillation is on the same level of the system-noises-induced oscillations. In this case, when the last higher-order mode is cut off in the tapered fiber waist, the user cannot accurately determine the triggering of the single-mode state based on the small changes in the oscillation amplitude of the transmission signal. As a result, the transmission-amplitude based monitoring method could easily cause misjudgments of the single-mode triggering, which will lead to a multi-mode tapered fiber waist.

To more reliably identify the triggering of the single-mode state of the tapered fiber waist, we implemented a frequency-based monitoring method. In our frequency-based monitoring method, the triggering of the single-mode state is determined by the vanishing of the peaks in the frequency-domain signal. This method is based on the fact that the peak will and only will appear when there is higher order mode co-propagating in the tapered fiber waist. The reasoning for this correlation can be found in section 3.5.2. Unlike the time-domain transmission-amplitude based

monitoring method, as shown in Figure 43 (b)(v-vi), the vanishing of the peaks/peak in the frequency-domain signal can be easily identified even when the beating-induced transmission oscillation has a small oscillation amplitude (Figure 43 (a)). To achieve real-time monitoring, we integrated the frequency-based monitoring method with a LabVIEW program, which allows us to transform the time-domain transmission signal into the frequency domain with a refresh rate of 1 second. This enabled us to reliably determine the triggering of the single-mode state of the tapered fiber waist in real time and to stop the tapering process promptly.

3.7 EXPERIMENTAL DEMONSTRATION OF A CLOSE TO PERFECT-ADIABATIC STRAIGHT TAPERED FIBER

Highly adiabatic tapered fibers are desired in many applications [9]. This is because the adiabaticity will determine a tapered fiber's efficiency of coupling light to and from external systems [18]. Using the CHEFs, especially the ones with the recommended optimum design of 13 mm long ceramic housing and 0.32 mm diameter heating coil, highly adiabatic tapered fibers with transmissions higher than 95% can be routinely fabricated. In the best cases, tapered fibers with close to perfect-adiabaticity and a transmission close to 99% have been demonstrated. As an example, Figure 45 shows the time-domain and the frequency-domain transmission signals recorded during a close to perfect-adiabatic fiber tapering process. In this tapering process, the total tapering speed is set to 0.2 mm/s and a CHEF with the recommended optimum design was used. To better understand the differences between the close to perfect-adiabatic tapered fibers and the more typical high-transmission but less adiabatic tapered fibers, we analyzed and compared their time-domain and frequency-domain transmission signals.

Firstly, the normalized time-domain transmission signal of the close to perfect-adiabatic tapered fiber (Figure 45 (a)) has a much smaller oscillation amplitude than that of the less adiabatic tapered fiber (Figure 43 (a)). For the less adiabatic tapered fiber, the largest oscillation amplitude in the normalized transmission signa is around 8%, while for the close to perfect-adiabatic tapered fiber, the largest oscillation amplitude is around 2% throughout the whole tapering process. The reason for this difference is because that in a close to perfect-adiabatic tapered fiber, only a small fraction of the input light is coupled into the higher-order mode and contributed to the beating-induced oscillation. In fact, the oscillation amplitude of the beating-induced oscillation is so small

that it is already close to that of the system-noises-induced oscillation and has caused quantization error in the signal due to the limited resolution of the optical detection system.

Secondly, comparing to the spectrogram of the less adiabatic tapered fiber (Figure 44), the spectrogram of the close to perfect-adiabatic tapered fiber is less noisy and shows only one visible intensity curve that corresponds to the beating between the higher order mode and the fundamental mode. Using the fitting method described earlier, we identified the higher order mode to be the HE_{12} mode. This result shows that during the tapering process of a close to perfect-adiabatic tapered fiber, not only the energy coupled to the higher order mode is small, but also only one higher order mode (HE_{12}) is generated through the whole tapering process.

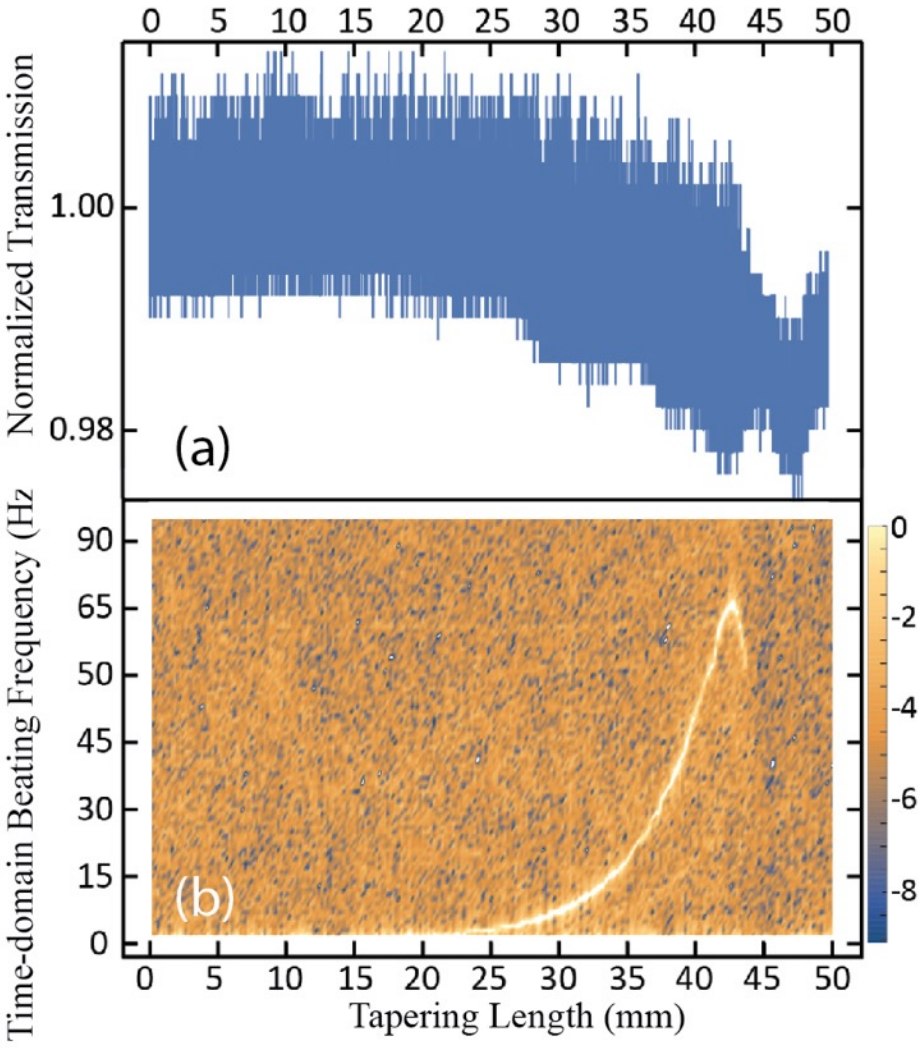

Figure 45 (a) Time-domain transmission recorded during the fabrication of a close to perfect-adiabatic tapered fiber. (b) A spectrogram showing the frequency-domain signal of the close to perfect-adiabatic tapered fiber.

Also, by comparing the time-domain and frequency-domain transmission signals of the close to perfect-adiabatic fiber tapering process (Figure 45 (a) and (b)), it again shows the advantage and necessity of the frequency-domain-based monitoring method we have discussed in section 3.6. The time-domain signal cannot be used for determining the triggering of the single mode state of the close to perfect-adiabatic tapered fiber, because the beating-induced oscillation is buried within the system-noises-induced oscillations throughout the whole tapering process as shown in Figure 45 (a). The only information related to the optical modes provided by the time-domain signal is that when the averaged transmission started to decrease at the tapering length of ~25 mm, it signals that light energy started to couple from the fundamental HE_{11} mode to the higher order HE_{12} mode. In comparison, as shown in Figure 45 (b), the frequency domain signal in the spectrogram clearly shows the evolution of the optical modes within the tapered fiber, including the generation of the higher-order mode, the beating-frequency shift, and most importantly, the single-mode triggering.

3.8 SUMMARY

In this chapter, a low-cost and highly accessible heat source, ceramic housed electric furnace (CHEF), is experimentally demonstrated. The CHEF-based fiber tapering setup can fabricate high-transmission adiabatic tapered fibers in a highly repeatable fashion. The performance of the CHEF was experimentally investigated in a parametric study. Recommendations on the design parameters of the CHEF was given based on the parametric study. The temperature distributions within the CHEFs of different designs are experimentally characterized. Fundamental understanding of the optical modes evolution in a tapered fiber is presented. Based on this fundamental understanding, a new frequency-signal-based monitoring method for the fiber tapering is developed. The frequency-signal based monitoring method can reliably determine the triggering of the single mode state of the tapered fiber, which is challenging for previous monitoring methods. This monitoring method will greatly benefit applications that require the tapered fiber to be both at a single mode state and have a fiber diameter that has not been over decreased (overly decreased diameter will cause the tapered fiber to be mechanically weak). Using the CHEF-based fiber tapering setup and the frequency-based monitoring method, a close to perfect-adiabatic tapered fibers is experimentally demonstrated and analyzed based on the optical waveguide theory.

Chapter 4 D-SHAPE FIBER-TIP RELATIVE HUMIDITY SENSOR BASED ON LOSSY MODE RESONANCE

In this chapter we switch gears from the tapered fibers to another type of specially shaped optical fibers that can allow the fiber-guided light to interact with the environment, namely, the D-shape fiber. The D-shape fiber-tip sensor we have developed can measure relative humidity and local moisture content using the lossy mode resonance signal generated by the sensor. This is the first time that the lossy mode resonance is demonstrated on a single-mode fiber with a fiber-tip form factor. The fiber-tip form factor will allow the sensor to access locations with limited space and requires only one small opening for the sensor implementation. This is also the first time that a D-shape lossy mode resonance sensor is being used for relative humidity/moisture sensing. To fully understand the performance of the sensor, its working principle is studied using numerical simulation and analytical analysis together with fundamental understandings provided by previous works. The sensor's response to relative humidity changes is experimentally characterized using a custom-built humidity chamber. Other than relative humidity, the sensor's capability of indirectly measuring the moisture content change of a food sample through local relative humidity changes within the food sample was also experimentally demonstrated.

The rest of this chapter is organized in the following way. In section 4.1, recent development of optical-fiber-based LMR sensors is briefly reviewed. In section 4.2, the design and fabrication method of the D-shape fiber-tip lossy mode resonance sensor is introduced. In section 4.3, a numerical simulation and analytical analysis are carried out to study the working principle of the D-shape-fiber-based lossy mode resonance. The relationship between the relative humidity and LMR signal is also explained in this section. In section 4.4, a relative humidity characterization system based on a customized humidity chamber is introduced, followed by an experimental characterization of the senor's response to relative humidity changes. In section 4.5, the D-shape fiber-tip sensor's potential of monitoring moisture content change in food samples in real time was experimentally demonstrated.

4.1 REVIEW OF THE RECENT DEVELOPMENT OF LMR OPTICAL FIBER SENSORS

In recent years, the relatively new lossy-mode-resonance (LMR) optical fiber sensors have been extensively explored. Their versatility is exploited for sensing of various physical parameters including voltage [78], electric current [61], relative humidity [77], gas [61], chemical, and bio-chemical [110]. The LMR optical fiber sensors have the advantages of high sensitivity, small footprint, and can be used in harsh environment [78]. However, most of the lossy-mode-resonance optical fiber sensors have an in-line design [76], in which the input and output fiber ends are on different sides of the sensor. Such design requires a large spatial clearance on both sides of the fiber sensor to avoid the breakage of the input and output fibers. Particularly, for small food samples in food processing, it is difficult to implement an in-line sensor. However, it is important to measure the moisture content of food samples during the food manufacturing process, because the moisture content can influence the food's textural properties and its shelf-life [111]. With such a need, lossy-mode-resonance sensors that are located at the fiber tips are desired because of the easy implementation, probe-like form factor, and high mechanical robustness.

4.2 SENSOR DESIGN AND FABRICATION

In this section, we introduce an LMR-based D-shape fiber sensor with a fiber-tip form factor, as shown in the 3 schematics in Figure 46 (a) and (b). The tip form factor of the sensor allows it to be used as a needle probe and to access narrow spaces with a single opening as small as its diameter (~125 μm). The tip of the sensor has a D-shape cross-section, which is fabricated using a custom side-polishing setup. A ~195 nm SnO_2 film was sputter-coated onto the side-polished fiber surface, acting as the sensing layer that supports the lossy mode resonance and changes refractive index when the environmental relative humidity changes.

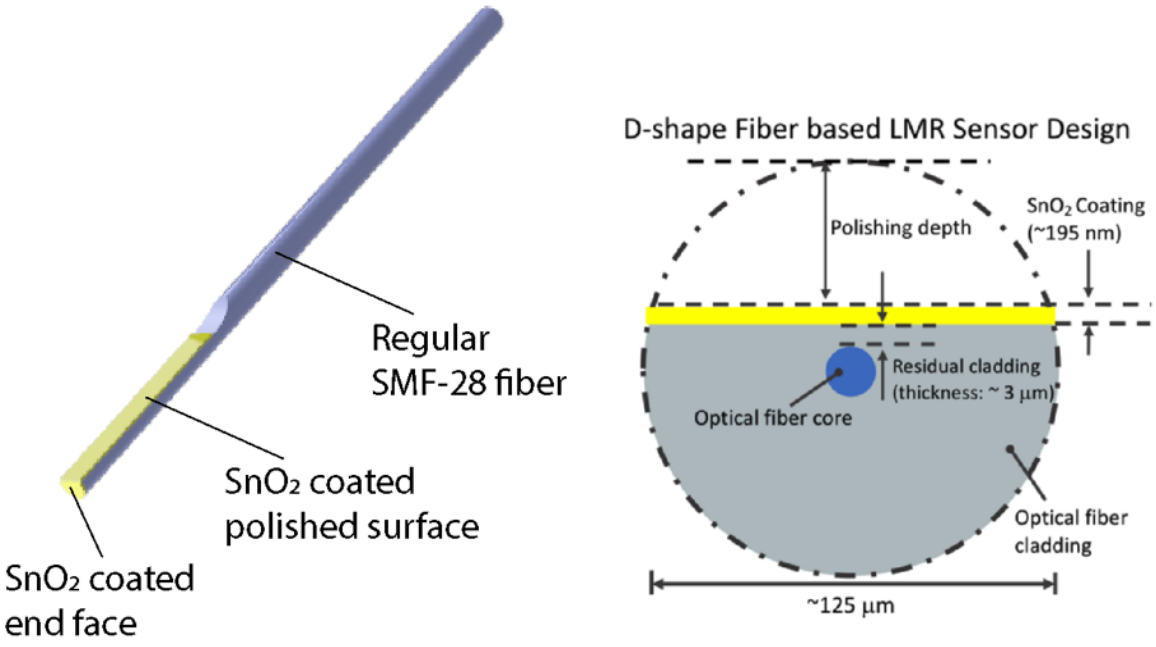

Figure 46. (Left) 3D model of the side-polished D-shape optical fiber. (right) schematic showing the cross section of the D-shape fiber sensor.

Fig. 47 (a) and (b) show the photo and schematic of the in-house side-polishing setup that we have developed to fabricate the D-shape fiber tip. Before the polishing, a single-mode fiber (SMF-28) was putting under tension and partially wrapped around a polishing rod. The polishing rod is mounted on and driven by a DC motor. The polishing time is determined by monitoring the drop of the real-time optical transmission from the fiber that is being polished. After the polishing, as shown in the fabrication schematic in Fig. 47(d), the polished fiber was cleaved into two side-polished fiber tips, whose SEM images are shown in Fig. 1(e). Finally, a ~195 nm thick SnO_2 film was coated on the polished surfaces.

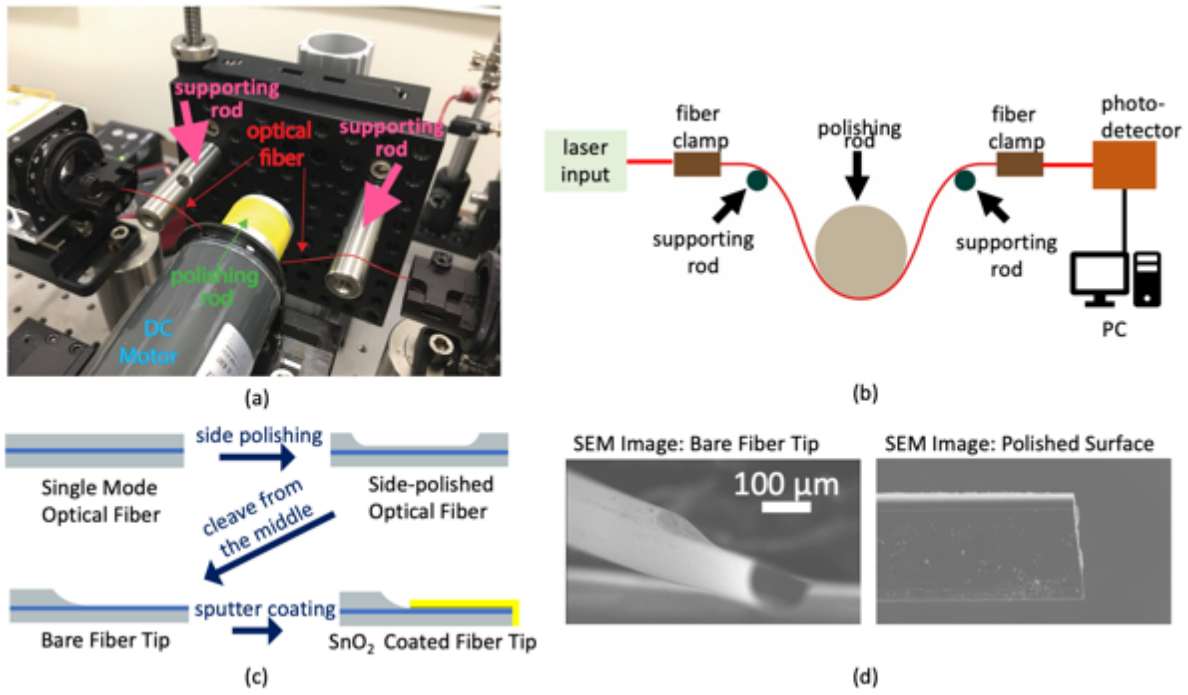

Figure 47. (a) Photo and (b) schematic of the fiber side-polishing setup. (c) Schematics of the sensor's fabrication process. (d) SEM photos of the side-polished fiber tip

After the D-shape fiber tip was fabricated, the residual cladding thickness (d_r) of the D-shape fiber was characterized using a microscope. Microscope images of the end face of the D-shape fiber tips with different residual cladding thicknesses were shown in Figure 48. The residual cladding thickness of each D-shape fiber tip was calculated using a computer program. First, the length represented by each pixel in the microscope images was calculated. Then, the position of the core was found by fitting the boundary of the D-shape fiber using a circle with equivalent diameter of 125 µm (red circles in Figure 48). Finally, the residual cladding thickness, which is the distance between the polished surface (represented by the red lines in Figure 48) and the fiber core (represented by the blue circles in Figure 48), were calculated. The d_r of a D-shape fiber is critical for the LMR generation. If the d_r is too thick, the evanescent field of the core mode will not be able to reach the SnO_2 film to excite the lossy mode resonance; if the d_r is too thin, a large portion of the evanescent field will be propagating within the SnO_2 film and cause large transmission loss even at non-resonance wavelengths (because the SnO_2 film is optically lossy). The d_r of an LMR D-shape fiber is between ~2 to ~4 µm. At this residual cladding thickness, the evanescent field of the core mode can reach the SnO_2 film and excite the LMR at the resonance wavelength but will not cause big transmission loss at non-resonance wavelengths. The two columns in Figure 48 show

the microscope photos of both successfully polished D-shape fibers with ideal d_r and failed ones with either too thick or too thin d_r. Typically, with the customized fiber polishing setup, from 10 polished fibers, at least 7 fibers will have a d_r between ~2 to ~4 μm and can be used as LMR sensors.

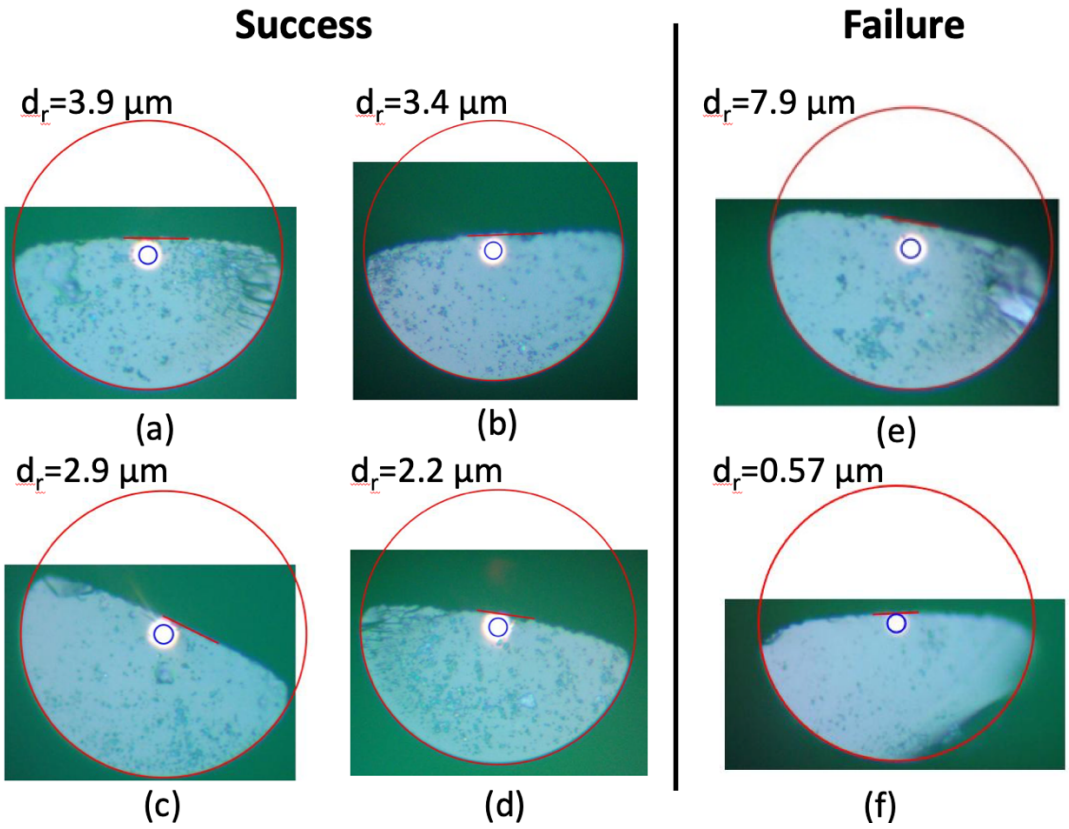

Figure 48. (a-d) Microscope images of the end face of successfully polished D-shape fiber tips. These D-shape fibers have a residual thickness (d_r) between 2 to 4 μm. (e-f) Microscope images of the end faces of unsuccessfully polished D-shape fiber tips. (e) has a too large residual thickness, and (f) has a too thin residual thickness.

4.3 WORKING PRINCIPLE OF THE D-SHAPE LMR RELATIVE HUMIDITY SENSOR

In an LMR sensor, light that is guided in the fiber's core mode can be coupled into the optically lossy film layer when reaching the polished fiber section. The coupling efficiency is determined by two conditions: the electromagnetic field overlapping and the phase (effective mode index) matching between the core mode and the film mode. These conditions are influenced by the film's refractive index and the light's wavelength. When the film's refractive index increases the resonance wavelength will red shift and vice versa. At the lossy mode resonance, the coupling

efficiency reaches a maximum, resulting in a minimum power left in the core. In this section, the lossy mode resonance phenomenon is studied using both numerical simulation and analytical analysis. The analytical analysis provides a method to calculate the optical transmission of the LMR sensor, while the numerical simulation of the optical modes provides the parameter (imaginary part of the effective mode index) required for the transmission calculation. Potentially, a finite-difference time-domain method (FDTD) can provide simulation results that is closer to the real sensor, but this topic is outside the scope of this dissertation and is not discussed in this section.

4.3.1 Analytical analysis of the transmission of an LMR sensor

For an optical mode propagating along the optical fiber, the electric and magnetic field can be written as the following:

$$\boldsymbol{E}(\boldsymbol{x},\boldsymbol{y},\boldsymbol{z}) = e(x,y)exp(-j\beta z) \tag{15}$$

$$\boldsymbol{H}(\boldsymbol{x},\boldsymbol{y},\boldsymbol{z}) = h(x,y)exp(-j\beta z) \tag{16}$$

where **E** and **H** are the total electric and magnetic field, e and h are the transverse electric and magnetic field, and β is the propagation constant. The propagation constant can be written as $\beta = k_0(n_{eff} + jn'_{eff})$, where k_0 is the propagation constant in vacuum, and n_{eff} and $n_{eff}{}'$ are the real and imaginary parts of the effective mode index. The optical power flow carried by an optical mode through the fiber is characterized by the Poynting vector **S** as:

$$\boldsymbol{S} = \frac{1}{2}Re(\boldsymbol{E} \times \boldsymbol{H}^*) = \frac{1}{2}Re(e \times h^*)\exp(-2n'_{eff}k_0 z) \tag{17}$$

The total power flow in an optical fiber carried in one optical mode can be calculated by integrating the Poynting vector across an infinite cross section as $P_{total}(z) = \iint \boldsymbol{S}\, dA = \frac{1}{2}\mathrm{e}^{-2n'_{eff}k_0 z} \iint Re(e \times h^*)\, dA$. The optical transmission of a fiber of length l can be written as $T = \frac{P_{total}(l)}{P_{total}(0)}$. Since the term $\iint Re(e \times h^*)\, dA$ is a constant for a fixed optical mode, the transmission can be simplified to be $T = \mathrm{e}^{-2n'_{eff}k_0 l}$. From the derivation above we know that to calculate the transmission of an LMR fiber sensor, we only need to know the imaginary part of the effective mode index of the propagating mode which is n'_{eff}. In the next section, n'_{eff} of the optical mode propagating in the LMR fiber is calculated using numerical simulations.

4.3.2 Numerical simulation of the LMR phenomenon

A numerical simulation is conducted using a commercial finite element method (FEM) software (COMSOL Inc.). In the simulation, optical modes at the cross section of a D-shape fiber is solved at different wavelengths. The model used for the simulation is shown in Figure 49. It consists of 4 domains, the optical fiber core and cladding, the SnO_2 film coating, and the environment (air). The refractive index of the core is set to be 1.447, the refractive index of the cladding is set to be 1.4419, the real part and imaginary part of the refractive index of the SnO_2 film is set to be 1.77 and 0.004 respectively. The refractive index of the environment is set to be 1. A scattering boundary condition is applied to the boundary of the environment (the red outmost circle in the model). With this boundary condition, the outgoing light will not be reflected at the environment boundary, in other words, the environment boundary (the outmost circle in the model) is transparent to the outgoing light wave.

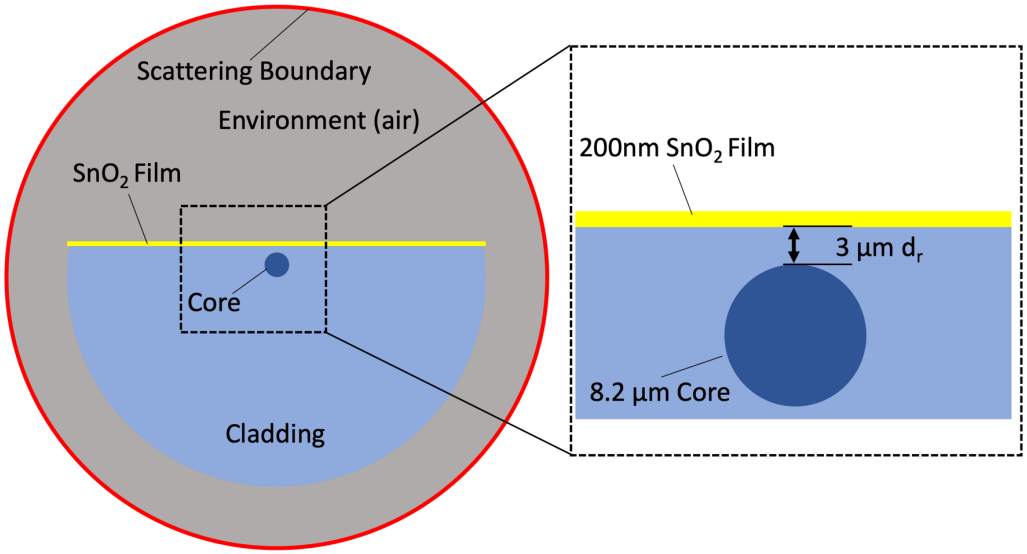

Figure 49 Schematic of the model for optical mode analysis of the LMR sensor. The SnO_2 film has a thickness of 200 nm. The residual thickness of the D-shape fiber is 3 μm.

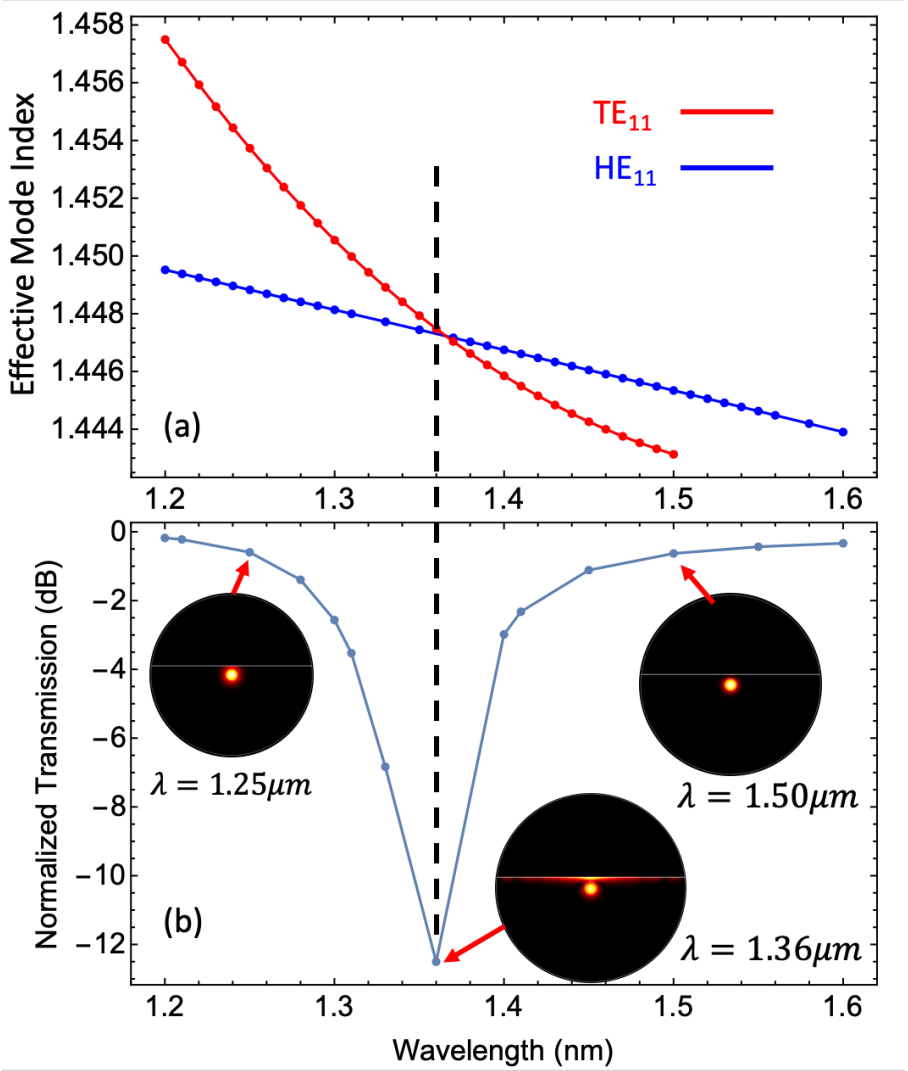

Figure 50 (a) The dispersion curve of the isolated film mode (TE_{11}) and core mode (HE_{11}). The isolated film mode is calculated using a D-shape fiber model with the core having the same refractive index as the cladding. The isolated core mode is calculated using a D-shape fiber model with the film having the same refractive index as the cladding. (b) shows the calculated optical transmission of the LMR fiber sensor. The three inset images show the optical energy distribution of the super-mode at different wavelengths. The dashed line show that the resonance is located at the wavelength where the film mode and the core mode have the same effective mode index.

The numerical simulation shows that light propagate along the D-shape fiber in the so-called super-mode, which is a hybridization of the film mode (TE_{11}) and the core mode (HE_{11}). The optical energy intensity distribution of three selected super-modes at different wavelengths are shown in Figure 50 (b). From the simulation results we can see that the energy is most efficiently coupled from the core mode to the lossy film mode at the LMR wavelength. At this wavelength, the

corresponding effective mode index of the film mode and the core mode are about the same, as shown in Figure 50 (a) and (b). In fact, previous work has shown that this is wavelength is also where the electromagnetic field of the core mode and the film mode overlap the most [32]. Using the imaginary part of the effective mode index of the super-mode $n_{eff}{}'$ provided by the numerical simulation and the equation $T = \mathrm{e}^{-2n'_{eff}k_0 l}$, we can calculate the normalized transmission of the LMR fiber sensor as shown in Figure 50 (b). From the transmission plot we can see that indeed, the lowest transmission is at where the core mode most efficiently couple to the film mode.

4.3.3 Fundamental understanding of the influence of the relative humidity on the LMR signal

In this section we address the question: how the relative humidity changes can be read out by the LMR sensor. It has been demonstrated that the LMR wavelength is sensitive to the environmental refractive index changes [76]. When the environmental refractive index increases/decreases, the LMR spectrum will shift to a longer/shorter wavelength. As shown in Figure 51. (a), the environment seen by the SnO_2 sensing layer consists a layer of adsorbed water molecules. Since water has a larger refractive index than air (n_{water}=1.33, n_{air}=1), when the thickness of the adsorbed water layer changes, the effective environmental refractive index seen by the fiber sensor will also change. And because the thickness of this adsorbed water layer has a positive correlation with the relative humidity, one can use the LMR fiber as a relative humidity sensor. To better understand the correlation between the adsorbed water thickness and relative humidity, we need to examine how the water molecules are attached to the fiber sensor surface. The attached water can be separated in two layers based on the different adsorption mechanisms as shown in Figure 51. (b), namely the chemisorbed and the physisorbed layer. The chemisorbed water layer is formed once the SnO_2 film coating is exposed to the water molecules in the air. This is because that water is a polar molecule, and the negatively charged oxygen of the water molecule is attracted to the cationic Sn molecules of the SnO_2 film to form a strong hydrogen-oxygen chemical bond [112]. After this non-reversible chemisorbed layer is formed, additional water molecules will then attach to the chemisorbed water molecules through a physisorption process. The physisorbed layer is hold together by a weak electrostatic force. As a result, the physisorption process is a reversible process.

The thickness of the physisorbed layer is determined by the relative humidity. When the relative humidity increases, the increased water vapor pressure in the environment will cause more water adsorption and a thicker physisorbed layer; when the relative humidity decreases, the decreased water vapor pressure will cause more adsorbed water to leave the physisorbed layer and result in a thinner physisorbed layer. As a result, when RH increases, the physisorbed water layer thickness will increase, which will cause the film's effective refractive index to increase, and the LMR spectrum will shift to a longer wavelength, and vice versa.

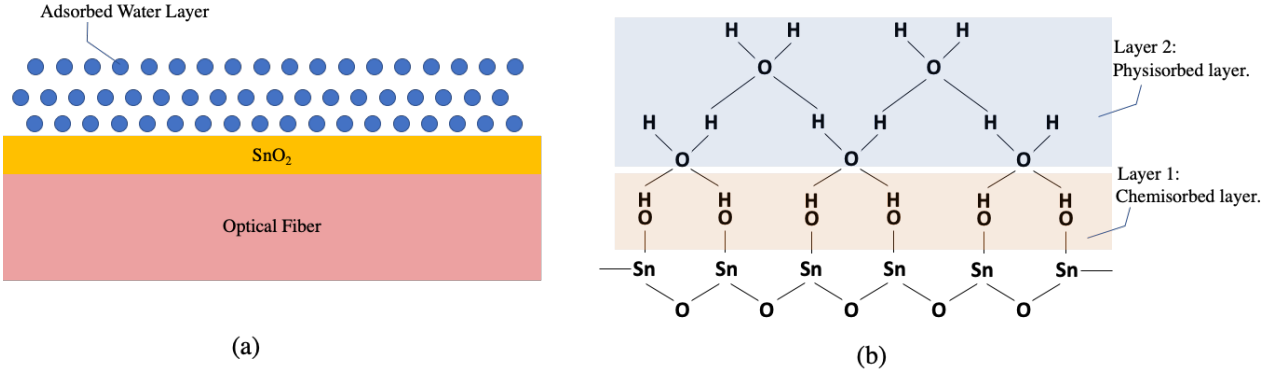

Figure 51 (a) A schematic showing the water molecules adsorbed by the SnO2 film coating on the optical fiber. (b) A schematic showing the chemical bonding of the chemisorbed and physisorbed water layer.

4.4 CHARACTERIZATIONS OF THE LMR SENSOR FOR RELATIVE HUMIDITY (RH) SENSING

4.4.1 Optical system for the sensor characterization

The optical system used to characterize the LMR sensor is shown in Figure 52. A broadband superluminescent diodes (SLD) from Thorlabs (S5FC1021P, Thorlabs Inc.) with center wavelength at 1310 nm and 85 nm bandwidth is used as the light source. The polarization of the light from the SLD can be adjusted using an optical polarization controller (FPC032, Thorlabs Inc.) before input into the LMR sensor. An optical circulator (CIR1310-APC, Thorlabs) is used to couple the input light to the LMR sensor and the output optical signal to the spectrometer (BTC261P-512-S, B&W TEK).

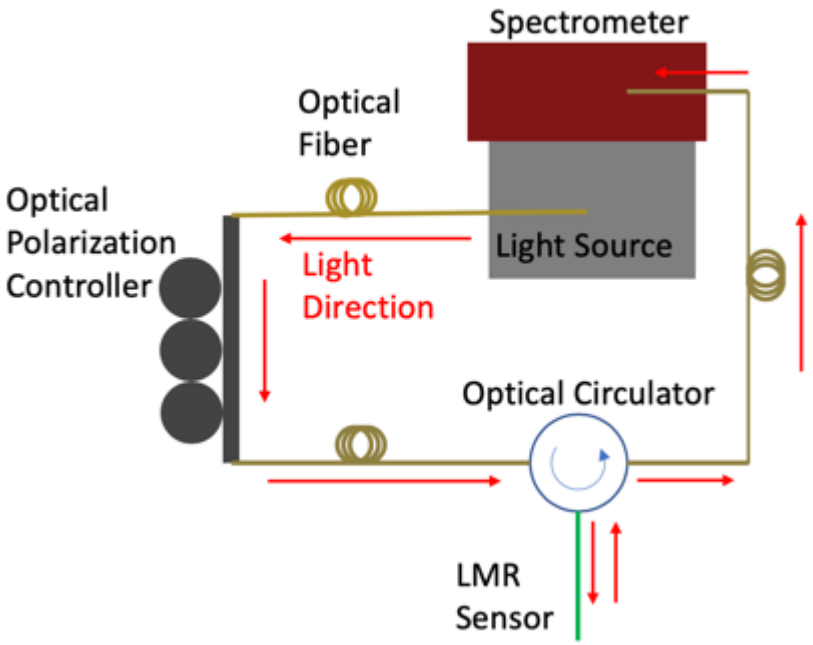

Figure 52 Schematic of the optical system for the LMR sensor characterization.

4.4.2 Experimental characterization of the LMR signal

Experimentally measured LMR spectrum

The sensor's LMR spectrum is characterized using the optical system described in section 4.4.1 (Figure 52). An LMR spectrum of the sensor acquired in room environment at relative humidity around 23% is shown in Figure 53. The resonance wavelength of the LMR signal is at around 1346.5 nm. The full width half maximum (FWHM) of the resonance is around 15 nm.

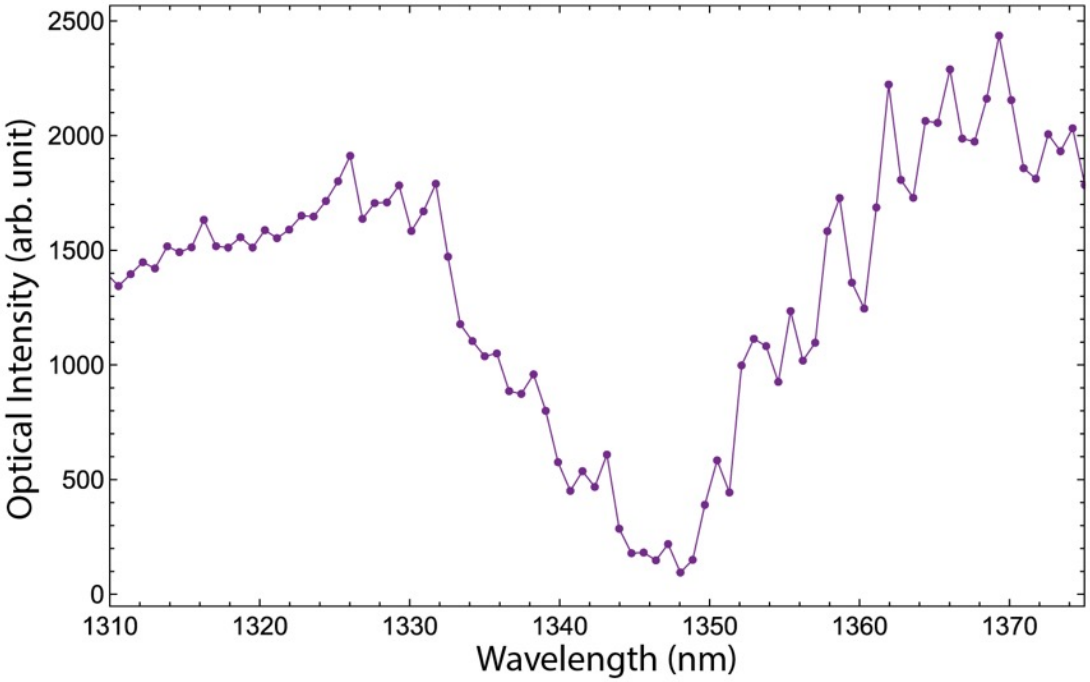

Figure 53 Experimentally measured LMR spectrum of the sensor.

4.4.3 Development of the characterization system

4.4.3.1 Customized RH chamber

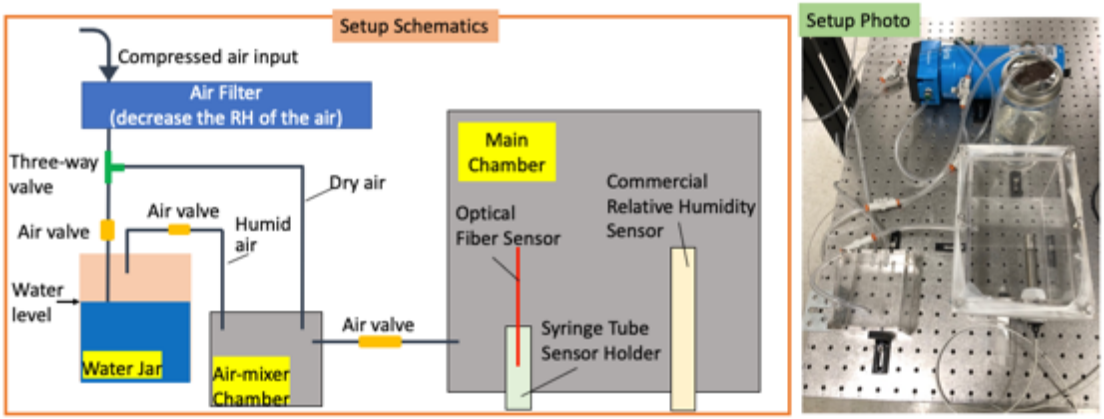

Figure 54 Schematics and photo of the customized humidity chamber.

In this section, a relative humidity (RH) characterization system based on a customized RH chamber is introduced. The schematics and the photo of the humidity chamber is shown in Figure 54. The customized RH chamber has two parts, a main chamber and an air-mixer chamber. Filtered

compress air (dry air) and air that has passed through water (humid air) will first be mixed at the air-mixer chamber before output into the main chamber. The pre-mixing of the humid and dry air at the air-mixer chamber will allow the RH within the main chamber to be adjusted more quickly and allow the RH within the main chamber to be hold at a same RH with lower fluctuations. By adjusting the air valves, both the RH and the flow rate of the air input into the main chamber can be adjusted. The optical fiber sensor and a commercial electrical RH sensor (RH-USB, OMEGA) are inserted in the main chamber, as shown in the schematics in Figure 54. The electrical sensor is used as a reference to characterize the optical sensor's response to RH changes.

4.4.4 Experimental characterization of the LMR sensor's dynamic response to relative humidity

In this section, experimental characterizations of the LMR fiber-tip sensor using the relative humidity chamber is presented. The characterized sensor parameters include the sensitivity, response time, and dynamic response of the sensor. To characterize the sensitivity of the sensor, we changed the RH value within the humidity chamber in steps over ~8500 seconds and recorded the optical spectra as shown in Figure 55 (a) and (b). The shift shown in the zoomed-in spectra (Figure 55 (b)) is due to the shift of the LMR wavelength when the environmental RH changes. There are two ways that the shift of the LMR spectrum can be characterized, one by monitoring the shift of the resonance wavelength, another one by monitoring the optical intensity change at a fixed wavelength that correspond to the shoulder of the resonance. While both methods are commonly used, comparing to the resonance-wavelength-based method, the intensity-based method only require information from a single wavelength and hence can allow a faster sampling time. Here the intensity-based monitoring method is used to experimentally characterize the sensitivity of the LMR fiber-tip sensor. Optical intensity changes at the wavelength that correspond to the shoulder of the LMR signal at different RH values were recorded as shown in Figure 55 (c). For each RH value, a 100-seconds long optical intensity data was chosen, and their average value was used to represent the optical intensity of the corresponding RH value. The averaged optical intensity at different RHs were plotted in Figure 55 (d). By fitting the plotted data, the sensitivity of the sensor was calculated to be around 0.15% RH/Int, meaning that for 1% of RH value change, the optical intensity will change ~6.7 units. It is noted that the sensitivity of the sensor may vary

between different measurements, a more detailed characterization of the sensor is required in the future.

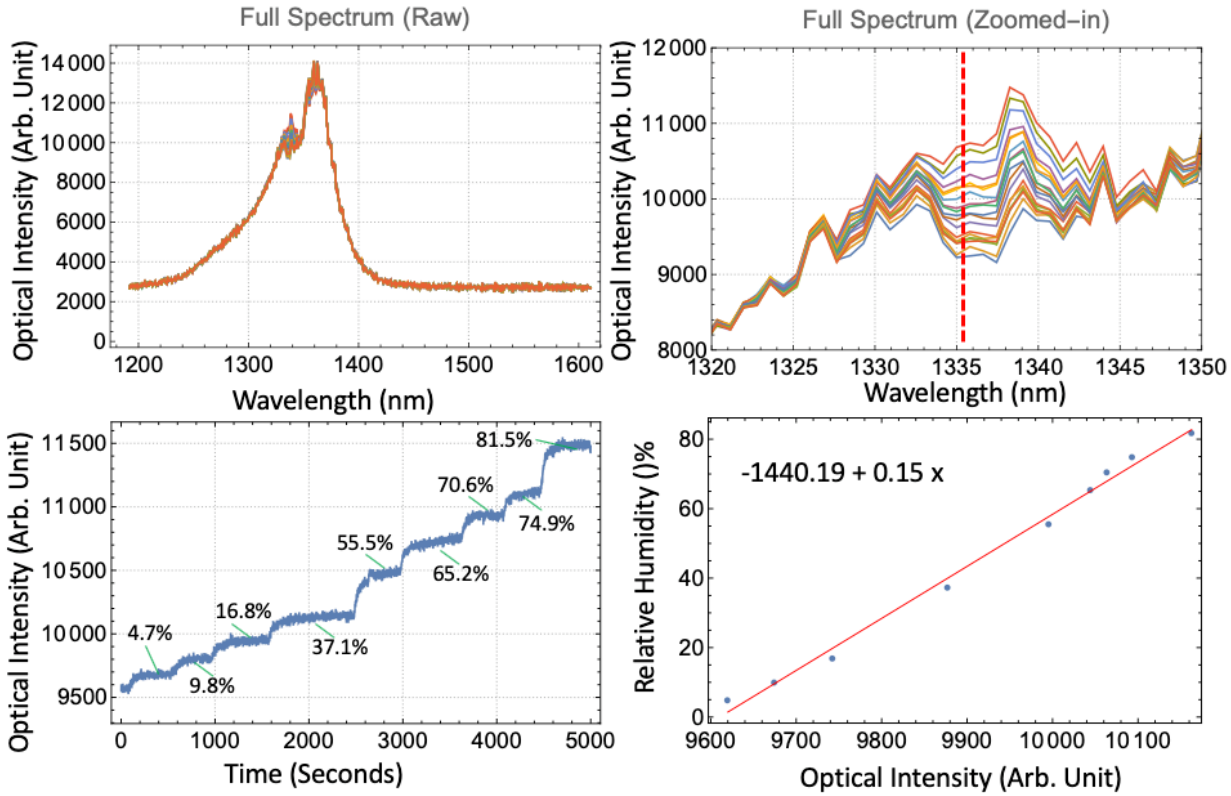

Figure 55 (a) and (b) show the LMR spectra measured at different RH values and the zoomed-in LMR spectra at different RH values. (c) Optical intensity changes recorded over 8500 seconds at the pixel indicated by the red-dashed line in (b). Each intensity step corresponds to a different RH value. (d) A plot showing the optical intensities at different RHs, and a linearly fitted curve showing the relationship between the relative humidity and the optical intensity of the LMR spectra at the pixel number 183.

Response time and dynamic response

The LMR sensor's response time and response to a dynamically changing RH signal were experimentally characterized. In the experiments, the response time of the sensor is defined as the time required for a sensor to reach equilibrium from the starting RH value to the end RH value. As a result, the defined response time is dependent on the absolute RH value change. To characterize the sensor's response time, the LMR fiber sensor and an electrical reference sensor were inserted into the humidity box. A step RH change from ~5% to ~83% was then introduced to the humidity box at t = 0 second. Both the LMR sensor's and the electrical reference sensor's responses to this step RH change were recorded and shown in Figure 56 (a). From the result we can see that the

LMR fiber sensor has a response time of ~480 seconds for a step RH change from ~5% to ~83%. Another parameter that can help to characterize the sensor's response time is the time required for the sensor to start to respond to the RH change. As shown in Figure 56 (b), after the step RH change was introduced at t = 0 second, the optical fiber sensor started to respond at around t = 55 second, while the electrical sensor started to respond at around t = 65 second. These results show that while the optical and electrical sensor have about the same response time, the optical sensor require a shorter time to start to respond to RH changes.

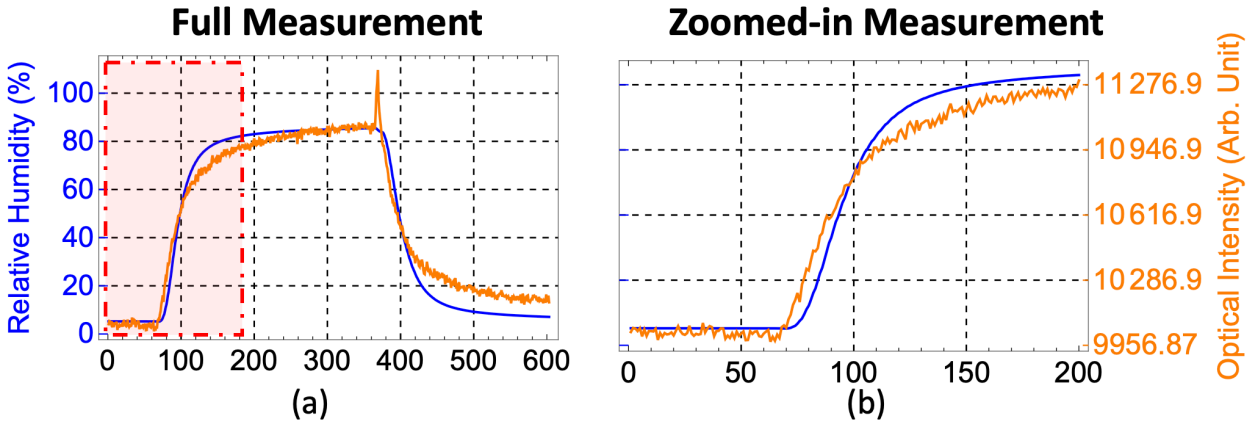

Figure 56 (a) Optical (orange) and electrical sensor (blue) responses to a step RH change from ~5% to ~83%. (b) Zoomed-in plot of the full response. It shows the sensor measurements from 0 to 200 seconds, which corresponds to the red highlighted section in (a). The plot shows that the optical sensor started to respond to the RH change ~10 seconds earlier than the electrical sensor.

To characterize the LMR fiber sensor's dynamic response, the sensor was subject to a periodically changing RH. Both the RH value read out by the electrical sensor and the optical intensity change at the shoulder position of the LMR resonance were recorded during the experiment as shown in Figure 57. The electrical signal and the optical signal were overlapped for each RH variation cycle. This overlapping shows that the optical fiber sensor has a low hysteresis and can be used to measure dynamically changing RH signals.

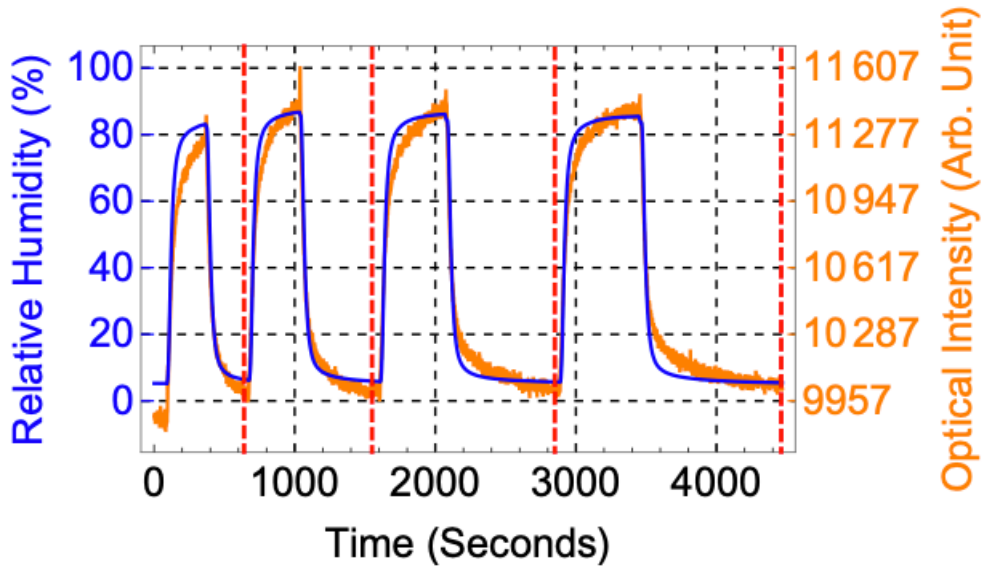

Figure 57 Characterization of the optical fiber sensor's dynamic response. The blue curve shows the RH measured by the electrical sensor; the orange curve shows the optical intensity signal measured by the optical fiber sensor.

4.5 Experimental Demonstration of the Sensor's Capability of Measuring Moisture Content in Food Samples

One important motivation of developing the LMR relative humidity sensor is using it to monitor the moisture of food samples during their drying processes. To achieve such moisture content monitoring, one need to insert the fiber sensor into the food sample to measure the local relative humidity of the food. The food's moisture content has a positive correlation to the local relative humidity within the food, higher moisture corresponds to higher relative humidity and vice versa. In this section, the LMR fiber sensor's response to food sample's moisture content change was experimentally characterized. The results demonstrated that the LMR fiber sensor can be potentially used for real-time moisture monitoring in the drying process of food.

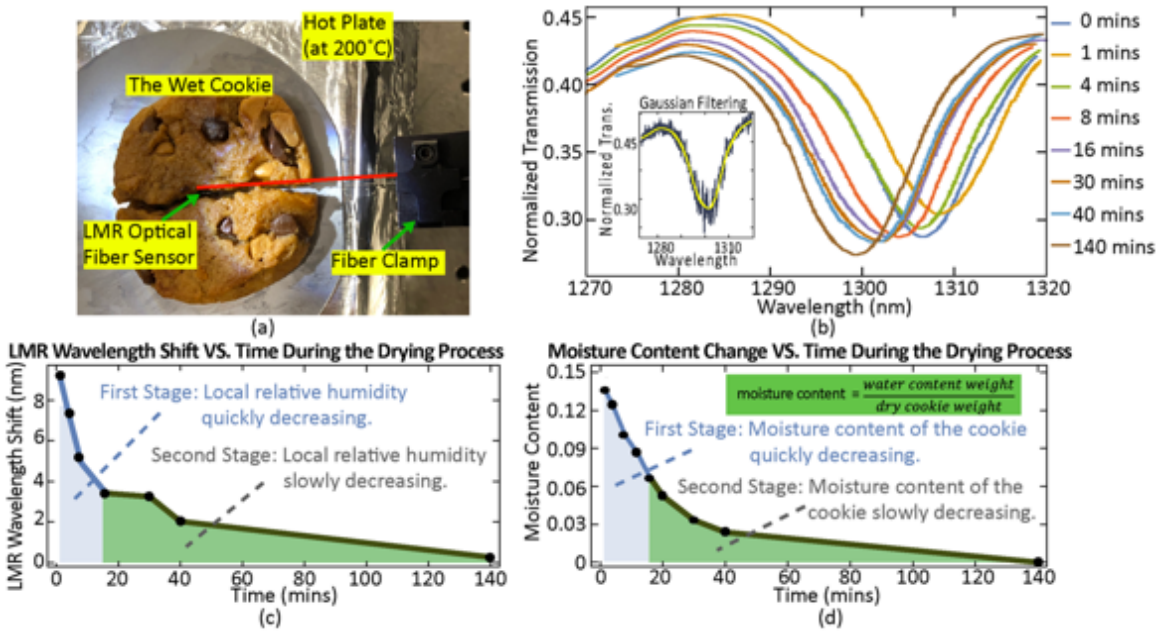

Figure 58 (a) Photo of the experimental setup for the cookie's water content measurement. (b) Experimentally measured LMR spectra during the drying process of the cookie. The inset shows the original LMR spectrum and the corresponding Gaussian filtered spectrum. (c) The LMR wavelength shift and (d) the moisture content change at different time points of the drying process.

The sensors are characterized in the following way. A wet cookie with a small (~3 mm wide) gap was placed on a 200 ˚C hot plate. The LMR fiber-tip sensor was inserted into the wet cookie through the gap, as shown in Figure 58(a). During the drying process, as the water was evaporated from the cookie, both the cookie's moisture content and the local relative humidity in the gap decreased and were read out by the fiber-tip sensor. The moisture content here is defined as the ratio between the weight of water within the cookie and the dry cookie weight. The dry cookie weight was measured 140 minutes after the cookie was put on the hot plate. The experimentally measured and Gaussian filtered LMR spectra at different time points of the drying process are shown in Figure 58 (b). The corresponding LMR wavelength shifts are shown in Figure 58 (c). We have also measured the moisture content of the food product at different time point, as shown in Figure 58 (d). By comparing Figure 58 (c) and (d) we can see that the LMR wavelength shift and the moisture content change has a very similar trend. This confirms our sensor's capability of moisture measurement. Moreover, the plots show that a moisture content change lower than 3% can be differentiated using the LMR spectra. These results show that the LMR fiber-tip sensors hold high potential for in-situ moisture content monitoring in the drying processes of foods. Such

sensors can enable real-time feedback control of the drying process and improve the energy efficiency of the drying process. It is noted however, the characterization conducted here didn't give a specific relationship between the food moisture content and the optical signal. Further characterization is underway to investigate the sensor's response at different food moisture content and the temperature influence to such measurements.

4.6 SUMMARY

In this chapter, we developed an LMR based optical fiber-tip relative humidity/moisture sensor and a customized fiber side polishing setup for the sensor fabrication. To the best of the author's knowledge, this is the first time that the lossy mode resonance has been demonstrated on a D-shape fiber tip. The working principle of the lossy mode resonance has been investigated using numerical simulations. The sensor's sensitivity and dynamic response to the relative humidity have been experimentally characterized using a customized humidity chamber. The sensor's dynamic response to moisture content change was characterized using a cookie sample. The preliminary characterization results show that the LMR sensor is capable of reading out moisture content change smaller than 3%. These results demonstrated that the LMR fiber-tip sensor can potentially be used for in-situ relative humidity and water content monitoring for the process control in food manufacturing, particularly food's drying process. A more detailed characterization of the sensor's response to moisture content change is underway, including response time, sensitivity, resolution, and temperature dependency.

Chapter 5 RECONFIGURABLE ACRYLIC-TAPE-HYBRID MICROFLUIDICS

As we have previously mentioned, the integration of special-shape optical fibers with microfluidics can benefit many applications, such as optical sensing [12] and microparticle manipulations [34]. However, existing microfluidic platforms, particularly the most widely used PDMS-based microfluidic platform, are not ideal for such integrations (detailed reasons are listed in section 1.4.1.3.3). In this chapter, we developed an acrylic-tape hybrid microfluidic platform that can allow the special-shape optical fibers (or optical fibers in general) to be integrated with the microfluidic devices in a straightforward way. The devices are fabricated by a readily accessible, straightforward process, and has a reversible tape-based sealing mechanism. While the sealing mechanism can reliably confine the fluids within the channel, ***it can also allow optical fibers to be inserted and aligned in the microfluidic channel in a straightforward way.*** Furthermore, this sealing mechanism can allow in-the-field reconfiguration of the device functions by changing tapes or the optical fibers inside.

The rest of this chapter is organized in the following way. In section 5.1, a brief review of the existing microfluidic platforms is presented. In section 5.2, the fabrication methods of the microfluidic device are introduced. In section 5.3, the flow in the acrylic microfluidic channels is experimentally characterized. In section 5.4, function multiplexing using the reconfigurable acrylic-tape microfluidic device is experimentally demonstrated. In section 5.5, two on-chip pumps, the on-chip paper pump and the on-chip pipette tube pump are experimentally demonstrated. In section 5.6 In section 5.6, monodisperse droplets generation is experimentally demonstrated on a syringe pump driven acrylic-tape microfluidic device. In section 5.7, preliminary experimental results showing the acrylic-tape microfluidic devices' capability of optical fiber integration is demonstrated.

5.1 REVIEW OF EXISTING MICROFLUIDIC PLATFORMS

Since the first demonstration1, polydimethylsiloxane (PDMS) [113] has been a dominant microfluidic platform with applications across a wide range of fields, including biology [114–116], chemistry [114, 117], soft electronics6, and biomedical analyses [119]. However, PDMS based microfluidic devices have a number of limitations. The fabrication process is based on

photolithography and soft lithography, which are time-consuming, need relatively expensive equipment such as plasma cleaners, and typically require a clean room environment. It can be difficult to translate the process into industrial mass productions8. In addition, most of the O_2 plasma enabled PDMS-glass bonding is irreversible, while reversible sealing is beneficial because it allows reconfiguration of device functions and thorough sterilization of microfluidic channels.

Various alternative microfluidic platforms have been proposed to address the challenges of PDMS platform, including paper microfluidics [121, 122], 3D-printed microfluidics [123,124], injection-molded blocks microfluidics [124], and acrylic microfluidic [126–131]. The fabrication of these platforms does not need clean room facilities or plasma bonding as PDMS devices do. Paper microfluidics have benefits of low cost, lightweight, and disposable, compared with the PDMS platform. However, paper microfluidic devices are mechanically weak and have poor flow control [134]. 3D-printed and injection-molded blocks microfluidics have benefits of function reconfigurability, which means the functions of the microfluidic devices can be changed without the need of fabricating new parts. This is realized by their modular designs [123–125], which enable different blocks to be rearranged in the field to provide different functions. However, both their fabrication and assembling processes are relatively complex and cannot be done by a novice without proper training. Acrylic microfluidic devices have benefits of mechanical durability and low cost. Furthermore, acrylic, also referred to as poly(methyl methacrylate) (PMMA), is non-porous and hence can prevent adsorption or absorption related contaminations. In most of the previously demonstrated acrylic microfluidics, the bonding between the channels and the covers was realized by hot laminating machine [127], thermal fusion bonding [128] or solvent-assisted lamination [127], all of which are permanent and needs special equipment. In addition, these bonding processes take longer than 20 minutes. Recently, the bonding between two pieces of acrylic has been realized more quickly by double-sided tapes [129]. However, this bonding mechanism is not reconfigurable because the channels were formed inside the tapes. Reconfigurable microfluidic devices made from low cost and mechanically durable materials in a rapid fashion are yet to be demonstrated. Reconfigurable microfluidic devices made from low cost and mechanically durable materials in a rapid fashion are yet to be demonstrated. In addition, inserting optical fibers in the microfluidic devices is challenging particularly for PDMS microfluidics. There is a strong need for a new microfluidic platform that is easily accessible, low-cost, and compatible for specially shaped optical fibers.

5.2 FABRICATION METHODS AND MATERIALS

Fabrication steps of the acrylic-tape hybrid microfluidic devices are shown in Figure 1(a). Firstly, the computer-aided-design (CAD) drawings of the devices, including flow channels and inlets/outlets, are developed on a computer. Secondly, a CO2 laser cutter is used to fabricate the devices on commercially available acrylic boards. Inlets/outlets are fabricated by cutting through the boards, while channels are engraved into the surface by laser ablation. Details on the laser ablation method can be found in previously published works [127, 131]. Briefly, when a laser spot that has an appropriate power moves across the acrylic surface, instead of cutting through the acrylic board, it heats and vaporizes a small volume of acrylic material. The resulted cavities left on the acrylic surface serve as the microfluidic channels. Finally, the channels are sealed with functionalized single-sided tapes, completing the fabrication process. A detailed discussion of the functional tapes is presented in the following sections.

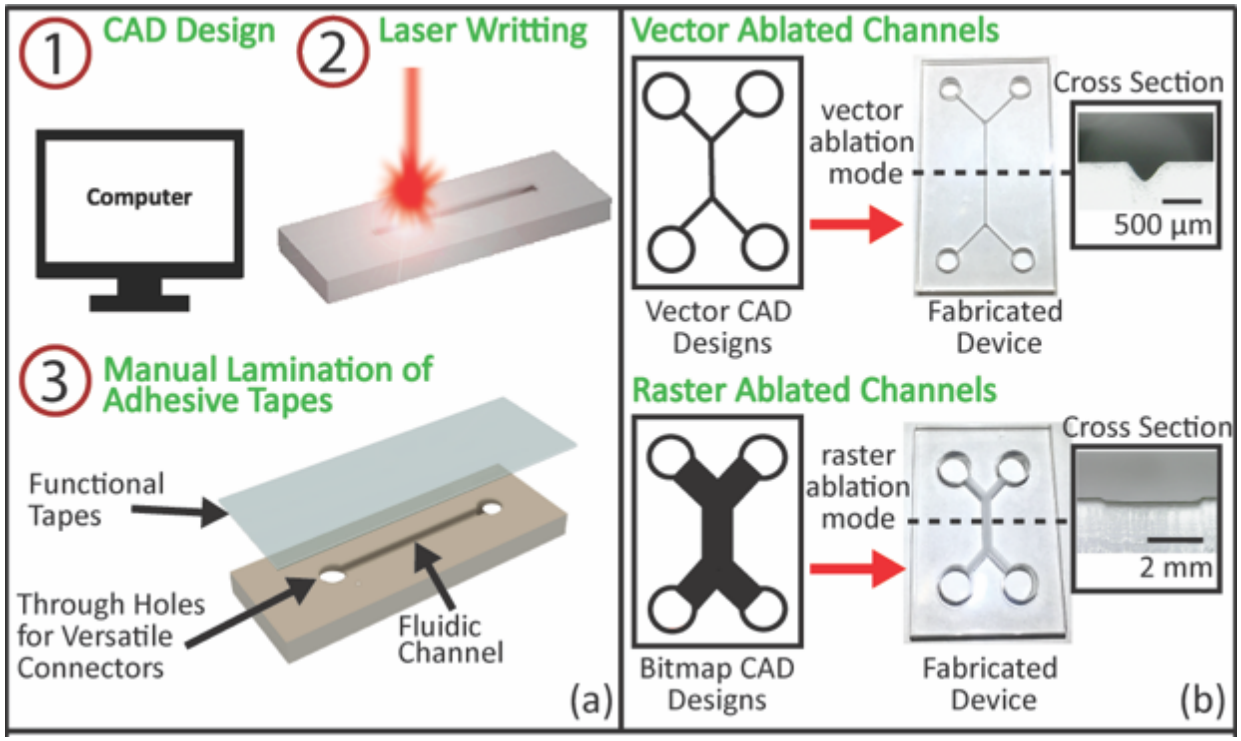

Figure 59 (a) Schematics of the fabrication process of the acrylic-tape hybrid microfluidic devices. (b) Fabricated devices by two different laser ablation modes: vector ablation (top) and raster ablation (bottom). The left column shows the CAD channel designs in the vector format (top) and the bitmap format (bottom). The right column shows the corresponding photos of the fabricated device and microscopic images of the channel cross-section. It is noted that the vector

ablated channel has a triangular cross-section (top) while the raster ablated channel has a rectangular cross-section (bottom).

Multiple devices can be fabricated in a single laser cutting process on one 12" X 24" acrylic board. The fabrication of 10 devices takes less than 30 minutes, and the results are highly reproducible. This straightforward three-step fabrication process allows rapid, controllable, and repeatable prototyping, which can greatly increase the efficiency of the iterative design process. It is noted that this fabrication method is based on laser ablation and limited to materials that can be ablated by lasers. Materials that are transparent at the CO_2 laser wavelength (around 10 μm) such as glass cannot be used.

There are two ablation modes in the laser cutter, namely the vector mode and the raster mode. The ablation modes are controlled by the formats of the CAD designs uploaded to the laser cutter as shown in Figure 59 (b). Each ablation mode has its own advantages and disadvantages, which will be detailed in the next paragraph. For the vector ablation mode, CAD designs are uploaded in the vector image format. In this mode, the laser cutter treats the CAD designs as continuous vector lines and continuously ablates these lines to form channels. For raster ablation mode, CAD designs are uploaded in the bitmap image format. In this mode, the laser cutter treats the CAD designs as discrete pixels and ablates all the pixel points with discrete laser pulses to form channels. Typical cross-sections of the channels fabricated by these two modes were shown in Figure 59 (b).

The roughness of the channels is determined by the laser cutter settings for both vector and raster ablation modes, while typically the vector mode ablated channels have smoother surfaces. As revealed by a recent study14, the roughness of the laser-cut channels ranges from 4 nm to 10 μm. A typical roughness of the vector mode ablated channels is 9.5 μm, as measured by a confocal microscope (LEXT OLS4000, Olympus). Although the roughness is not as good as that of the PDMS, the laser-ablated acrylic channels meet the needs of a wide range of applications, as proved by all the experimental results below in this paper. The widths of the channels fabricated by the vector and raster ablation modes are different. Vector mode ablated channel widths are determined by the laser spot diameter. In our case, the typical width of the channel opening is around 200 μm. By comparison, the raster mode ablated channels have a minimum width of around 450 μm, but the width can be much wider and not limited by the laser spot diameter. The two types of channels

are preferred in different applications. Vector ablated channels are used when smooth, small channels are preferred, such as in droplet generation applications. The raster ablated channels with wider cross-sections are preferred in point-of-care testing applications, where the wider cross-section channels make reading out the test results easier. We would like to note that strong optical scattering is caused by the relatively high roughness of the laser ablated channel surfaces. As a result, the transmission microscope images of these channels have limited resolution. However, the single-sided sealing tapes are optically clear and have a thickness of 50 ~ 150 μm, allowing for reflection microscope images with good quality to be readily taken from the tape side. All the experimental photos of the results below were taken from the tape side at the reflection imaging mode, if not specified otherwise.

The cost for fabricating acrylic microfluidic chips is low. For example, a 12" X 24" blank acrylic board costs less than $10, and a roll of single-sided tape costs around $2. From these materials, hundreds of acrylic microfluidic devices can be made even in the field, which leads to a material cost of less than $0.1 per device. In addition, after the tapes are peeled off, the acrylic substrate with channels could be thoroughly cleaned and sterilized for re-use, which further reduces the device cost, as well as the shipping and storage costs. The laser cutter is the most expensive equipment required for the fabrication. In this work, we used a professional laser cutter (VLS-4.60, Universal Laser Systems) simply because it is available. However, all the results should be repeatable by a regular laser cutter available on the market. It has been demonstrated that even a modified CD optical pickup head system can ablate micro-scale channels on acrylic boards [132]. In addition to the unique capabilities of the acrylic-tape devices, the decreasing cost and increasing accessibility of laser cutters in academia and industry make the platform even more appealing.

5.3 EXPERIMENTAL CHARACTERIZATION OF THE FLOW IN THE VECTOR ABLATED ACRYLIC CHANNELS

One important parameter of a microfluidic device is its characteristic length, which is directly related to the Reynolds number and the capillary action of the channel [133]. In our acrylic microfluidic devices, the Reynolds number is low (0.1-0.7) and the flow is laminar. Thus, a linear relationship is expected between the flow speed of capillary flow and the channel's characteristic

length. However, as discussed above in Section 2, our laser ablated acrylic channels have rougher surfaces than that of the conventional PDMS microfluidics, and this roughness could cause the flow behavior to differ from the expectation. As a result, it is important to experimentally determine the dependence of the flow on the characteristic length in the acrylic microfluidic channels.

For this purpose, we vector ablated acrylic channels with different heights, which resulted in different characteristic lengths. With a laser cutter, the height can be changed by using a different laser power with a fixed number of ablation passes or a different number of ablation passes with a fixed laser power. In both cases, the channel width on the top surface remains the same when the height is changed, because we focused the laser spot on the top acrylic surface before ablating the channels. In our experiment, we always changed the number of ablation passes with a fixed power to change the channel heights, as shown in Figure 60.

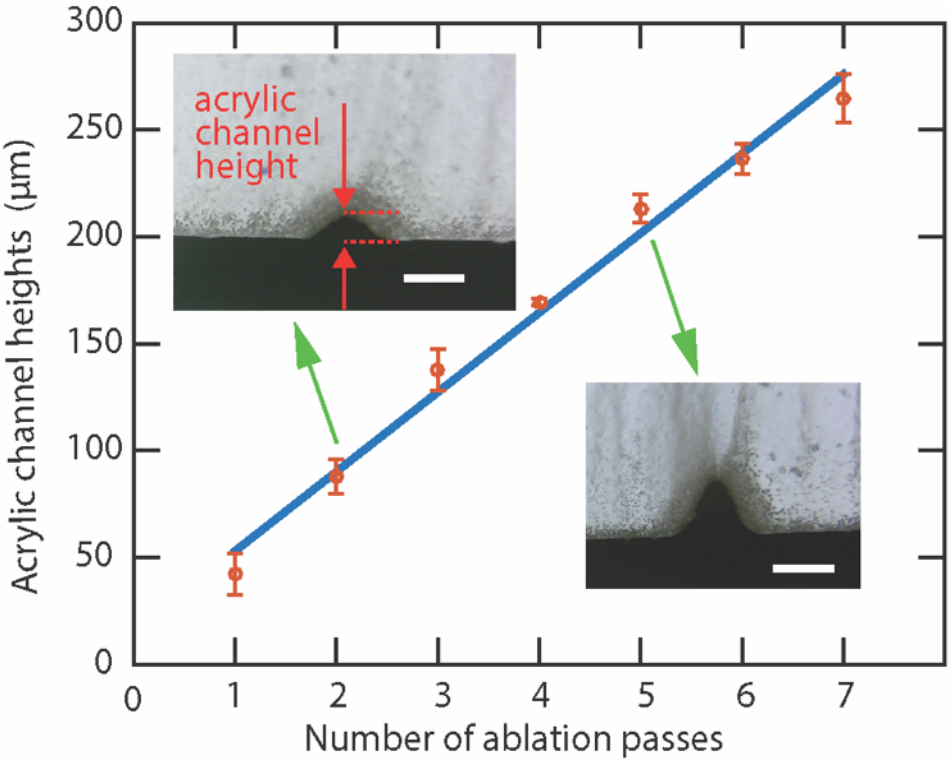

Figure 60 Measured heights of acrylic channels fabricated by different numbers of ablation passes. The red dots represent heights of channels fabricated by different numbers of ablation passes. The heights were measured from the microscope images of the channel cross-sections. (Insets) Two typical microscope images. The scale bars in both images are 200 μm. The blue linear regression line shows a linear relationship between the channel height and the number of ablation passes. The uncertainties are determined by the standard deviation obtained from 5 independent measurements on channels fabricated with the same number of ablations passes.

In the characterization experiment, we plasma-treated the acrylic channels to create hydrophilic acrylic surfaces and then sealed it with hydrophilic tapes (ARflow 93049, Adhesives Research). After applying the liquid to the inlet without an additional pressure, the capillary-force-driven flow was recorded by 1080p, 60 frame-per-second videos. We measured the time for the capillary-force-driven flow to pass through the channel and calculated the flow speed by the ratio of the channel length to the time. From the experiments, we found that the flow speed increased linearly with the channel height, as shown in Figure 61. This confirms the linear relationship between the flow speed and the channel's characteristic length, in this case, the channel height. This linear relationship in the experiment agrees with the capillary action and Hagen-Poiseuille theory [134]. Briefly, the capillary force (F_C) on the fluid inside the channel act as an equivalent hydro-pressure $\Delta P = F_c/A$ that drives the fluid flow. The pressure scales with channel height (H) as as $\Delta P \sim H^{-1}$. As a result, the flow speed (v) can be calculated by $v = Q/A$ and $Q = \Delta P/R$, where Q is the volumetric flow rate, A is the cross-section area that scales with H^2, and R is the hydraulic resistance that scales with H^{-4}. Therefore, the flow speed v scales linearly with H as $v \sim$ H. This experimental result confirms that the roughness of the laser ablated channel do not alter the flow behaviors that are expected from the theory. Such capillary action based microfluidic devices are desired in point-of-care applications for its active pump free, passively driven fluid flows.

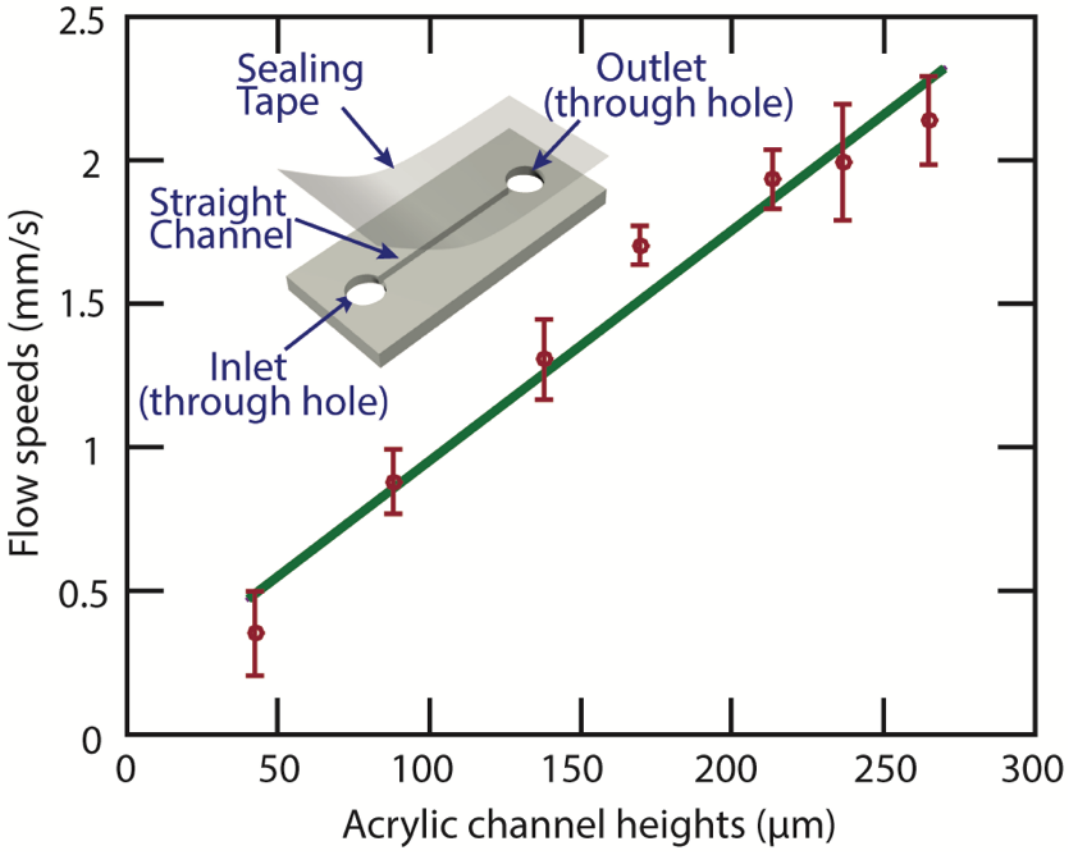

Figure 61 Flow speed characterization. The red dots represent the experimentally acquired flow speeds in channels with different heights. The green line is the linear fitting between the flow speed and the acrylic channel height. The inset schematic shows the acrylic device used for the characterization. The uncertainty of each data point was determined by the standard deviation obtained from 5 independent experiments with the same channel.

5.4 RECONFIGURABLE ACRYLIC-TAPE HYBRID MICROFLUIDIC DEVICES WITH MULTIPLEX FUNCTIONS

It is beneficial to reconfigure the functions of a microfluidic device without re-patterning the fluidic channels. This allows multiplexing of different functions on one single acrylic device with fixed channel patterns. These devices are appealing particularly for point-of-care applications, where the number of devices to realize multiple functions can be significantly reduced, saving cost on transportation and storage. However, most of the existing microfluidic devices are not reconfigurable. For example, most of the PDMS based devices that are plasma bonded can't be dissembled for reconfigurations. In paper microfluidics, functional chemicals or bio-markers [135]

are permanently coated onto the paper flow channels, making it difficult to reconfigure. By comparison, our acrylic-tape hybrid microfluidic platform can be reconfigured by changing the functional tapes, which can be done by an untrained person in the field, without requiring expensive equipment. The tape can be peeled off with minimum efforts for reconfigurations, and a new functional tape can be applied to the cleaned acrylic substrate, bestowing reconfigured, different functions on the same device. To showcase this capability, we demonstrate here reconfigurable, controlled flow actuation on an acrylic-tape microfluidic device.

Controlled flow actuation, especially delayed flow for sequential fluids delivery, is important in many applications [136-139]. We demonstrated different flow actuation mechanisms on a spiral microfluidic channel. As shown in Figure 62, in an acrylic channel sealed by a hydrophilic tape, once the green-dyed water was dropped into the inlet reservoir, it automatically wicked into the channel by capillary action. We peeled off the hydrophilic tape, cleaned the acrylic channels by rinsing them with isopropanol alcohol (IPA), and applied a hydrophobic tape on the channels to reconfigure the device. The green-dyed water applied to the inlet was confined in the inlet reservoir until a finger-press actuation. The results prove that we can switch the flow actuation mechanisms between passive capillary force driving and active finger actuation by changing the tapes.

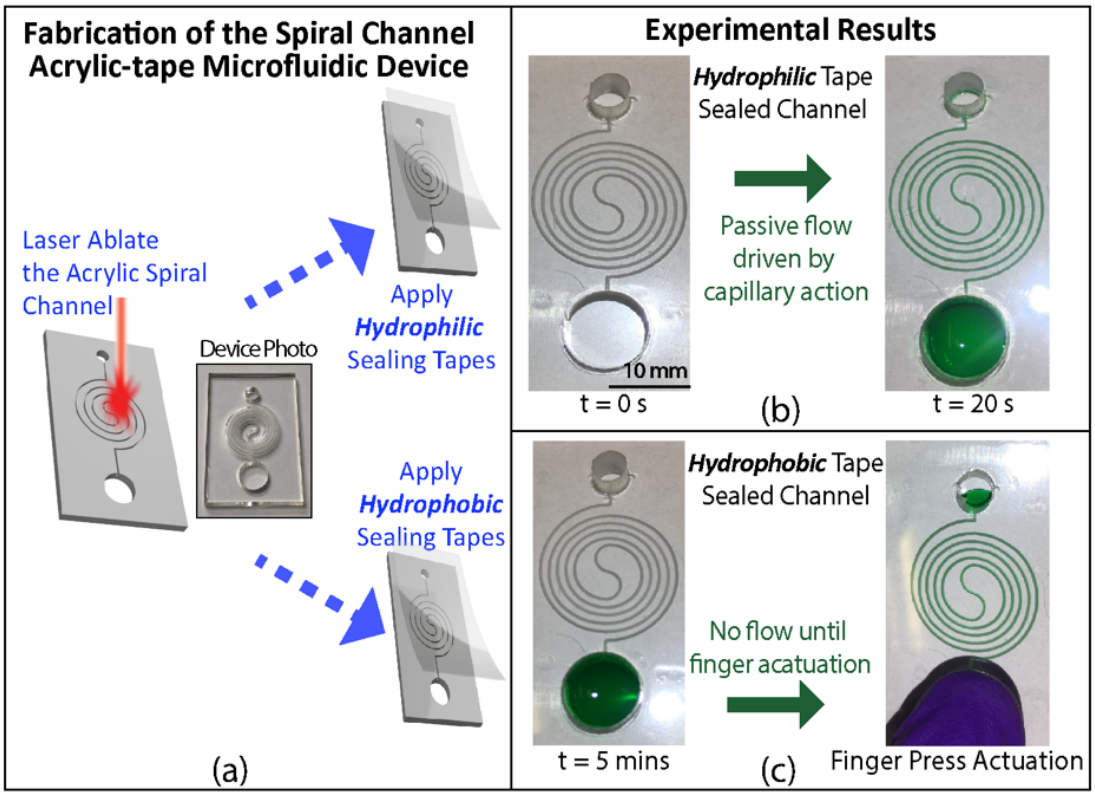

Figure 62 (a) Fabrication and assembly of the spiral channel acrylic microfluidic devices with reconfigurable flow actuation mechanisms. A spiral microfluidic channel is laser ablated onto an acrylic board. Either a hydrophilic or a hydrophobic tape is applied to seal the channel. (b) Automatic pump-free flow actuation with the spiral acrylic microfluidic channel sealed by a hydrophilic tape. Water with green dye was dropped into the inlet at t = 0. The whole channel was automatically filled due to the passive capillary action at t = 20s. (c) Finger-press flow actuation with the same spiral channel sealed by a hydrophobic tape. Water with green dye was dropped into the inlet at t = 0 and could not flow into the channel after 5 minutes because of the tape hydrophobicity, until actuated by a finger press on the inlet. The scale bar is 10 mm. The results in this figure were obtained with acrylic channels fabricated using the vector ablation method shown in Figure 1 and can be repeated with channels made by raster ablation (data not shown).

In addition to the flow actuation mechanism, we demonstrated reconfigurable flow pattern on a single acrylic microfluidic device. Specifically, as shown in Figure 63 (a-f), we used hydrophilic tapes with different hydrophobic patterns to realize different flow patterns in the same Y-shaped acrylic channel. When the hydrophobic stripe is on the top right channel (Figure 63 (b)), after the red dyed water was dropped into the inlet at the bottom of the Y-channel, water was immediately driven by the capillary force and automatically filled the top left channel. However, the water was stopped by the right channel's hydrophobic stripe, leaving the right channel dry.

When we used a different tape with a hydrophobic strip located at the top left channel, the flow pattern was reversed, as shown in Figure 63 (e). In both cases, all channels were filled right after a finger press was applied onto the inlet. The deformation of the tape resulting from the finger press generated additional hydraulic pressure that pushed the water through the hydrophobic stripes, as shown in Figure 63 (c) and (f). These results prove that we can reconfigure the flow patterns in the field, without fabricating a new device, making it potential to multiplex various functions on a single acrylic device.

In the abovementioned experiment, hydrophobic patterns can be created by selectively replacing hydrophilic glue with a hydrophobic coating on desired areas of the tape. The detailed experiment steps are explained below and shown in Figure 63 (g). First, a plastic film was laser cut to expose the desired patterns of the final hydrophobic areas. The cut film is applied on the sticky side of the hydrophilic tape, serving as a mask. The exposed hydrophilic glue on the tape was removed by rubbing a cotton swab soaked with IPA on the surface. Commercially available hydrophobic fluid (GRF135, Granger) was sprayed onto the masked tape to make the exposed area hydrophobic. With the plastic film mask removed, the hydrophilic tape can be applied to seal the acrylic channels with the hydrophobic patterns at the desired locations.

We note that acrylic-tape microfludics can be sterilized, especially before the devices are reconfigured. Commercially available pre-sterilized tapes (ARcare 8311, Adhesive Research) can

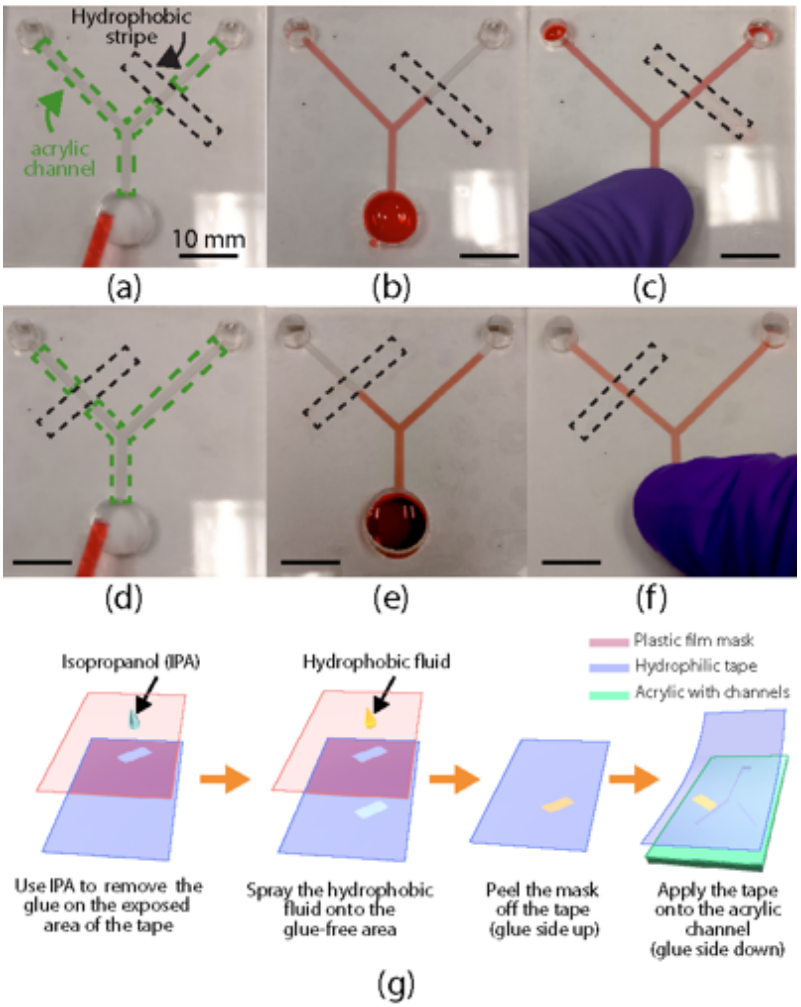

Figure 63 Reconfigurable acrylic microfluidics by functional tapes. (a-c) Flow patterns in a Y-shaped channel (the green dotted box) sealed by a hydrophilic tape with a hydrophobic stripe (black dotted box) on the top right channel. (d-f) Reconfigured flow patterns in the same Y-shaped channel sealed by a hydrophilic tape with a different hydrophobic stripe (the black dotted box) location. The flow patterns (a, d) before and (b, e) after the water was applied, and (c, f) after a finger press on the inlet (on the bottom of the Y channel). The fluid was water with red dye. All scale bars are 10 mm. (g) Schematics of the fabrication of a hydrophilic tape with a hydrophobic strip, as well as the application of the tape to an acrylic substrate with a Y-shaped channel.

be used. By removing the tape, channels in the used acrylic microfluidic devices are fully exposed and can be thoroughly cleaned or sterilized by solvents. We immersed the acrylic substrates with laser ablated channels in IPA and ethanol over 48 hours, and there was no crack observed, proving the solvent cleaning is safe to sterilize our acrylic substrates. We also note that the application of reconfigurable functional tapes is not limited to flow pattern controls. Other functional materials

can be patterned onto the tapes for interdisciplinary process control, such as the chemical catalyst for multi-step reactions and biomarkers for immunoassays. Furthermore, the tape coating process is suitable for mass production in industry, which is important for translating laboratory research to real-world applications.

5.5 ACRYLIC-TAPE MICROFLUIDIC DEVICES WITH ON-CHIP PUMPS

Control of continuous flow in microfluidics is important for both laboratory experiments and in-the-field testing. For example, in microfluidic H-filter applications [140], a controlled continuous flow is required for maintaining the two-phase flow boundary and transportation of the filtered substances. While conventional syringe pump systems can provide more accurate flow control, their relatively large sizes and the requirement of an AC supply can compromise their usability in the field. Especially when only moderate flow control is required, microfluidic devices with on-chip pumps are preferred. In this section, we demonstrate two on-chip pump designs that are compatible with the acrylic-tape hybrid microfluidic devices. In both demonstrations, the acrylic channels were fabricated using the raster ablation method, which is shown in Figure 58 and detailed in Section 2.

5.5.1 On-chip paper pump

Paper is lightweight and low-cost, and their porous structures have excellent wicking properties to provide continuous flow for a relatively long time (~60s). We applied paper pumps, which was demonstrated previously in PDMS microfluidics29, in our acrylic-tape devices. We inserted two pieces of Whatman filter paper into the two outlets of an acrylic H-channel, respectively, as shown in Figure 64 (a). One of the inlets was filled with red-dyed deionized water (DI water), and the other inlet was filled with green-dyed DI water. The fluid was first driven by the capillary force to fill the channel and wicked into the papers at the outlets, until the paper was fully soaked with the fluid. The hydraulic pressure provided by the wicking paper was controlled by the paper's cross-section area. Two paper pumps with the same cross-sections provided equal hydraulic pressures at the two outlets of the H-channel. Thanks to this constant and continuous driving pressure, the two-phase flow maintained a stable boundary in between, as can be clearly seen in the inset of Figure

64 (a). Besides providing constant hydraulic pressure, paper pumps with carefully designed cross-sections can also provide various functions, as demonstrated in previous work [139].

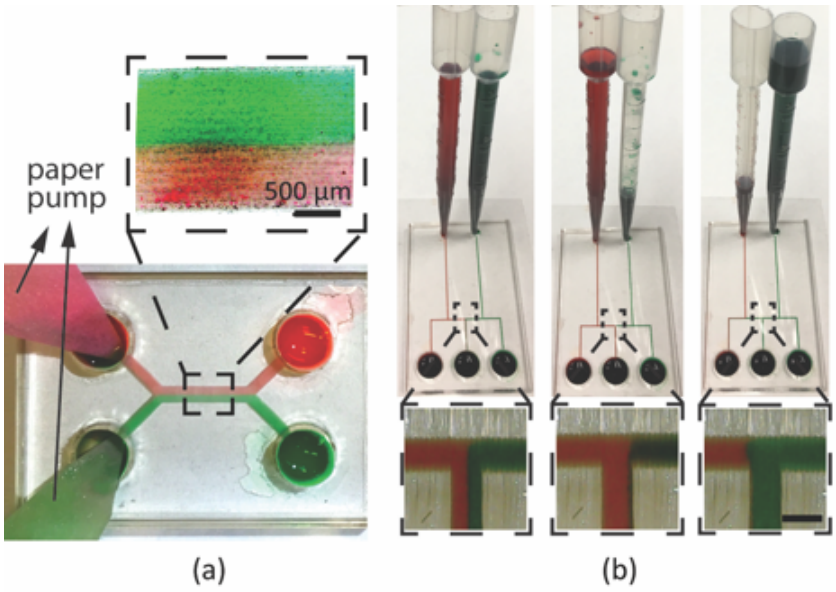

Figure 64 Experiment results of (a) on-chip paper pumps and (b) on-chip pipette tube pumps. The channel in (a) has a width of around 2 mm, and a height of around 200 μm. The inset in (a) shows a microscope image of the two-phase laminar flow in the channel. The channels in (b) have a width of around 500 μm, and a height of around 200 μm. The insets in (b) show the microscope images of the middle channel, where the output fluid was controlled in real time by the pumps. Scale bars in all the insets are 500 μm.

5.5.2 On-chip pipette tube pump.

For applications that require flow durations longer than one minute, we used on-chip pipette tube pumps to drive the flow in acrylic microfluidic devices. The diameters of the rigid acrylic inlets of the microfluidic channels are designed to be slightly smaller than the outer diameters of the deformable pipette tips. As a result, the interference fit ensured fluid-tight sealing between the pipette tips and the acrylic inlets. The fluid height in a pipette was around 15 cm with a fluid volume of around 5 ml. A continuous flow in the channels was realized by the hydrostatic pressure at the inlet for more than 30 minutes. The hydraulic pressure can be easily adjusted on the fly by controlling the fluid height in each pipette.

Figure 61 (b) shows the experimental results of a microfluidic chip with two on-chip pipette tube pumps. The output fluid of the middle channel can be switched in real time by controlling the

input pressure from the pipette pump. At first, the red and green dyed water was kept at the same heights in the pipettes to realize a balanced hydraulic pressure input. As a result, the red-green water interface is located at the center of the middle output channel, resulting in the same volume ratio of red and green dyed water in the middle outlet, as shown in the left column of Figure 61 (b). When green-dyed water was drawn out from the pipette to lower its hydraulic pressure, the red-green water interface shifted to the right of the middle channel, as shown in the middle column of Figure 61 (b). As a result, only red fluid was output from the middle channel. Similarly, when the green pipette has a higher water level, the red-green interface shifted to the left of the middle channel, resulting in only green fluid output from the middle outlet, as shown in the right column of Figure 61 (b). A complete switch from red to green water at the middle outlet required about 1~2 seconds.

5.6 SYRINGE PUMP DRIVEN MONODISPERSE DROPLET GENERATION

In addition to on-chip pumps that are preferred for point-of-care applications, traditional syringe pump systems are also readily compatible with the acrylic-tape hybrid devices. Syringe pumps are preferred for applications where well-controlled flow speeds are important while the portability is not a concern.

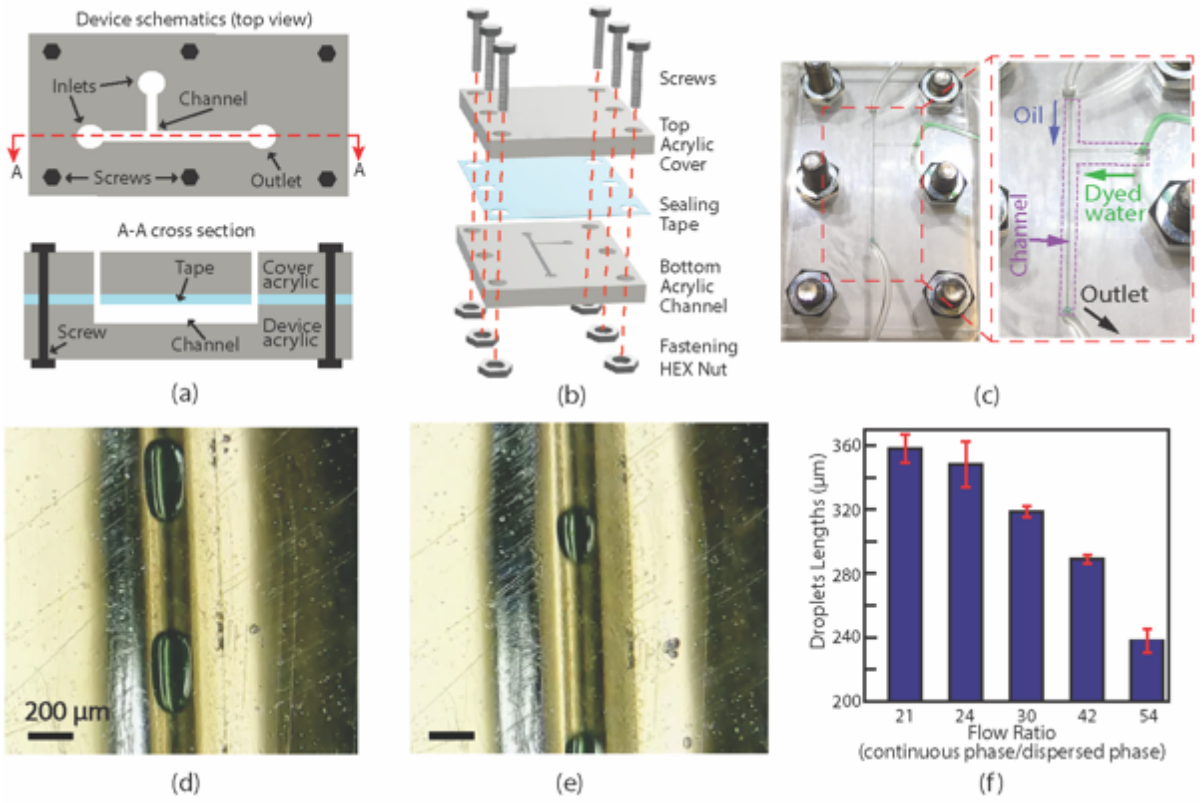

Figure 65 (a) 2D schematics of a T-channel acrylic-tape microfluidic device for monodisperse droplet generation. The channels were fabricated using the vector ablation method shown in Figure 1. (b) An exploded-view showing the assembly of the device. (c) Photos of an assembled acrylic-tape microfluidic device. The arrows in the zoomed-in (right) photo show flow directions from the inlets and outlet inside the T-shaped channel, while the channel is highlighted by a purple dotted box. (d) and (e) are microscopic images showing two typical monodisperse droplets generated at volumetric flow ratios (continuous phase flow over dispersed phase flow) of 30 and 54, respectively. The scale bars are 200 μm. (f) Experimentally measured droplet lengths at different ratios of continuous to dispersed phase flow speeds. The uncertainty of each data point is determined by the standard deviation obtained from 5 independent measurements on the droplets generated with the same flow ratio.

Monodisperse droplet generation is an important application in microfluidics. It requires a continuous phase flow with a relatively high speed to squeeze and break off the dispersed phase fluid into droplets. To generate droplets with consistent geometries, a well-controlled and maintained flow ratio between the dispersed phase and the continuous phase is required. Here, we demonstrated droplet generation on an acrylic-tape hybrid microfluidic device and characterized the dependence of the droplet size on the flow rate. The channel design, assembly schematic, and the photos of an assembled device are shown in Figure 65 (a-c), respectively. A T-junction microfluidic channel design was chosen for droplet generation. To ensure a high flow rate without

a concern of tape leakage, the tape sealed channel layer was sandwiched by two acrylic boards which are clamped with screws.

Microscope images of the generated droplets with different diameters are shown in Figure 65 (d) and (e). The fluid in the droplets was green-dyed deionized water, the continuous phase medium was vacuum pump oil (Vacuum Pump Oil No. 19, VWR). Droplets with different lengths were consistently generated by a fixed disperse phase flow rate of 1.667 μl/min and various continuous phase flow rates from 35 to 90 μl/min. Droplet generation at a frequency of 7 Hz was demonstrated with a coefficient of variation (CV) of the droplet length as low as 4%. The CV is defined as the standard variation of the generated droplet lengths normalized by the average length. The characterization results of droplet lengths at different flow rates are shown in bar charts in Figure 65 (f), and the droplet widths were always the same with the channel width.

In addition to the droplet generation, the functional tape sealed acrylic-tape devices can potentially enable droplet manipulation if proper tapes are used. For example, electric-field-based droplet manipulation30 requires materials that can withstand high voltages, and the electrical tapes (Super 88 Vinyl Electrical Tape, 3M) with 10 kV breakdown voltages are suitable for these applications. In magnetic-field-based droplet manipulation, magnetic tapes (Flexible Magnet Tape, 3M) can be used to support magnetic fields in the fluid channels. Furthermore, all the above-mentioned special tapes are commercially available, which is beneficial to decrease the cost and to increase the accessibility of the acrylic-tape microfluidic devices.

5.7 PRELIMINARY EXPERIMENTAL RESULTS OF INTEGRATION WITH LMR D-SHAPE OPTICAL FIBER SENSORS (AND FUTURE PLANS)

Thanks to the tape-based sealing method, optical fibers can be easily integrated with the acrylic-tape microfluidic devices. Before the tape is applied, a fiber can be inserted into a channel from the open top and the fiber position can be precisely adjusted. By comparison, in the commonly used PDMS microfluidic channels, the optical fiber has to be inserted after the channels are sealed between the PDMS and glass substrates. The position control of the fiber, especially in the lateral direction, in such closely sealed channels is difficult, if not impossible.

The optical fiber integrated acrylic-tape microfluidic devices enjoy the advantages of both the microfluidic platform and the optical fibers. Specifically, for sensing applications, such devices

combine the high sensitivity (optical fiber sensors) and the high-throughput fluidic manipulation (microfluidic device) in a highly portable way, which can allow enhanced sensing capabilities in applications such as point-of-care diagnosis.

Preliminary results of such integrations were experimentally demonstrated. As shown in the device schematic in Figure 66 (a), the acrylic device has two channels that are arranged in a T-shape, one for fluidic flow, another for D-shape fiber senor. Figure 66 (b) shows the photo of the fabricated acrylic microfluidic device with a D-shape fiber sensor embedded. To investigate whether the integration of optical fiber will affect the fluidic flow in the device, particularly, whether there will

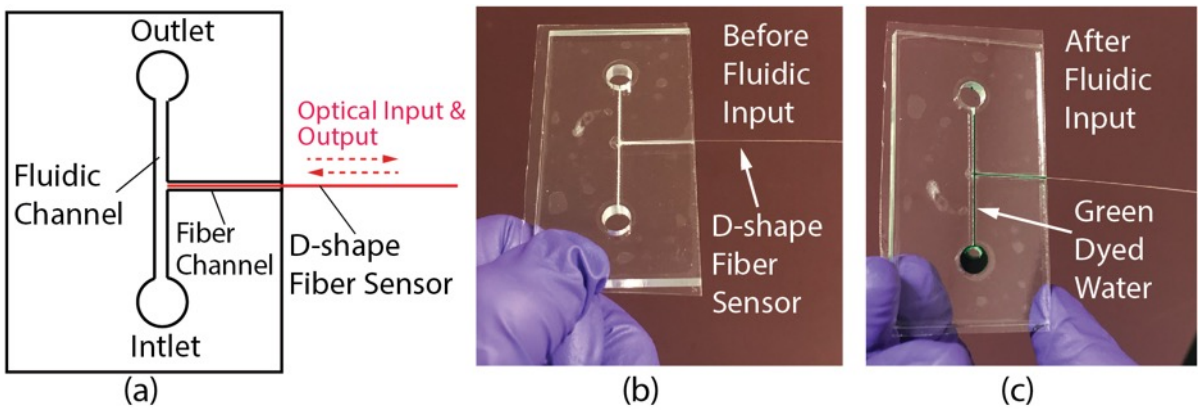

Figure 66 (a) Schematic of the optical fiber integrated acrylic-tape microfluidic device. (b) and (c) photos showing before and after input fluid (green dyed water) into the device.

be fluidic leakage close to the fiber channel, fluidic flow in the channel were experimentally characterized. As shown Figure 66 (c), right after a small volume of green dyed water was applied to the fluidic inlet, the fluid was automatically pumped into the channels due to the capillary force (detailed in section 5.3). The passive fluid pumping requires only a small amount of fluid and no additional energy cost. The fluid-filled fiber channel can allow the D-shape fiber with a specific coating material to sense the substance of interest in the fluid. For example, if the D-shape fiber sensor is coated with a specific type of antigens, when the corresponding antibodies in the fluid are attached to these antigens, the resulting refractive index change will change the optical signal and allow the sensor to detect the presence of the antibodies. Such detection capabilities are valuable to point-of-care applications. It is noted that, as to date, due to the limited time, no sensing signal has been experimentally acquired from the devices yet, more research in this direction is

required in the future. In order to realize the full potential of the optical fiber integrated acrylic-tape microfluidic devices, some of the important future works are listed below:

1) Develop effectively chemical or bio-chemical coating technic to functionalize the D-shape fiber sensor (e.g. antigen coating).
2) Improve the stability of the relative position of the D-shape fiber sensor in the channel to prevent the sensing surface touching the sealing tape.
3) Develop more sophisticated acrylic-tape microfluidic devices that can also take advantages of the unique reconfigurable functional sealing tapes for the sensing.

5.8 SUMMARY

In this chapter, a low-cost and versatile acrylic-tape hybrid microfluidic platform is developed. Different from that of PDMS microfluidics, the fabrication process is rapid, straightforward, and does not require clean-room access or plasma bonding, which makes the acrylic-tape microfluidics readily translatable to industrial mass production. The tape-based reversible sealing mechanism is reliable for long-term applications and allows reconfiguration of device functions to be carried out in the field. We experimentally characterized the dependence of the capillary flow speed on channel geometric parameters. We demonstrated reconfigurable functions by changing functional tapes on the same microfluidic device, thanks to the reversible sealing and multiple flow mechanisms enabled by different tapes. This result indicates the potential of function multiplexing on a single acrylic-tape microfluidic device and the ability of changing the device functions in the field. Different pumping mechanisms have been investigated for the acrylic-tape platform. To reduce device footprints for point-of-care applications, two types of on-chip pumps, namely paper pumps and pipette tube pumps, have been used to demonstrate reliable and adjustable two-phase flow. In addition, repeatable and controllable droplet generation was demonstrated with syringe pumps. The ability to reconfigure and multiplex functions on a single device, augmented by its immediate compatibility with both on-chip pumps and syringe pumps, makes the acrylic-tape hybrid microfluidics a versatile platform with great potential for in-the-field applications such as biomedical testing and point-of-care diagnosis. Preliminary results of D-shape fiber sensor integration was experimentally demonstrated using a T-shape channel. Our future work will be focused on the integration of multiple functions across disciplines, including surface chemistry,

electrochemistry, biology, and fiber optics, by leveraging the adaptive and versatile nature of the acrylic-tape platform.

Chapter 6 SUMMARY AND FUTURE WORK

6.1 SUMMARY AND CONTRIBUTIONS OF THE DISSERTATION WORK

Specially shaped optical fibers that can not only efficiently transmit light but also allow the guided light to interact with the matters around it have found a wide range of applications both in engineering [9, 34, 75] and in fundamental science research [9, 10, 49, 85]. In the near future, with the quickly advancing nano/micro-fabrication technologies and the emerging trends of uniting electronics with photonics, it is certain that special-shape optical fibers will find more applications and have a strong impact to both the research community and the society as a whole.

While the impressive capabilities of the special-shape optical fibers have already been widely demonstrated, they are far from perfect. Due to the lack of understanding of the optical properties of specially shape fibers, only a limited number of specially shaped fiber designs have been demonstrated. These designs did not fully exploit the capabilities of the specially shaped fibers. In addition, the poor controllability and repeatability of the fabrication methods have limited the advancement of the specially shaped fibers.

This doctoral research aims to solve the abovementioned limitations of the special-shape fibers, with the objectives of achieving fundamental understanding, improving the fabrication methods to allow a repeatable and controllable fabrication of novel specially shaped fiber designs for different applications, and developing a new microfluidic platform that can allow special-shape optical fibers to be integrated with the microfluidic devices in a straightforward way. Based on the research work described in the previous chapters, the contributions of this dissertation work are summarized as follows**:**

Contribution 1: An enhanced fiber tapering system for highly repeatable adiabatic tapered fiber fabrications.

An enhanced fiber tapering system have been developed with innovations both in hardware and monitoring method. The innovation in hardware is the ceramic housed electric furnace (CHEF). The CHEF has a low cost and is highly accessible. The CHEF allows fabrication of high-transmission adiabatic tapered fibers in highly repeatable way. *To the best of the author's knowledge, this is the first time that a customized low-cost ceramic-based electric heat source that can allow adiabatic fiber tapering has been demonstrated.*

The innovative monitoring method is based on the frequency-domain optical transmission signal from the fiber that is being tapered has been developed. *To the best of the author's knowledge, this is the first time that a frequency-domain fiber tapering monitoring method has been developed.* Compare to the widely used time-domain monitoring method, *this monitoring method can reliably determine whether the tapered fiber has achieved single-mode state,* which is critical for the fabrication of high quality tapered fibers. The enhanced fiber tapering system can allow a wider audience to access the high-quality adiabatic tapered fibers and apply it in a wide range of applications.

Contribution 2: Lossy mode resonance (LMR) sensor enabled by SnO_2 coating on a novel specially shaped fiber design has been developed.

The developed LMR sensor has a D-shape fiber tip, *to the best of the author's knowledge, this is the first time that a fiber-tip form factor has been introduced to the D-shape fiber lossy mode resonance sensors.* The SnO_2 coating has endowed the sensor with the capability of relative humidity and moisture sensing. *This is also the first time that a D-shape fiber lossy mode resonance sensor has been used for relative humidity/moisture sensing.* The fiber-tip form factor can allow the sensor to be used like a probe and be inserted into/removed from a tight space. Such capability can create various new use case for the sensor, in fact, *collaborators from the industry has already took steps in creating a utility patent for this novel sensor*.

Contribution 3: Specially shaped tapered fibers with novel designs have been developed for integrated photonic and microfluidic applications.

Two novel specially tapered fibers, the tapered fiber loop and the tapered fiber helix have been developed. The tapered fiber loop is a type of ring resonator, while ring resonators that also have the name of tapered fiber loop have been demonstrated before, the tapered fiber loop developed in this work has two superiority that differentiated itself from them: 1) the mechanical stability of the tapered fiber loop in this work is significantly better. 2) the tapered fiber loops in this work can achieve a diameter as small as 15 μm while still have a high intrinsic optical quality factor of 32,500. *In fact, neither 1) nor 2) has been demonstrated before*. Tapered fiber developed in this work that possesses both 1) and 2) can potentially be used in various sensing applications.

The tapered fiber helix has a 3D structure that allows it to efficiently deliver light to locations out of the plane defined by its two regular fiber arms. One application of the tapered fiber helix is integrated photonic device characterizations. The outmost protruded part of the helix can

couple light to an in-plane integrated photonic device through near-field optical coupling. *This is the first time that a helical geometry has been demonstrated on a tapered fiber. More importantly, the straightforward fabrication method of the tapered fiber helix will allow a wider audience to use this tool to probe integrated photonic devices.*

Other than being used as an optical probe for integrated photonic device characterizations, the tapered fiber helix can also be used for micro-particle manipulations. Different from micro-particle manipulations done by a straight tapered fiber taper, the helical geometry allows optical transportation of microscale particles along more complex, three-dimensional trajectories. *To the best of the author's knowledge, this is the first time that a three-dimensional micro-particle manipulation using a tapered fiber has been demonstrated.* In a stationary fluidic environment, the fiber helix can be used to selectively approach, trap, and propel a particular particle lying on the substrate from a group of particles, which is challenging for straight tapered optical fibers. In a microfluidic channel, the fiber helix can be used to pre-focus particles to the center of the channel, as they pass through the channel. The three-dimensional shape of the fiber helix allows for much more efficient particle focusing than straight fiber tapers. This pre-focusing is important for effective subsequent optical detection or interrogation, such as flow cytometry and cell stiffness measurements in optical stretchers.

Contribution 4: Developed an acrylic-tape hybrid microfluidic platform that can allow function reconfiguration and optical fiber integration.

A low-cost, versatile microfluidic platform based on reconfigurable acrylic-tape hybrid microfluidic devices has been developed. The acrylic-tape hybrid device is fabricated by laser cutting microfluidic channels on an acrylic board, and then seal the channels with a functional tape. The fabrication processes are rapid, straightforward, and translatable to industrial mass productions. *To the best of the author's knowledge, this is the first time that the fabrication method of sealing the acrylic channel with a reconfigurable functional tape has been demonstrated.* The functional tapes can allow the function of the microfluidic devices be reconfigured without repatterning the fluidic channels. The reconfigurable feature made the acrylic-tape hybrid devices particularly appealing to point-of-care applications, where the number of devices required to realize multiple functions can be significantly reduced, saving cost on transportation and storage. Furthermore, the tape-sealing method is compatible with special-shape fiber integrations. After inserting the optical fiber into the acrylic channel, one can directly apply the sealing tape to seal

the channel without worrying that the sealing process might cause damage to the fiber or misalign the fiber within the channel.

6.2 FUTURE WORK

The capabilities of the specially shaped fibers are far from being fully exploited. However, the highly accessible special-shape fiber fabrication methods and the enhanced special-shape fiber designs developed in this dissertation work has provided a foundation for using the special-shape fibers in a wide range of applications. To further improve the specially shaped fibers, specifically the tapered fiber loos, helices, and the D-shape fibers, the suggested future work is summarized as follows:

i. Suggestions to improve the mechanical robustness of the tapered-fiber-loop sensors.
   The high optical quality factor of the tapered fiber loop, made it a promising sensor for various sensing applications. However, while the circular structure of the loop is mechanically stable and won't unwrap even under strong air flows, the tapered fiber itself is relatively weak (remember that it is a ~ 1 μm glass wire) and may be broken by the flow disturbance in a real-world environment. Furthermore, any contaminations stuck onto the tapered fiber will cause huge optical scattering loss can result in the failure of tapered-fiber-loop sensor. In order to solve these problems, one solution is to develop a packaging for the tapered-fiber-loop sensors. For example, a tapered fiber loop can be inserted into a high stiffness tube, and the two regular fiber arms of the tapered fiber loop can be fixed onto the tube wall using glues. This way the tapered fiber loop will be protected from strong air flow disturbance and environmental contaminations. However, it remains a question that how one can allow the tapered fiber to sense the environment while being enclosed in a package.

ii. Integrate the tapered fiber helix with the microfluidic device.
   As we have previously mentioned, tapered fiber helix can manipulate micro-particles in three dimensions, which is beneficial for microfluidic applications such as particle sorting and flow cytometry. However, due to the limited time and immature device design,

integrating tapered fiber helix with microfluidic devices has not been achieved yet. An improved microfluidic device design to allow such integration is suggested in future work.

iii. Suggestions to overcome the limitations of the ceramic housed electric furnace (CHEF).
One of the CHEF's limitations is its relatively short lifetime (~ 3 months). The short lifetime is mainly due to the oxidation of the heating wire. When certain part of the wire is fully oxidized, the wire will break, and the CHEF will stop working. One possible solution to this problem is to put the CHEF-based fiber tapering setup in a chamber with nitrogen-purging, so that the oxidation process of the electric wire can be slowed down.

The manual fabrication process of the heating coil may cause non-uniform coil spacings, which may result in non-uniform temperature distribution and affect the tapered fiber quality. One possible solution to this problem is to replace the manual coil fabrication process with an automated coil fabrication process that can accurately control the spacing between each coil.

iv. Suggestions to overcome the limitations of the lossy-mode-resonance D-shape fiber sensor
The current side-polishing setup for the D-shape fiber is based on an aluminum rod wrapped with a polishing paper. However, it is difficult to cut a polishing paper whose length is exactly the same with the circumference of the aluminum rod. As a result, there will be either an overlapped area or a gap introduced after wrapping the polishing paper around the rod. This may affect the polishing surface roughness of the D-shape fiber. It is suggested to look for a monolithic polishing rod whose surface can be directly used for the fiber polishing.

Currently, some of the fabricated lossy-mode-resonance D-shape fiber sensors have a relatively large FWHM and low sensitivity. It is not clear what is that cause for these problems. It is suggested to use FDTD simulation to study the lossy mode resonance phenomenon. The FDTD simulation can facilitate the investigation of the optical mode coupling between the optical fiber and the film coating and can provide simulated

transmission signals of different sensor designs. These enhanced fundamental understanding will help to better understand the lossy-mode-resonance signal.

v. Fully characterize the D-shape fiber relative humidity sensor.
As we have mentioned in Chapter 5, the lossy-mode-resonance D-shape fiber relative humidity sensor is an on-going project. Due to the limited time, the sensor has not been fully characterized yet. It is suggested to carry out a full characterization of the sensor in the future, including characterization of its sensitivity, response time, resolution, relative humidity sensing range, and temperature dependence.

vi. Package the D-shape fiber-tip sensor.
The polished tip of the D-shape fiber-tip sensor is fragile. However, in many applications it is desired that the sensor tip can be inserted or embedded into a relatively hard material (e.g. cookies, chips). In order to improve the mechanical strength of the sensor, a packaging for the sensor, especially for the tip area, is suggested in the future work.

6.3 SOCIAL IMPACT OF THIS DISSERTATION WORK

Other than being useful to the academic research community, the four thrusts of this dissertation work, namely, 1) fiber tapering system development, 2) special-shape tapered fibers development, 3) D-shape fiber sensor development, and 4) development of microfluidic platform that is compatible with optical fiber integrations, can all potentially bring positive impact to the society. Their impacts are summarized in the following:

6.3.1 Tapered fibers.

Cost reduction for the fiber tapering system.

In Chapter 3, we introduced a low-cost, customized heat source for the fiber tapering called the ceramic housed electric furnace (CHEF). The monetary cost for one CHEF is less than $5, the time cost for fabricating one CHEF is around 5 minutes (manual fabrication by a student). In comparison, the two commercially available ceramic heat sources that have a similar fiber tapering performance with the CHEF have a much higher cost, both in terms of money and time. The

ceramic heat source from MHI has a price of $20600 and need a lead time of 8 to 12 weeks; the ceramic heat source from NTT-AT has a lower price of $2500 but it needs a longer lead time of 4 to 6 months. *As a result, the CHEF can potentially reduce the cost of accessing high-quality tapered fibers for the masses.*

On-the-fly optical probe for on-wafer integrated photonic testing

One appealing feature of the tapered-fiber-helix-based optical probe introduced in Chapter 2 is that it can selectively characterize integrated photonic devices on a whole wafer on the fly, without having to modify or adding additional components to the devices. Optical probes with such characterization capabilities are highly desired by the integrated photonic industries. In fact, probe stations with similar functionalities, but for electronic devices, have proven to be a useful and important tool in the semiconductor industry. *Since the tapered-fiber-helix-based optical probes have a miniaturized size, it can potentially be integrated onto an electronic device probe station and endowing it with optical probing capabilities. These enhanced probe stations with optical probing capabilities will greatly facilitate the development of the integrated photonic industry.*

Education

The tapered fibers developed in this work have a miniaturized size and are highly portable. After the fabrication they can be mounted to a stiff mechanical holder. These mounted tapered fiber devices can be moved around with hands and do not require any further alignment. They can potentially be used in the K-12 education. The tapered fiber loops can demonstrate the phenomenon of optical ring resonators; the tapered fiber helix can demonstrate three dimensional optical microparticle manipulations. *These experiments would inspire students' interests in further understanding of the fundamental physics behind them. This educational purpose of tapered fibers will benefit both students and teachers.*

6.3.2 D-shape fibers

Impact of the D-shape fiber relative humidity and moisture content sensor in the food industry

The D-shape fiber relative humidity and moisture sensor introduced in Chapter 4 has an imminent impact in the food industry. The sensor can potentially be used to track moisture loss in a food or relative humidity drop in a harsh environment such as an oven. *The D-shape fiber sensors can enable real-time, high-sensitivity, and high accuracy relative humidity/moisture measurements,*

which can be a huge labor and cost savings on a food production line. This is because, quite often, companies start up an oven and have to take samples of finished product for moisture testing. They have to throw away product until the moisture is below a certain level. If this could be done in real time, it would go a long way to automating the start-up process and allowing feedback oven control without human intervention.

The D-shape fiber relative humidity/moisture content sensor is even potentially a game changing technology for food companies needing start-up help, online monitoring, and feedback control and monitoring. In fact, a provisional patent has already been filed for using this sensor to measure moisture in wet, porous food samples. And two companies have showed great interest in buying the patent.

Impact of the D-shape fiber sensor in health-care applications

Other than measuring relative humidity and moisture, by changing or modifying the coating material, the lossy-mode-resonance-based D-shape fiber sensors can also be potentially used to measure biochemical substances such as antigens. In many health-care applications, the diagnosis relies on the measurements of biochemical substances in body fluids. *The high sensitivities of the lossy-mode-resonance D-shape fiber sensors can potentially improve the detection limits of these biochemical-substance-related measurements, and hence can potentially improve the accuracy of the diagnosis in different health-care applications.*

6.3.3 Acrylic-tape hybrid microfluidic platform.

Point-of-care applications

Both the special-shape tapered fibers and the D-shape fibers developed in this dissertation are small in size, and thus have great potentials to be integrated to microfluidic devices for point-of-care applications. Thanks to the unique functional-tape-based sealing method, the acrylic-tape hybrid microfluidic platform developed in Chapter 5 can potentially facilitate such integrations. *Integrating special-shape optical fibers with the acrylic-tape microfluidic devices can potentially lead to a new type of point-of-care device that is portable, low-cost and has ultra-high sensitivity.*

REFERENCES:

1. "Fiber Optics 2019 Global Market Net Worth Research Report" (WiseGuyReports.Com)

2. M. C. Frawley, A. Petcu-Colan, V. Truong, and S. Chormaic, "Higher order mode propagation in an optical nanofiber," Optics Communications 285, 4648 (2012).

3. F. Xu, P. Horak, and G. Brambilla, "Optical microfiber coil resonator refractometric sensor," Opt Express 15, 7888 (2007).

4. H. Latifi, M. I. Zibaii, S. M. Hosseini, and P. Jorge, "Nonadiabatic tapered optical fiber for biosensor applications," Photonic Sensors 2, 340–356 (2012).

5. H. Xin, Y. Li, L. Li, R. Xu, and B. Li, "Optofluidic manipulation of Escherichia coli in a microfluidic channel using an abruptly tapered optical fiber," Applied Physics Letters 103, 033703 (2013).

6. H. Bae, X. Zhang, H. Liu, and M. Yu, "Miniature surface-mountable Fabry-Perot pressure sensor constructed with a 45 degrees angled fiber.," Optics letters 35, 1701–3 (2010).

7. W. Talataisong, R. Ismaeel, and G. Brambilla, "A Review of Microfiber-Based Temperature Sensors," Sensors 18, 461 (2018).

8. metsky, Y. Dulashko, and A. Hale, "Fabrication and study of bent and coiled free silica nanowires: Self-coupling microloop optical interferometer," Opt Express 12, 3521 (2004).

9. B. D. Hauer, P. H. Kim, C. Doolin, A. J. MacDonald, H. Ramp, and J. P. Davis, "On-chip cavity optomechanical coupling," EPJ Techniques and Instrumentation 1, (2014).

10. C. Michael, M. Borselli, T. Johnson, C. Chrystal, and O. Painter, "An optical fiber-taper probe for wafer-scale microphotonic device characterization," Opt Express 15, 4745 (2007).

11. J. Shin, M.-S. Yoon, and Y.-G. Han, "Relative Humidity Sensor Based on an Optical Microfiber Knot Resonator With a Polyvinyl Alcohol Overlay," Journal of Lightwave Technology 34, 4511–4515 (2015).

12. H. Yu, L. Xiong, Z. Chen, Q. Li, X. Yi, Y. Ding, F. Wang, H. Lv, and Y. Ding, "Solution concentration and refractive index sensing based on polymer microfiber knot resonator," Applied Physics Express 7, 022501 (2014).

13. F. Xu, P. Horak, and G. Brambilla, "Conical and biconical ultra-high-Q optical-fiber nanowire microcoil resonator," Applied Optics 46, 570 (2007).

14. M. Sumetsky, "Optical fiber microcoil resonators.," Optics express 12, 2303–16 (2004).

15. K. Okamoto, "Fundamentals of Optical Waveguides (Second Edition)," xv–xvi (2006).

16. T. A. Birks and Y. W. Li, "The shape of fiber tapers," Journal of Lightwave Technology 10, 432–438 (1992).

17. T. Kippenberg, O. Painter, K. Vahala, and S. Spillane, "Ideality in a Fiber-Taper-Coupled Microresonator System for Application to Cavity Quantum Electrodynamics," Physical Review Letters 91, 043902 (n.d.).

18. S. Ravets, J. E. Hoffman, P. R. Kordell, J. D. Wong-Campos, S. L. Rolston, and L. A. Orozco, "Intermodal energy transfer in a tapered optical fiber: optimizing transmission," J Opt Soc Am 30, 2361 (2013).

19. J. Villatoro, D. Monzón-Hernández, and E. Mejía, "Fabrication and modeling of uniform-waist single-mode tapered optical fiber sensors.," Appl Optics 42, 2278–83 (2003).

20. M. Sumetsky, "Uniform coil optical resonator and waveguide: transmission spectrum, eigenmodes, and dispersion relation.," Optics express 13, 4331–40 (2005).

21. F. Xu and G. Brambilla, "Embedding optical microfiber coil resonators in Teflon," Opt. Lett. 32, 2164 (2007).

22. J. Hou, H. Ding, B. Wei, C. Gao, and X. Li, "Microfiber knot resonator based electric field sensor," Instrumentation Science & Technology (2016).

23. L. Xiao and T. Birks, "High finesse microfiber knot resonators made from double-ended tapered fibers.," Opt. Lett. 36, 1098 (2011).

24. X. Zeng, Y. Wu, C. Hou, J. Bai, and G. Yang, "A temperature sensor based on optical microfiber knot resonator," Optics Communications 282, 3817–3819 (2009).

25. Y. Wu, X. Zeng, Y.-J. Rao, C.-L. Hou, and G.-G. Yang, "MOEMS accelerometer based on microfiber knot resonator," spie 75036U-75036U–4 (2009).

26. X. Jiang, Q. Yang, G. Vienne, Y. Li, L. Tong, J. Zhang, and L. Hu, "Demonstration of microfiber knot laser," Appl Phys Lett 89, 143513 (2006).

27. L. Ding, C. Belacel, S. Ducci, G. Leo, and I. Favero, "Ultralow loss single-mode silica tapers

manufactured by a microheater," Appl Optics 49, 2441 (2010).

28. L. Ding, P. Senellart, A. Lemaitre, S. Ducci, G. Leo, and I. Favero, "GaAs micro-nanodisks probed by a looped fiber taper for optomechanics applications," (2010).

29. X. Guo and L. Tong, "Supported microfiber loops for optical sensing," Opt Express 16, 14429 (2008).

30. F. Xu, V. Pruneri, V. Finazzi, and G. Brambilla, "An embedded optical nanowire loop resonator refractometric sensor.," Optics express 16, 1062–7 (2008).

31. M. Sumetsky, Y. Dulashko, J. Fini, A. Hale, and D. DiGiovanni, "The Microfiber Loop Resonator: Theory, Experiment, and Application," J Lightwave Technol 24, 242–250 (2006).

32. F. J. Arregui, I. Villar, C. R. Zamarreño, P. Zubiate, and I. R. Matias, "Giant sensitivity of optical fiber sensors by means of lossy mode resonance," Sensors and Actuators B: Chemical 232, 660–665 (2016).

33. J. Zhao, S. Cao, C. Liao, Y. Wang, G. Wang, X. Xu, C. Fu, G. Xu, J. Lian, and Y. Wang, "Surface plasmon resonance refractive sensor based on silver-coated side-polished fiber," Sensors Actuators B Chem 230, 206–211 (2016).

34. A. Maimaiti, V. Truong, M. Sergides, I. Gusachenko, and S. Chormaic, "Higher order microfibre modes for dielectric particle trapping and propulsion," Scientific Reports 5, 9077 (2015).

35. J.-C. Beugnot, S. Lebrun, G. Pauliat, H. Maillotte, V. Laude, and T. Sylvestre, "Brillouin light scattering from surface acoustic waves in a subwavelength-diameter optical fibre," Nature Communications 5, 5242 (2014).

36. Y. Maya, N. Cardona, and P. Trujillo, "Low cost heat-and-pull rig for manufacturing adiabatic optical fiber tapers," Revista Facultad de Ingeniería Universidad de Antioquia (2014).

37. J. M. Ward, D. G. O'Shea, B. J. Shortt, M. J. Morrissey, K. Deasy, and S. G. Chormaic, "Heat-and-pull rig for fiber taper fabrication," Rev Sci Instrum 77, 083105 (2006).

38. Z. Chenari, H. Latifi, S. Ghamari, R. S. Hashemi, and F. Doroodmand, "Adiabatic tapered optical fiber fabrication in two step etching," Optics & Laser Technology 76, 91–95 (2016).

39. H. S. Haddock, P.ankar, and R. Mutharasan, "Fabrication of biconical tapered optical fibers using hydrofluoric acid," Materials Science and Engineering: B 97, 87–93 (2003).

40. F. Orucevic, V. Lefèvre-Seguin, and J. Hare, "Transmittance and near-field characterization

of sub-wavelength tapered optical fibers," Opt Express 15, 13624 (2007).

41. J. Ward, A. Maimaiti, V. H. Le, and N. S. Chormaic, "Contributed Review: Optical micro- and nanofiber pulling rig," Review of Scientific Instruments 85, 111501 (2014).

42. V. Kavungal, G. Farrell, Q. Wu, A. Mallik, and Y. Semenova, "A comprehensive experimental study of whispering gallery modes in a cylindrical microresonator excited by a tilted fiber taper," Microw Opt Techn Let 60, 1495–1504 (2018).

43. -P J Laine, B. Little, and H. Haus, "Etch-eroded fiber coupler for whispering-gallery-mode excitation in high-Q silica microspheres," IEEE Photonics Technology Letters 11, 1429–1430 (1999).

44. E. J. Zhang, W. D. Sacher, and J. K. Poon, "Hydrofluoric acid flow etching of low-loss subwavelength-diameter biconical fiber tapers," Opt Express 18, 22593 (2010).

45. S. Zhu, F. Pang, S. Huang, F. Zou, Q. Guo, J. Wen, and T. Wang, "High Sensitivity Refractometer Based on TiO2-Coated Adiabatic Tapered Optical Fiber via ALD Technology," Sensors 16, 1295 (2016).

46. Y. Tian, W. Wang, N. Wu, X. Zou, and X. Wang, "Tapered Optical Fiber Sensor for Label-Free Detection of Biomolecules," Sensors Basel Switz 11, 3780–3790 (2011).

47. Y. Xue, Y.-S. Yu, R. Yang, C. Wang, C. Chen, J.-C. Guo, X.-Y. Zhang, C.-C. Zhu, and H.-B. Sun, "Ultrasensitive temperature sensor based on an isopropanol-sealed optical microfiber taper," Opt Lett 38, 1209 (2013).

48. "Liquid Point Sensor by Brillouin Backscattering in Tapered Silica Optical Fiber," (n.d.).

49. G. Sagué, E. Vetsch, W. Alt, D. Meschede, and A. Rauschenbeutel, "Cold-Atom Physics Using Ultrathin Optical Fibers: Light-Induced Dipole Forces and Surface Interactions," Phys Rev Lett 99, 163602 (2007).

50. G. Brambilla, S. G. Murugan, J. Wilkinson, and D. Richardson, "Optical manipulation of microspheres along a subwavelength optical wire," Opt Lett 32, 3041 (2007).

51. H. Xin, C. Cheng, and B. Li, "Trapping and delivery of Escherichia coli in a microfluidic channel using an optical nanofiber.," Nanoscale 5, 6720–4 (2013).

52. H. Lei, Y. Zhang, X. Li, and B. Li, "Photophoretic assembly and migration of dielectric particles and Escherichia coli in liquids using a subwavelength diameter optical fiber," Lab on a Chip 11, 2241–2246 (n.d.).

53. L. Zhang, P. Wang, Y. Xiao, H. Yu, and L. Tong, "Ultra-sensitive microfibre absorption detection in a microfluidic chip," Lab Chip 11, 3720–3724 (2011).

54. P. Polynkin, A. Polynkin, N. Peyghambarian, and M. Mansuripur, "Evanescent field-based optical fiber sensing device for measuring the refractive index of liquids in microfluidic channels," Opt Lett 30, 1273 (2005).

55. K. nivasan, M. Borselli, A. Stintz, S. Krishna, and O. Painter, "Cavity Q, mode volume, and lasing threshold in small diameter AlGaAs microdisks with embedded quantum dots," Opt Express 14, 1094 (2005).

56. F. Vollmer, S. Arnold, and D. Keng, "Single virus detection from the reactive shift of a whispering-gallery mode," Proc National Acad Sci 105, 20701–20704 (2008).

57. F. Xie, N. Yao, W. Fang, H. Wang, F. Gu, and S. Zhuang, "Single-mode lasing via loss engineering in fiber-taper-coupled polymer bottle microresonators," Photonics Res 5, B29 (2017).

58. metsky, "A SNAP coupled microresonator delay line.," Opt Express 21, 15268–79 (2013).

59. L. Gai, J. Li, and Y. Zhao, "Preparation and application of microfiber resonant ring sensors: A review," Optics & Laser Technology 89, 126–136 (2017).

60. G. Brambilla, F. Xu, P. Horak, Y. Jung, F. Koizumi, N. P. Sessions, E. Koukharenko, X. Feng, G. S. Murugan, J. S. Wilkinson, and D. J. Richardson, "Optical fiber nanowires and microwires: fabrication and applications," Adv Opt Photonics 1, 107 (2009).

61. Y. Xu, L. Ren, J. Liang, C. Ma, Y. Wang, N. Chen, and E. Qu, "A simple, polymer-microfiber-assisted approach to fabricating the silica microfiber knot resonator," Opt Commun 321, 157–161 (2014).

62. Y. Jung, G. Murugan, G. Brambilla, and D. J. Richardson, "Embedded Optical Microfiber Coil Resonator With Enhanced High-<formula formulatype="inline"><tex Notation="TeX">Q</tex></formula>," Ieee Photonic Tech L 22, 1638–1640 (2010).

63. S. Yan, B. Zheng, J. Chen, F. Xu, and Y. Lu, "Optical electrical current sensor utilizing a graphene-microfiber-integrated coil resonator," Appl Phys Lett 107, 053502 (2015).

64. M. Khan and S.-W. Kang, "A High Sensitivity and Wide Dynamic Range Fiber-Optic Sensor for Low-Concentration VOC Gas Detection," Sensors 14, 23321–23336 (2014).

65. H. Ahmad, A. Zulkifli, and Z. Tiu, "Acrylate polymer coated side-polished fiber with graphene oxide nanoparticles for ultrafast fiber laser operation," Laser Phys 28, 115101 (2018).

66. A. O. Dikovska, G. B. Atanasova, N. N. Nedyalkov, P. K. Stefanov, P. A. Atanasov, E. I. Karakoleva, and A. T. Andreev, "Optical sensing of ammonia using ZnO nanostructure grown on a side-polished optical-fiber," Sensors Actuators B Chem 146, 331–336 (2010).

67. T. Batchman and G. McWright, "Mode coupling between dielectric and semiconductor planar waveguides," Ieee J Quantum Elect 18, 782–788 (1982).

68. M. Marciniak, J. Grzegorzewski, and ustakowski, "Analysis of lossy mode cut-off conditions in planar waveguides with semiconductor guiding layer," Iee Proc J Optoelectron 140, 247 (1993).

69. I. Villar, C. R. Zamarreño, M. Hernaez, F. J. Arregui, and I. R. Matias, "Generation of Lossy Mode Resonances with Absorbing Thin-Films," Ieee Osa J Light Technology 28, 3351–3357 (2010).

70. I. Villar, F. J. Arregui, C. R. Zamarreño, J. M. Corres, C. Bariain, J. Goicoechea, C. Elosua, M. Hernaez, P. J. Rivero, A. B. Socorro, A. Urrutia, P. Sanchez, P. Zubiate, D. Lopez, N. Acha, J. Ascorbe, and I. R. Matias, "Optical sensors based on lossy-mode resonances," Sensors and Actuators B: Chemical 240, 174–185 (2017).

71. I. D. Villar, P. Zubiate, C. R. Zamarreño, F. J. Arregui, and I. R. Matias, "Optimization in nanocoated D-shaped optical fiber sensors," Opt Express 25, 10743 (2017).

72. I. Villar, V. Torres, and M. Beruete, "Experimental demonstration of lossy mode and surface plasmon resonance generation with Kretschmann configuration," Optics Letters 40, 4739 (2015).

73. P. Zubiate, C. Zamarreño, D. I. Villar, I. Matias, and F. Arregui, "D-shape optical fiber refractometer based on TM and TE lossy mode resonances," 91577V-91577V–4 (2014).

74. F. J. Arregui, I. Villar, J. M. Corres, J. Goicoechea, C. R. Zamarreño, C. Elosua, M. Hernaez, P. J. Rivero, A. B. Socorro, A. Urrutia, P. Sanchez, P. Zubiate, D. Lopez, N. Acha, and I. R. Matias, "Fiber-optic Lossy Mode Resonance Sensors," Procedia Engineering 87, 3–8 (2014).

75. D. I. Villar, M. Hernaez, and Z. C. Applied …, "Design rules for lossy mode resonance based sensors," (2012).

76. I. Villar, M. Hernaez, C. R. Zamarreño, P. Sánchez, C. Fernández-Valdivielso, F. J. Arregui, and I. R. Matias, "Design rules for lossy mode resonance based sensors," Applied Optics 51, 4298 (2012).

77. C. Zamarreño, M. Hernaez, D. I. Villar, I. Matias, and F. Arregui, "Lossy Mode Resonance-Based Optical Fiber Humidity Sensor," 2011 IEEE SENSORS Proceedings 234–237 (2011).

78. Q. Wang and W.-M. Zhao, "A comprehensive review of lossy mode resonance-based fiber optic sensors," Opt Laser Eng 100, 47–60 (2018).

79. N. Paliwal, N. Punjabi, J. John, and S. Mukherji, "Design and Fabrication of Lossy Mode Resonance Based U-Shaped Fiber Optic Refractometer Utilizing Dual Sensing Phenomenon," J Lightwave Technol 34, 4187–4194 (2016).

80. P. Zubiate, C. R. Zamarreno, I. Villar, I. R. Matias, and F. J. Arregui, "Experimental Study and Sensing Applications of Polarization-Dependent Lossy Mode Resonances Generated by D-Shape Coated Optical Fibers," J Lightwave Technol 33, 2412–2418 (2015).

81. J. Ascorbe, J. M. Corres, F. J. Arregui, and I. R. Matias, "Recent Developments in Fiber Optics Humidity Sensors," Sensors 17, 893 (2017).

82. C. R. Zamarreño, P. Zubiate, M. Sagües, I. R. Matias, and F. J. Arregui, "Experimental demonstration of lossy mode resonance generation for transverse-magnetic and transverse-electric polarizations.," Opt Lett 38, 2481–3 (2013).

83. Y. Li, O. V. Svitelskiy, A. V. Maslov, D. Carnegie, E. Rafailov, and V. N. Astratov, "Giant resonant light forces in microspherical photonics," Light: Science & Applications 2, e64 (2013).

84. G. Violakis, N. Korakas, and S. Pissadakis, "Differential loss magnetic field sensor using a ferrofluid encapsulated D-shaped optical fiber," Opt Lett 43, 142 (2017).

85. Y. Zhang, C. Gu, A. hwartzberg, and J. Zhang, "Surface-enhanced Raman scattering sensor based on D-shaped fiber," Appl Phys Lett 87, 123105 (2005).

86. J. Nayak and R. Jha, "Numerical simulation on the performance analysis of a graphene-coated optical fiber plasmonic sensor at anti-crossing.," Appl Optics 56, 3510–3517 (2017).

87. T. Sherwood, A. C. Young, J. Takayesu, A. K. Y. Jen, L. R. Dalton, and A. Chen, "Microring resonators on side-polished optical fiber," Ieee Photonic Tech L 17, 2107–2109 (2005).

88. H. Xin, H. Lei, Y. Zhang, X. Li, and B. Li, "Photothermal trapping of dielectric particles by optical fiber-ring," Optics Express 19, 2711–2719 (2036).

89. I. Villar, C. R. Zamarreño, M. Hernaez, F. J. Arregui, and I. R. Matias, "Lossy Mode Resonance Generation with Indium-Tin-Oxide-Coated Optical Fibers for Sensing Applications," IEEE/OSA Journal of Lightwave Technology 28, 111–117 (2010).

90. L. Tong, R. R. Gattass, J. B. Ashcom, S. He, J. Lou, M. Shen, I. Maxwell, and E. Mazur, "Subwavelength-diameter silica wires for low-loss optical wave guiding," Nature 426, 816

(2003).

91. Y. Jung, G. Brambilla, G. Murugan, and D. J. Richardson, "Optical racetrack ring-resonator based on two U-bent microfibers," Appl Phys Lett 98, 021109 (2011).

92. T. Tiecke, K. Nayak, J. Thompson, T. Peyronel, N. de Leon, V. Vuletić, and M. Lukin, "Efficient fiber-optical interface for nanophotonic devices," Optica 2, 70 (2015).

93. Y. Zhang and B. Li, "Particle sorting using a subwavelength optical fiber," Laser & Photonics Reviews 7, 289–296 (2013).

94. H. Xin, R. Xu, and B. Li, "Optical trapping, driving, and arrangement of particles using a tapered fibre probe," SCIENTIFIC REPORTS (2012).

95. Y. Sun and X. Fan, "Optical ring resonators for biochemical and chemical sensing," Anal Bioanal Chem 399, 205–211 (2011).

96. V. R. Almeida, C. A. Barrios, R. R. Panepucci, and M. Lipson, "All-optical control of light on a silicon chip," Nature 431, 1081–1084 (2004).

97. K. nivasan, A. Stintz, S. Krishna, and O. Painter, "Photoluminescence measurements of quantum-dot-containing semiconductor microdisk resonators using optical fiber taper waveguides," Phys Rev B 72, 205318 (2005).

98. M. Aili, V. Truong, M. Sergides, I. Gusachenko, and S. Chormaic, "Propulsion of particles using ultrathin optical fibers," (2015).

99. K. Lim, A. A. Jasim, S. S. Damanhuri, S. W. Harun, A. B. Rahman, and H. Ahmad, "Resonance condition of a microfiber knot resonator immersed in liquids.," Appl. Opt. 50, 5912 (2011).

100. A. Sulaiman, S. W. Harun, and H. Ahmad, "Thermally tunable microfiber knot resonator based erbium-doped fiber laser," Optics Communications 285, 4684–4687 (2012).

101. Z. Zhang, W. Fan, J. Gan, C. Li, and Z. Yang, "Single-Frequency Microfiber Single-Knot Laser," Appl Phys Express 6, 042702 (2013).

102. M. Aili, V. Truong, M. Sergides, I. Gusachenko, and S. Chormaic, "Propulsion of particles using ultrathin optical fibers," OtT1D.3 (2015).

103. L. Liu, L. Jin, J. Li, Y. Ran, and B.-O. Guan, "Fabrication of highly stable microfiber structures via high-substituted hydroxypropyl cellulose coating for device and sensor applications," Optics Letters 40, 1492 (2015).

104. R. Zhang, C. Ti, M. Davanço, Y. Ren, V. Aksyuk, Y. Liu, and K. nivasan, "Integrated tuning fork nanocavity optomechanical transducers with high fMQM product and stress-engineered frequency tuning," Applied Physics Letters 107, 131110 (2015).

105. D. A. Ateya, J. S. Erickson, P. B. Howell, L. R. Hilliard, J. P. Golden, and F. S. Ligler, "The good, the bad, and the tiny: a review of microflow cytometry," Anal Bioanal Chem 391, 1485–1498 (2008).

106. G. Nava, F. Bragheri, T. Yang, P. Minzioni, R. Osellame, I. Cristiani, and K. Berg-Sørensen, "All-silica microfluidic optical stretcher with acoustophoretic prefocusing," Microfluid Nanofluid 19, 837–844 (2015).

107. J. Lou, Y. Wang, and L. Tong, "Microfiber Optical Sensors: A Review," Sensors 14, 5823–5844 (2014).

108. T. Hamidfar, A. Dmitriev, B. Magdan, P. Bianucci, and metsky, "Surface nanoscale axial photonics at a capillary fiber," Optics Letters 42, 3060 (2017).

109. I. Turek, I. Martinc˘ek, and R. Stra´nsky, "Interference of modes in optical fibers," Opt Eng 39, 1304–1309 (2000).

110. A. B. Socorro, J. M. Corres, D. I. Villar, F. J. Arregui, and I. R. Matias, "Fiber-optic biosensor based on lossy mode resonances," Sensors and Actuators B: Chemical 174, 263–269 (2012).

111. S. P. Cauvain and L. S. Young, "Bakery food manufacture and quality: water control and effects," (2009).

112. J. Ascorbe, J. M. Corres, I. R. Matias, and F. . Arregui, "High sensitivity humidity sensor based on cladding-etched optical fiber and lossy mode resonances," Sensors and Actuators B: Chemical 233, 7–16 (2016).

113. D. C. Duffy, C. J. nald, O. J. Schueller, and G. M. Whitesides, "Rapid Prototyping of Microfluidic Systems in Poly(dimethylsiloxane)," Analytical Chemistry 70, 4974–4984 (1998).

114. X. Chen and J. Shen, "Review of membranes in microfluidics," J Chem Technol Biot 92, 271–282 (2017).

115. G. Velve-Casquillas, M. Berre, M. Piel, and P. T. Tran, "Microfluidic tools for cell biological research," Nano Today 5, 28–47 (2010).

116. D. Holmes and S. Gawad, "The Application of Microfluidics in Biology," Methods Mol

Biology Clifton N J 583, 55–80 (2010).

117. K. S. Elvira, X. i Solvas, R. C. Wootton, and A. J. deMello, "The past, present and potential for microfluidic reactor technology in chemical synthesis," Nature Chemistry 5, 905–915 (2013).

118. M. Zandvakili, "Liquid Metal Based Test Structures and Reconfigurable Microfluidic Microwave Devices and Antennas," (2017).

119. E. K. Sackmann, A. L. Fulton, and D. J. Beebe, "The present and future role of microfluidics in biomedical research," Nature 507, nature13118 (2014).

120. R. Mukhopadhyay, "When PDMS isn't the best," Analytical Chemistry 79, 3248–3253 (2007).

121. S. Altundemir, A. Uguz, and K. Ulgen, "A review on wax printed microfluidic paper-based devices for international health," Biomicrofluidics 11, 041501 (2017).

122. A. W. Martinez, S. T. Phillips, G. M. Whitesides, and E. Carrilho, "Diagnostics for the Developing World: Microfluidic Paper-Based Analytical Devices," Anal Chem 82, 3–10 (2010).

123. K. Vittayarukskul and A. Lee, "A truly Lego®-like modular microfluidics platform," J Micromech Microeng 27, 035004 (2017).

124. N. Bhattacharjee, A. Urrios, S. Kang, and A. Folch, "The upcoming 3D-printing revolution in microfluidics," Lab Chip 16, 1720–1742 (2016).

125. C. E. Owens and J. A. Hart, "High-precision modular microfluidics by micromilling of interlocking injection-molded blocks," Lab Chip 18, 890–901 (2017).

126. X. Chen, T. Li, and J. Shen, "CO2Laser Ablation of Microchannel on PMMA Substrate for Effective Fabrication of Microfluidic Chips," Int Polym Proc 31, 233–238 (2016).

127. H. Klank, J. P. Kutter, and O. Geschke, "CO 2 -laser micromachining and back-end processing for rapid production of PMMA-based microfluidic systems," Lab on a Chip 2, 242–246 (2002).

128. A. Chandrasekaran, N. Kalashnikov, R. Rayes, C. Wang, J. Spicer, and C. Moraes, "Thermal scribing to prototype plastic microfluidic devices, applied to study the formation of neutrophil extracellular traps," Lab on a Chip 17, 2003–2012 (2017).

129. X. Chen, T. Li, and Q. Gao, "A novel method for rapid fabrication of PMMA microfluidic chip by laser cutting and sealing integration," Surf Rev Lett (2018).

130. T.-F. Hong, W.-J. Ju, M.-C. Wu, C.-H. Tai, C.-H. Tsai, and L.-M. Fu, "Rapid prototyping of PMMA microfluidic chips utilizing a CO2 laser," Microfluidics and Nanofluidics 9, 1125–1133 (2010).

131. X. Chen, T. Li, K. zhai, Z. Hu, and M. Zhou, "Using orthogonal experimental method optimizing surface quality of CO2 laser cutting process for PMMA microchannels," The International Journal of Advanced Manufacturing Technology 88, 2727–2733 (2017).

132. D. Pérez-Calixto, D. Zamarrón-Hernández, A. Cruz-Ramírez, M. Hautefeuille, J. Hérnandez-Cordero, V. Velázquez, and M. Grether, "Fabrication of large all-PDMS micropatterned waveguides for lab on chip integration using a rapid prototyping technique," Optical Materials Express 7, 1343 (2017).

133. S. N. Lynn and D. S. Dandy, "Passive microfluidic pumping using coupled capillary/ evaporation effects," Lab Chip 9, 3422–3429 (2009).

134. H. Bruus, Governing Equations in Microfluidics. (2015), pp. 1–28.

135. M. M. Gong and D. Sinton, "Turning the Page: Advancing Paper-Based Microfluidics for Broad Diagnostic Application," Chem Rev 117, 8447–8480 (2017).

136. J. Songok and M. Toivakka, "Controlling capillary-driven surface flow on a paper-based microfluidic channel," Microfluidics and Nanofluidics 20, 63 (2016).

137. A. C. Glavan, R. V. Martinez, J. E. Maxwell, A. Subramaniam, R. Nunes, S. Soh, and G. M. Whitesides, "Rapid fabrication of pressure-driven open-channel microfluidic devices in omniphobic RF paper," Lab on a chip 13, 2922–2930 (n.d.).

138. B. J. Toley, B. McKenzie, T. Liang, J. R. Buser, P. Yager, and E. Fu, "Tunable-Delay Shunts for Paper Microfluidic Devices," Anal Chem 85, 11545–11552 (2013).

139. B. M. Cummins, R. Chinthapatla, B. Lenin, F. S. Ligler, and G. M. Walker, "Modular pumps as programmable hydraulic batteries for microfluidic devices," TECHNOLOGY 1–10 (2017).

140. J. L. Osborn, B. Lutz, E. Fu, P. Kauffman, D. Y. Stevens, and P. Yager, "Microfluidics without pumps: reinventing the T-sensor and H-filter in paper networks," Lab on a Chip 10, 2659–2665 (2010).

141. T. Kokalj, Y. Park, M. Vencelj, M. Jenko, and L. P. Lee, "Self-powered Imbibing Microfluidic Pump by Liquid Encapsulation: SIMPLE," Lab Chip 14, 4329–4333 (2014).

142. D. R. Link, E. Grasland-Mongrain, A. Duri, F. Sarrazin, Z. Cheng, G. Cristobal, M.

Marquez, and D. A. Weitz, "Electric Control of Droplets in Microfluidic Devices," Angewandte Chemie International Edition 45, 2556–2560 (2006).

143. Q. Yan, S. Xuan, X. Ruan, J. Wu, and X. Gong, "Magnetically controllable generation of ferrofluid droplets," Microfluid Nanofluid 19, 1377–1384 (2015).